11-27-2017 3:00 PM

Free-Surface Wall-Jet Flow at Moderate Reynolds Number as Applied to Slot and Blade Coating

Mohammad Tanvir Hossain, *The University of Western Ontario*

Supervisor: Khayat, Roger E., *The University of Western Ontario*

A thesis submitted in partial fulfillment of the requirements for the Master of Engineering Science degree in Mechanical and Materials Engineering

Abstract

The flow of a two-dimensional steady wall jet observed in the slot and blade coating processes has been examined theoretically near the channel exit. The Newtonian free surface jet emerges from a channel and deposits onto an infinite moving wall with an adverse or favorable pressure gradient applied inside the channel. The Reynolds number considered is within the moderate range, and fully developed Couette-Poisueille flow conditions are assumed to prevail far upstream inside the channel. The effects of inertia and pressure gradient on the velocity, the shape of the free surface, and the stress are emphasized. It is found that the jet always contracts near the channel exit regardless of the level of inertia and direction of the applied pressure gradient. An adverse pressure gradient provides thinner film thickness than a favorable one.

Keywords

Wall jet flows, free surface flows, slot coating, blade coating, matched asymptotic expansion, moderate Reynolds number, inertia, laminar jet flows, moving wall, boundary layers, channel exit.

Acknowledgments

All praises are due to the almighty Allah for providing me the excellent opportunity to work in the field of research. Throughout this journey, I got help from several people, and I would like to offer my sincere gratitude towards them. First, I would like to thank my esteemed supervisor Prof. Dr. Roger Khayat for his constant support and guidance in completing my master's research work. His involvement has helped me to enrich my knowledge and has developed my skills as a researcher.

I offer my regards and thanks to my colleagues: Md. Asif Zobaer and Yunpeng Wang for their valuable comments and companionship throughout the entire tenure of my master's degree. I would also like to acknowledge my friend Md. Yahia Hussain for helping me to understand the solution strategy.

Finally, I thank my parents and brother for their constant encouragement and support throughout my life.

Table of Contents

Abstract i

Acknowledgments ii

Table of Contents iii

List of Tables v

List of Figures vi

List of symbols x

Chapter 1 1

1 Introduction 1

1.1 Problem description and practical relevance of the current study 3

1.2 Boundary layer theory 6

1.3 A brief discussion on the solution strategy 10

1.4 Historical overview on coating flows 16

1.5 Motivation 21

1.6 Summary 22

Chapter 2 23

2 Free surface moving wall jet flow near the channel exit 23

2.1 Problem formulation 23

2.2 The Kinematic and dynamic boundary conditions on the free surface 25

2.3 Flow in the free-surface or inner layer 29

2.3.1 Flow in the inner layer to $O\left(\varepsilon^2\right)$ 32

2.3.2 Flow in the inner layer to $O\left(\varepsilon^3\right)$ 37

2.4 Flow in the lower wall layer 51

2.5 Flow in the core layer 66

2.5.1 Flow in the core layer upstream of the channel exit $(x < 0)$ 68

2.5.2 Flow in the core layer downstream of the channel exit $(x > 0)$ 72

2.5.3 Pressure in the core layer and elsewhere 74

2.6 Composite flow 79

2.7 Flow far from the channel exit 84

2.8 Matching between the inner and core layer 86

Chapter 3 92

3 Summary and concluding remarks 92

3.1 Future work 93

References 95

List of Tables

Table 1: Values for the first six modes for $[G \in 0.2, 0.8]$ 69

Table 2: Values for the first six modes for $[G \in -0.2, -0.8]$ 70

List of Figures

Figure 1.1: Schematic representations of the (a) free surface jet, (b) wall jet and (c) impinging jet..... 2

Figure 1.2: (a) Schematic illustrations of a typical slot coating and (b) schematic illustrations of the analyzed domain of the slot coating process. 4

Figure 1.3: (a) Schematic illustrations of a typical blade coating process and (b) schematic illustrations of the analyzed domain of the blade coating process..... 4

Figure 1.4: Schematic representation of the moving wall jet (Schlichting 2000). 7

Figure 1.5: Shear stress distribution along the moving plate..... 9

Figure 1.6: Schematic representation of (a) Tillett's (1968) free surface jet and (b) his region of study..... 10

Figure 1.7: Pressure development along the centerline with distance x (Tillett 1968)..... 14

Figure 1.8: Different applications of coating processes (a) adhesive tapes, (b) paper, (c) thin displays and (d) transparent printed electronics (Araujo and Carvalho 2014). 16

Figure 2.1: Schematic illustration of the free surface wall jet of (a) the slot coating and (b) the blade coating (dimensionless notions are used).. 24

Figure 2.2: Schematic representation of the dynamic boundary condition on the free surface. 25

Figure 2.3: Schematic depiction of the computational domain (all notations are dimensionless). The boundary layers are depicted along the free surface (dotted lines), upper wall and lower wall. Five segments of the control volume analysis are also shown. 28

Figure 2.4: Variation of the function g_2, g_2' and g_2'' with t for all the G values. 35

Figure 2.5: Variation of similarity function f_2 with θ for all the G values..... 35

Figure 2.6: Dependence of the initial slope $f_2'(0)$ and c_1 on the parameter G. 36

Figure 2.7: Variation of the function g_3, g_3' and g_3'' with t for all the G values. 39

Figure 2.8: Variation of similarity function f_2 with θ for all the G values. 39

Figure 2.9: Dependence of the initial slope $f_3'(0)$ and c_2 on the parameter G. 41

Figure 2.10: Influence of pressure gradient (a) adverse $(G \in [0, 0.8])$ and (b) favorable $(G \in [0, -0.8])$ on the streamwise velocity u at the free surface $z = \zeta(x)$ for $\varepsilon = 0.1$. 43

Figure 2.11: Influence of inertia on the streamwise velocity $u(x = 1, z = \zeta)$ at the free surface $z = \zeta(x)$ (a) for different ε and (b) $\mathrm{Re}\, u(x = 1, z = \zeta)$. 44

Figure 2.12: Influence of pressure gradient (a) adverse $(G \in [0, 0.8])$ and (b) favorable $(G \in [0, -0.8])$ on free surface $z = \zeta(x)$ for $\varepsilon = 0.1$. 45

Figure 2.13: Influence of inertia on the jet surface $\zeta(x = 1)$ 46

Figure 2.14: Influence of pressure gradient (a) adverse $(G \in [0, 0.8])$ and (b) favorable $(G \in [0, -0.8])$ on the transverse velocity, $w(x, z = \zeta)$ at the free surface, $z = \zeta(x)$ for $\varepsilon = 0.1$ 47

Figure 2.15: Effect of inertia on the free surface curvature with the inclination angle for G=0.4 48

Figure 2.16: Free surface curvature variation with the inclination angle for $G \in [0, 0.8]$ and $\varepsilon = 0.2$ 48

Figure 2.17: Development of the pressure along the free surface with distance x for $\varepsilon = 0.2$ and for $G \in [0, -0.8]$ 49

Figure 2.18: Effect of inertia on the pressure along the free surface for G=-0.4. 49

Figure 2.19: Development of the film thickness with Re for different level of pressure gradient ($G \in [-0.4, 0.4]$). 50

Figure 2.20: the profiles of $F_n'(\eta)$ for the first six eigen modes (G=0.4). Also the values of $F_n''(\eta = 0)$ and $F_n'''(\eta = 0)$ are shown in the insets. 57

Figure 2.21: Streamwise velocity disturbance profiles near the lower wall for (a) G=0.4 and (b) G=-0.4. 59

Figure 2.22: Transverse velocity disturbance profiles near the lower wall for (a) G=0.4 and (b) G=-0.4. 60

Figure 2.23: Influence of inertia on pressure along the lower wall for (a) G=0.4 and (b) G=-0.4. 61

Figure 2.24: Influence of inertia on the wall shear stress along the lower wall for (a) G=0.4 and (b) G=-0.4. 62

Figure 2.25: Pressure profile along the lower wall and free surface for $\varepsilon = 0.44$ and G=-0.4. Inset shows the magnification of the area very close to the exit inside the channel. 63

Figure 2.26: Pressure profile for trailing stiff blade geometry for Re=12 (figure 9 of Lliopoulos and Scriven 2005). Inset shows the blade configuration (figure 4 of Lliopoulos and Scriven 2005). 63

Figure 2.27: Pressure distribution in the blade coating of a shear-thinning fluid obeying the Carreau model for S010 geometry (figure 11b of Mitsoulis and Athanasopoulos 2010). Inset shows the S010 geometry (figure 11a of Mitsoulis and Athanasopoulos 2010). 64

Figure 2.28: Axial shear stress profile along the blade wall and roll for a Newtonian fluid in the S010 geometry (figure 8a of Mitsoulis and Athanasopoulos 2010). Inset shows the S010 geometry (figure 7a of Mitsoulis and Athanasopoulos 2010). 65

Figure 2.29: Shape function V_n vs z for the first six Eigen modes for $G = -0.4$ 71

Figure 2.30: the profiles of function $V_0(z)$ for different G values 73

Figure 2.31: Influence of pressure gradient on the pressure distribution at the upper wall for (a) $G \in [0.2, 0.8]$ and (b) $G \in [-0.2, -0.8]$ 77

Figure 2.32: Pressure distribution at different heights for (a) G=0.4 and (b) G=-0.4..... 78

Figure 2.33: Composite Streamwise velocity profile over the entire jet region at different locations for (a) G=0.4, (b) G=0 and (c) G=-0.4 and for $\varepsilon = 0.2$. Vertical lines represent the corresponding x location. 81

Figure 2.34: Composite transverse velocity profiles over the entire jet region at different locations for (a) G=0.4, (b) G=0 and (c) G=-0.4 and for $\varepsilon = 0.2$. Vertical lines represent the corresponding x locations and insets show the magnification of the velocity component. 82

Figure 2.35: Composite pressure profiles across the jet width for (a) G=0.4, (b) G=0 and (c) G=-0.4 and for $\varepsilon = 0.2$. Vertical lines represent the corresponding x locations. 83

List of symbols

A_n	n^{th} value of the coefficients
C	Moving wall velocity
C_n	Composite expansion operator to $O(\varepsilon^n)$
c_1, c_2	Integration constants of the f_2 and f_3 equations
D	Channel gap/width
d_1, d_2	Integration constants of g_2 and g_3 equations
E_n	Core expansion operator to $O(\varepsilon^n)$
F_n	Shape functions for the flow in the lower-wall layer
f_2	Similarity function for the inner region flow to $O(\varepsilon^2)$
f_3	Similarity function for the inner region flow to $O(\varepsilon^3)$
G	Non-dimensional pressure gradient
g_2	Similarity function for the inner region flow to $O(\varepsilon^2)$
g_3	Similarity function for the inner region flow to $O(\varepsilon^3)$
H_m	Inner expansion operator to $O(\varepsilon^n)$
h	Shape of the free surface
k	Constant in the shape functions equations

l	Characteristics length
p	Pressure
p_n	Perturbation pressure to $O\left(\varepsilon^n\right)$
Re	Reynolds number
u	Streamwise velocity component
U_n	Perturbation of streamwise velocity to $O\left(\varepsilon^n\right)$
V_0, V_n	Shape functions for the flow in the core layers
$\bar{v}$	Scaled transverse velocity component in the boundary layer (flat plate)
W	Uniform jet speed
W_n	Perturbation of transverse velocity to $O\left(\varepsilon^n\right)$
w	Transverse velocity component
X, Z, x, y, z	Coordinates (upper case dimensional and lower case non-dimensional)
$\bar{y}$	Scaled normal coordinate in the boundary layer (flat plate)
α	Exponential constant in the relation $Re^{-\alpha}$
β_n	n^{th} Eigen value
ε	Inverse of the cubic root of the Reynolds number/Perturbation parameter
ζ	The free surface height
η	Rescaled coordinate in the inner and lower-wall layers

θ	Similarity variable
μ	Fluid dynamic viscosity
ν	Kinematic viscosity
ξ	Coordinate in the inner and lower-wall layers
ρ	Fluid density
$\boldsymbol{\sigma}$	Total stress tensor
ϕ	Inclination angle of the free surface
χ	Final jet thickness
ψ	Stream function
ψ_0	Base Couette-Poiseuille stream function
ψ_n	Perturbation of stream function to $O\left(\varepsilon^n\right)$

Chapter 1

1 Introduction

A liquid jet is formed when a stream of liquid exits from a channel, nozzle, tube or orifice where it acquires more or less a columnar shape. This phenomenon can be seen in something as simple as in the showers and kitchens to rather complex fields including but not limited to automobile, pharmaceutical, agriculture, irrigation, ink-jet printing and cosmetics (Eggers and Villermaux 2008). Typically, this type of flow is named based on the formation mechanism such as free surface jet, wall jet, impinging jet and so on. A free surface jet forms when the fluid emanates from a slot/nozzle into the surrounding air without being bounded by any wall (see figure 1.1 a).

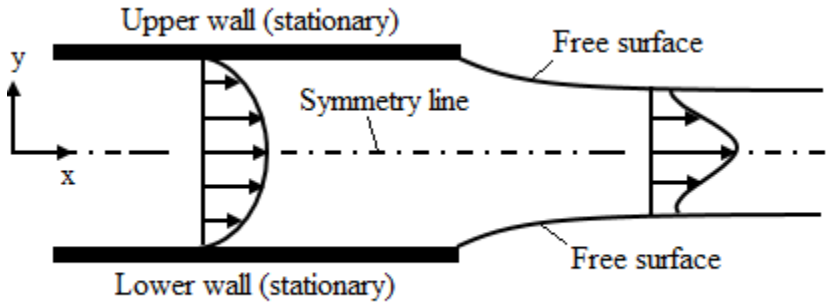

(a)

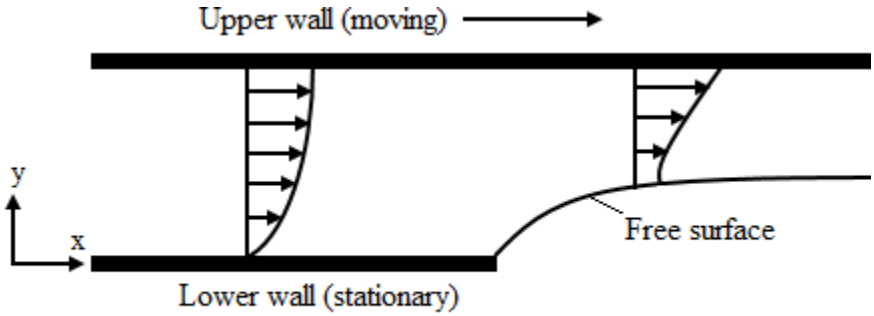

(b)

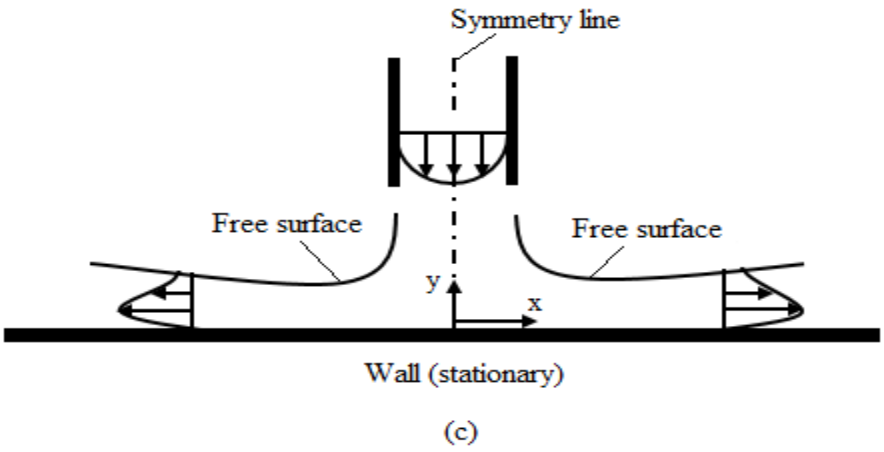

Figure 1.1: Schematic representations of the (a) free surface jet, (b) wall jet and (c) impinging jet.

However, as the name suggests, a wall jet is created when the flow of liquid is discharged through a narrow slot/gap and deposited onto a moving/stationary wall (see figure 1.1 b) (Pantokratoras 2011). When the jet strikes a wall (stationary/moving) at an angle, impinging jet forms (see figure 1.1 c). Based on the flow condition, the jet flow is either laminar or turbulent. All the aforementioned jet flows exhibit a stress singularity at the channel exit as a result of the change in the value of the shear stress from a non-zero value close to the Poiseuille level at the wall to a zero value at the free surface. This sudden jump in the shear stress causes a boundary layer to form in a region near the free surface (see sections 2.2 and 2.4 for details). In addition, both the free surface and impinging jets are symmetric about horizontal and vertical axes, respectively. However, in the case of the wall jet, the symmetry is lost due to the formation of an additional boundary layer close to the wall because of the failure of the wall adherence condition of the core flow given the inviscid character of that flow.

Given the importance of the free surface wall jet flow in the film cooling of gas turbine blades, combustion chambers and the defrosters for automobiles and most importantly in the coating (Levin et al. 2005), it has been examined extensively in the past. Glauert (1956) studied the flow of a jet on a stationary flat wall and provided a similarity solution for that wall jet flow. Later, Riley (1958) examined the compressibility effect on the wall jet. Maki (1983) and Mahmood (2005) studied the moving wall jet under the influence of heat

transfer experimentally and numerically, respectively. Merkin and Deenham (1986) investigated the effect of suction and blowing on a moving wall jet. Levin et al. (2005) explored the wall jet of Blasius type (extended to infinity in thickness). Elliotis et al. (2005) examined the wall jet in the creeping flow regime. More recently, Pantokratoras (2011) studied the laminar wall jet flow for a combination of moving plate and free stream. Other jet flows that have also been analyzed in the previous literature see, for example, the works of Tillett (1968), Philippe, and Dumargur (1991) on the free jet, Watson (1964), Bowels and Smith (1992), Bush, and Aristoff (2003) on the impinging jet and for the gravity jet, Ruschak and Scriven (1977), and Wilson (1986).

1.1 Problem description and practical relevance of the current study

This thesis focuses on the free surface flow of a planar moving-wall jet at moderate Reynolds number near the channel exit with direct relevance to the coating flow. In the current study, inertia is assumed to be important but is typically neglected in the traditional modelling of the coating process. However, inertia may not be negligible for high-speed processes. Currently, various coating processes are used such as blade, slot, curtain and dip coating (Weinstein & Ruschak, 2004).

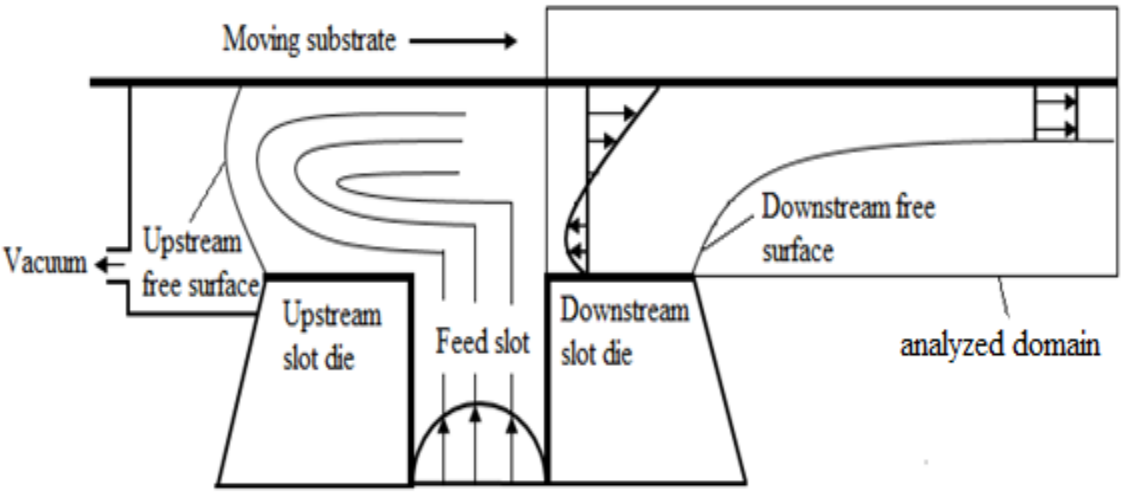

(a)

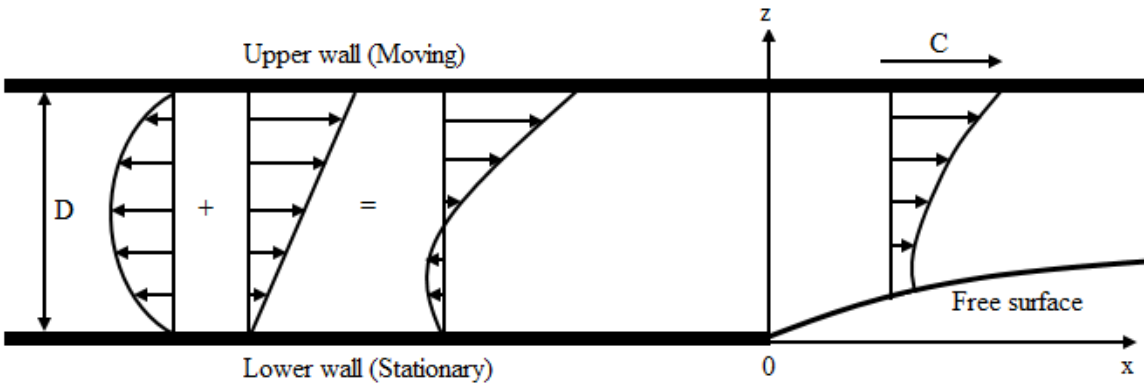

(b)

Figure 1.2: (a) Schematic illustrations of a typical slot coating and (b) schematic illustrations of the analyzed domain of the slot coating process.

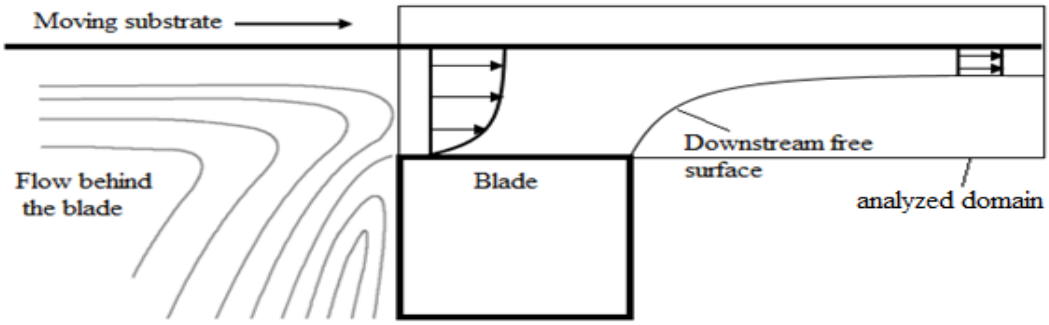

(a)

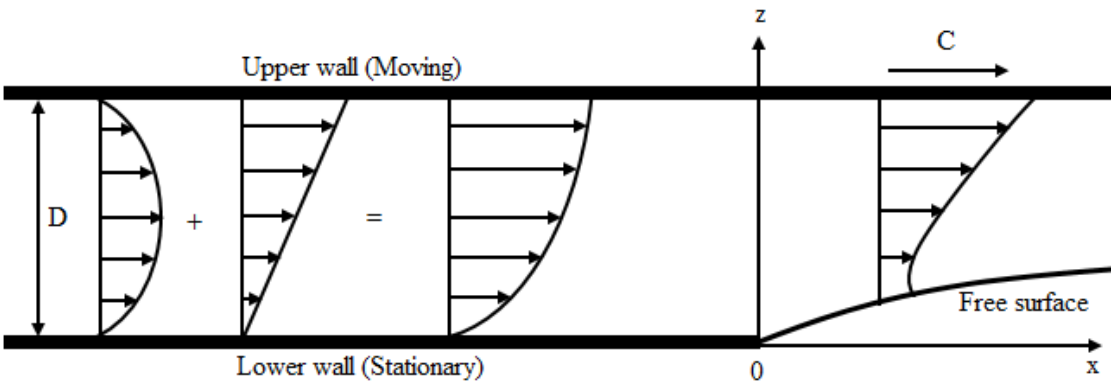

(b)

Figure 1.3: (a) Schematic illustrations of a typical blade coating process and (b) schematic illustrations of the analyzed domain of the blade coating process

The current work focuses mainly on the slot coating and the blade coating processes which involve adverse and favorable pressure gradients, respectively, in addition to the substrate movement. In the slot coating process, the coating liquid is pumped into the slot die, and it distributes through the narrow slot then it exits from the slot onto a moving substrate (figure 1.2 a). Part of the flow is being driven downstream by the moving substrate and part of it circulates upstream as a result of an imposed low-pressure area or vacuum that is often needed to facilitate faster and stable coating. This vacuum causes an adverse streamwise pressure gradient to act inside the channel formed between the downstream die and the moving substrate. Therefore, in that case, the flow inside the channel is a superposition of Couette (velocity driven), and Poiseuille (pressure driven) flows. On the other hand, in the blade coating, the flow is between a fixed blade of prescribed shape and a substrate moving parallel to itself (see figure 1.3 a). The coating liquid is dragged inside the channel by the moving substrate, which causes a hydrodynamic pressure rise at the nip of the blade. Due to the pressure rise, the blade rejects most of the liquid, and only a fraction passes into the narrow channel. Since the drag flow can only carry half of the coating liquid, a streamwise favorable pressure gradient is needed to carry the rest (Aidun et al. 1997). Thus, in this case, the pressure gradient pumps the coating liquid in the same direction as of the movement of the substrate inside the channel. Then, in both processes, the moving substrate drags the flow out of the channel in the form of a free surface wall jet, and thin layers of liquid films are obtained.

In the present study, the two coating processes are studied in a manner as illustrated schematically in the figures 1.2 b and 1.3 b, respectively. A channel is formed between the moving substrate and the slot die or blade, which is evident from these figures. Also, in both cases, the fluid encounters a free surface whenever it leaves the channel. Thus, a free surface moving wall jet is produced. Although the problem exhibits the challenges common to flow near a singularity, it becomes particularly simple far downstream of the channel exit as it becomes fully of the boundary-layer type. For this reason, it is helpful to first review the boundary layer flow for a moving wall jet (Schlichtling 2000) in an infinite medium (without a free surface).

1.2 Boundary layer theory

A boundary layer is a thin region where the viscous effects are important. Whenever fluid flows over a body, a thin boundary layer is formed close to the body surface due to no-slip condition. Ludwig Prandtl proposed this idea first in 1904.

In the boundary layer theory, the flow of a fluid at high Reynolds number (ratio of inertia to viscous forces) is divided into two different regions: a boundary layer where the flow shows significant viscous characteristics and an outer layer where the flow corresponds to inviscid flow. This division of the flow facilitates a considerable simplification in the theoretical analysis of the flows with high Reynolds number.

Now, consider the flow over a flat plate at a zero incidence, which is moving at a velocity, C (figure 1.3). The lengths are made dimensionless with length l (characteristic length in the streamwise direction), the velocities with C, and the pressure with ρC^2. Thus, the mass conservation and momentum equations for a steady two-dimensional incompressible flow in the non-dimension forms read,

$$\frac{\partial u}{\partial x}+\frac{\partial v}{\partial y}=0, \tag{1.2.1}$$

$$u\frac{\partial u}{\partial x}+v\frac{\partial u}{\partial y}=-\frac{\partial p}{\partial x}+\frac{1}{Re}\left(\frac{\partial^2 u}{\partial x^2}+\frac{\partial^2 u}{\partial y^2}\right), \tag{1.2.2}$$

$$u\frac{\partial v}{\partial x}+v\frac{\partial v}{\partial y}=-\frac{\partial p}{\partial y}+\frac{1}{Re}\left(\frac{\partial^2 v}{\partial x^2}+\frac{\partial^2 v}{\partial y^2}\right). \tag{1.2.3}$$

where u and v are the streamwise and transverse velocity components, respectively, Re is the Reynolds number and p is the pressure. If the limit $Re\to\infty$ is taken, the equations (1.2.2) and (1.2.3) will reduce to those for inviscid flow, and no-slip condition at the plate will not be satisfied. Therefore, to satisfy the no-slip at the plate, the viscous effect in the thin boundary layer close to the plate has to be considered. The order of magnitude of the above equations reveals that both the coordinate, y and velocity, v are of the order of

$O(\delta)$ where δ is thickness of the thin boundary layer. Consequently, these variables have small values in the boundary layer for $\delta \to 0$ or $\mathrm{Re} \to \infty$ and are not suitable to describe the boundary layer flow. Thus, they are scaled as follows:

$$\bar{y} = y\sqrt{\mathrm{Re}} \sim \frac{y}{\delta}, \qquad \bar{v} = v\sqrt{\mathrm{Re}}. \tag{1.2.4}$$

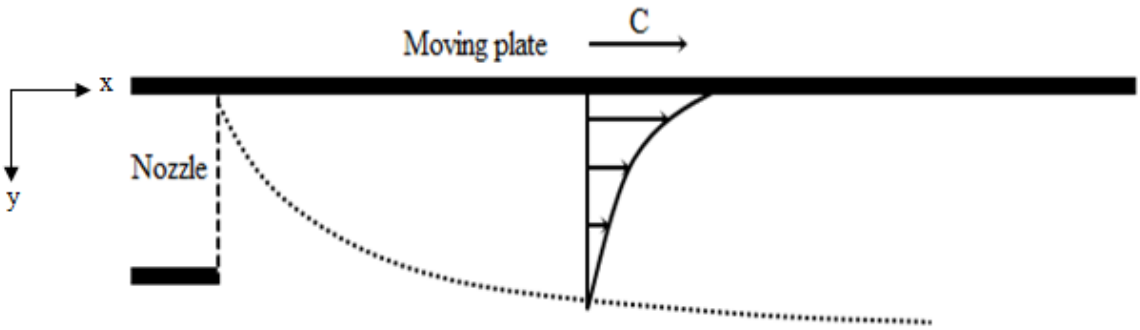

Figure 1.4: Schematic representation of the moving wall jet (Schlichting 2000).

This scaling makes the new variables the same order as x and u i.e. $O(1)$. Now, introducing the above-transformed variables into the expressions (1.2.1)-(1.2.3) and applying the limit $\mathrm{Re} \to \infty$ the following equations are obtained:

$$\frac{\partial u}{\partial x} + \frac{\partial \bar{v}}{\partial \bar{y}} = 0, \tag{1.2.5}$$

$$u\frac{\partial u}{\partial x} + \bar{v}\frac{\partial u}{\partial \bar{y}} = -\frac{\partial p}{\partial x} + \frac{\partial^2 u}{\partial \bar{y}^2}, \tag{1.2.6}$$

$$\frac{\partial p}{\partial \bar{y}} = 0. \tag{1.2.7}$$

The above equations are known as boundary layer or Prandtl boundary layer equations. Expression (1.2.7) implies that pressure is constant across the boundary layer. Consequently, it can be taken from the pressure at the outer layer, i.e. the pressure of the

inviscid flow is imposed in the boundary layer by the outer flow. Since the velocity gradients must vanish at the edge of the boundary layer, equation (1.2.6) becomes,

$$U\frac{\partial U}{\partial x} = -\frac{\partial p}{\partial x} \tag{1.2.8}$$

where U is the free stream/inviscid flow velocity in the outer layer. In this case, U is constant (U=0) which indicates that $\frac{dp}{dx} = 0$. Therefore, the boundary layer equations (in dimensional form) simplify to the following equations:

$$\frac{\partial u}{\partial x} + \frac{\partial v}{\partial y} = 0 \tag{1.2.9}$$

$$u\frac{\partial u}{\partial x} + v\frac{\partial u}{\partial y} = \nu\frac{\partial^2 u}{\partial y^2} \tag{1.2.10}$$

Here ν is the kinematic viscosity of the fluid. For a moving flat plate, the boundary conditions are the following:

$$y = 0: \quad u = C, \quad v = 0 \tag{1.2.11a}$$

$$y \to \infty: \qquad u = U = 0 \tag{1.2.11b}$$

The problems (1.2.9)-(1.2.11) admit a similarity solution, which means that the velocity profiles of the flow at different points are similar i.e. they can be plotted onto each other by using a suitable scaling factor. For a flat plate, using the Blasius (1908) scaling factor, $\eta \sim \frac{y}{\delta(x)}$ which is set as,

$$\eta = y\left(\frac{C}{2\nu x}\right)^{1/2} \tag{1.2.12}$$

Correspondingly, the stream functions is set as,

$$\psi = (2\nu x C)^{1/2} f(\eta) \tag{1.2.13}$$

Finally, substituting the variables η and ψ into the expression (1.2.9)-(1.2.11) leads to,

$$f''' + ff'' = 0 \tag{1.2.14}$$

Subject to the following boundary conditions:

$$\eta = 0: \quad f = 0, \quad f' = 1 \tag{1.2.15a}$$

$$\eta \to \infty: \qquad f' = 0 \tag{1.2.15b}$$

The development of the wall shear stress along the moving plate with distance is plotted in the figure 1.4. As the figure suggests, the shear stress decreases monotonically with distance. In particular, the stress exhibits a dramatic drop near the leading edge. A similar behavior is expected in the slot and blade coating processes near the channel exit where a singularity occurs as a result of a sudden drop in the shear stress at the exit; the shear stress suddenly vanishes at the free surface (see figures 1.1b and 1.2b).

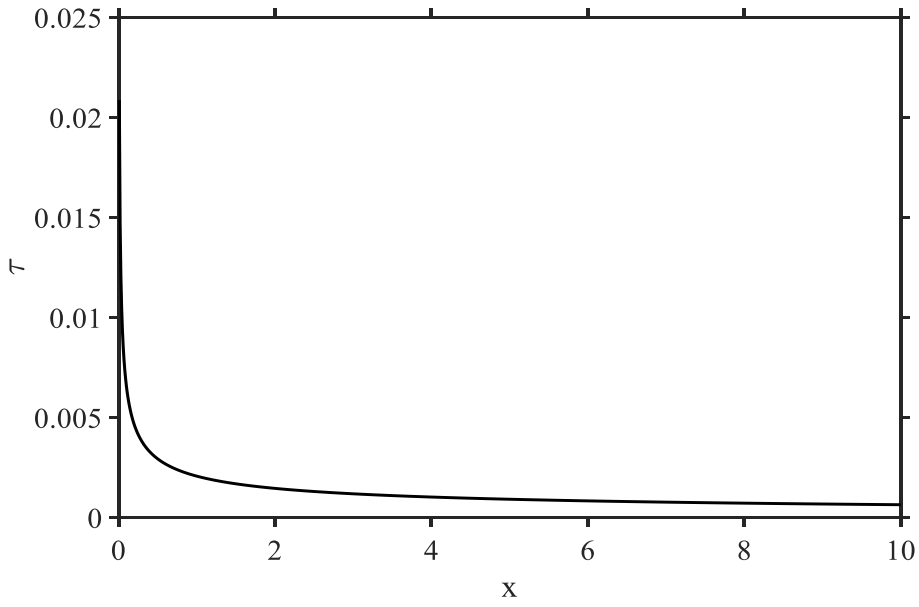

Figure 1.5: Shear stress distribution along the moving plate

1.3 A brief discussion on the solution strategy

The current work is based on the methodology developed by Tillett (1968) for the free surface symmetric jet flow at high Re. The flow configuration of Tillett's problem is depicted in the figure 1.5. From the figure it is evident that when the free surface jet emerges from the channel at the channel exit ($x = 0$), the wall shear stress undergoes a drastic change from a non-zero value at the lower wall ($z = 0$), to a value of zero at the free surface $\left(z = \zeta(x)\right)$. This removal of the wall shear stress causes a boundary layer to form in a region close to the free surface. In this region, the base velocity profile adjusts itself to satisfy the condition of zero traction at the free surface. Outside the boundary layer, the flow is assumed to have the base Poiseuille character to the lowest order, which begins to change when the fluid exits the channel in the form of a free jet. The solution of the problem is then constructed in powers of ε both in the 'inner' layer (boundary-layer) and in the 'core' layer, where ε is a small parameter in the problem defend as, $\varepsilon = \mathrm{Re}^{-1/3}$.

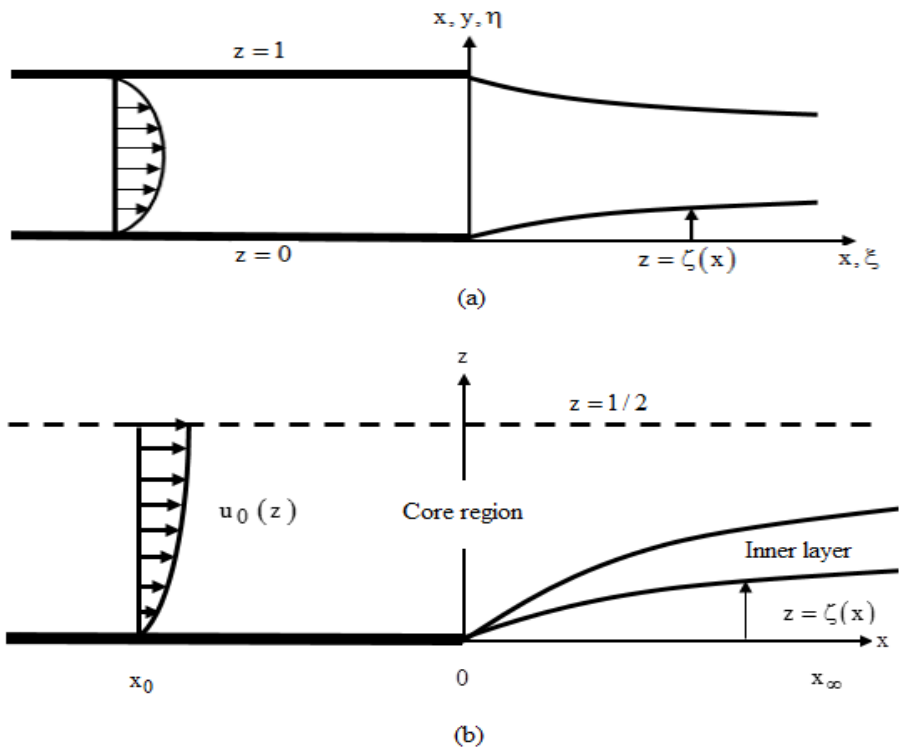

Figure 1.6: Schematic representation of (a) Tillett's (1968) free surface jet and (b) his region of study.

To investigate the problem, the X axis is considered along the lower edge of the channel and the Z axis in the transverse direction at the channel exit with the origin fixed at the exit. The stream function of the base Poiseuille flow inside the channel is,

$$\psi_0 = Z^2 - \frac{2}{3}Z^3. \tag{1.3.1}$$

The flow variables are non-dimensionalized by measuring the lengths with respect to channel width a, velocities with Aa, stream function with Aa^2 and pressure with $\rho A^2 a^2$. Here, $A = \frac{3\bar{u}}{a}$ and $\bar{u}$ is the mean velocity. The conservation of momentum equations in the non-dimensional forms read to,

$$\psi_z \psi_{xz} - \psi_x \psi_{zz} = -p_x + \frac{1}{Re}\left(\psi_{xxz} + \psi_{zzz}\right), \tag{1.3.2a}$$

$$\psi_x \psi_{xz} - \psi_z \psi_{xx} = -p_z - \frac{1}{Re}\left(\psi_{xxx} + \psi_{xzz}\right). \tag{1.3.2b}$$

The symmetry and wall conditions as well as the kinematic and dynamic boundary conditions at the free surface are to be satisfied (refer to the next section and Tillett (1968) for details). In order to solve the boundary layer flow close to the free surface, which is also called as inner layer, the following scaling variables are introduced,

$$x = \xi, \quad z = y + \zeta(x), \tag{1.3.3}$$

where, $y = \varepsilon\eta$ and $\zeta = \varepsilon h$. For matching with the core Poiseuille flow it is necessary that $\psi \sim y^2$ as $\eta \to \infty$, which leads to the following inner expansion for the stream function and pressure,

$$\psi = \varepsilon^2 \Psi_2 + \varepsilon^3 \Psi_3 + \cdots, \tag{1.3.4}$$

$$p = \varepsilon^4 P_3 + \varepsilon^5 P_4 + \cdots. \tag{1.3.5}$$

The following similarity solutions are found for Ψ_2 and Ψ_3:

$$\Psi_2 = \xi^{2/3} f_2(\theta), \qquad \Psi_3 = \xi f_3(\theta), \tag{1.3.6}$$

where, $\theta = \xi^{-1/3}\eta$ is the similarity variable. The equations and the boundary conditions for f_2 and f_3 are,

$$f_2''' + \frac{2}{3} f_2 f_2'' - \frac{1}{3} f_2'^2 = 0, \tag{1.3.7}$$

subject to $f_2(0) = f_2''(0) = 0$ and $f_2(\theta) \sim \theta^2$ as $\theta \to \infty$.

$$f_3''' + \frac{2}{3} f_2 f_3'' - f_2' f_3' + f_2'' f_3 = 0, \tag{1.3.8}$$

subject to $f_3(0) = f_3''(0) = 0$ and $f_2(\theta) \sim -\frac{2}{3}\theta^3$ as $\theta \to \infty$.

The third boundary conditions for both problems are obtained by matching the inner flow with the core flow at the edge of the boundary layer. The streamwise velocity at the free surface to the order $O\left(\varepsilon^3\right)$ becomes,

$$u\left(x, z = \zeta\right) = 2.5572\varepsilon x^{1/3} - 3.5878\varepsilon^2 x^{2/3}. \tag{1.3.9}$$

To examine the core flow the stream function and pressure are expressed as,

$$\psi = \psi_0 + \varepsilon\psi_1 + ..., \tag{1.3.10}$$

$$p = p_0 + \varepsilon p_1 + \cdots. \tag{1.3.11}$$

Here, ψ_0 is just the stream function of the base Poiseuille flow and higher order terms are the deviation from the basic flow. After substituting the above expansions into (1.3.2), to each order of ε different equations for stream function are obtained and by matching the

boundary layer flow onto the core at the edge of the boundary layer trivial solutions are found for both ψ_1 and ψ_2 .i.e. $\psi_1(x,z)=\psi_2(x,z)=0$. However, the ψ_3 equation provides a non-trivial problem due to the non-homogenous boundary condition $\psi_3(x,0)=-2x$. Using $w_3=-\psi_{nx}$, the following equation and boundary conditions are obtained in the core layer,

$$\nabla^2 w_3+\frac{2}{z(1-z)}w_3=0, \tag{1.3.12a}$$

$$\begin{aligned} &w_3\left(x,\frac{1}{2}\right)=0,\\ &w_3(x<0,0)=0, \qquad w_3(x>0,z\to 0)=-2, \end{aligned} \tag{1.3.12b}$$

where $\nabla=\frac{\partial}{\partial x}+\frac{\partial}{\partial z}$. Then, carrying out the variable separation method, the solution of the above equations both inside and outside the channel become,

$$w_3(x<0,z)=-\psi_{3x}=-\sum_{n=1}^{\infty}A_n e^{\beta_n x}V_n(z), \tag{1.3.13}$$

$$w_3(x>0,z)=-\psi_{3x}=-2V_0(z)+\sum_{n=1}^{\infty}A_n e^{-\beta_n x}V_n(z). \tag{1.3.14}$$

The coefficients A_n are obtained from matching the upstream and downstream core flows at the exit. The shape functions w_n are governed by the following eigen value (β_n) problem:

$$V_n''+\left(\beta_n^2+\frac{2}{z-z^2}\right)V_n=0, \qquad V_n(0)=V_n\left(\frac{1}{2}\right)=0. \tag{1.3.15}$$

The expressions of pressure inside and outside the channel are determined by using (1.3.13)-(1.3.15) which leads to, namely,

$$p_3(x<0,z) = -4x - 2\sum_{n=1}^{\infty} \frac{A_n}{\beta_n} e^{\beta_n x} \left\{ \left(z - z^2 \right) V_n' - (1-2z) V_n \right\}, \tag{1.3.16}$$

$$p_3(x<0,z) = -2\sum_{n=1}^{\infty} \frac{A_n}{\beta_n} e^{\beta_n x} \left\{ \left(z - z^2 \right) V_n' - (1-2z) V_n \right\}. \tag{1.3.17}$$

The flow has been matched in different layer by adopting the matching rule of Van Dyke (1964) which is expressed as, $E_n H_m \psi = H_m E_n \psi$. Here, E_n and H_m are corresponding inner and core expansion operators, respectively. Not only the additional boundary conditions needed to solve problems in different layers but also the shape of the free surface is attained from the matching. The surface height up to $O\left(\varepsilon^3\right)$ is given by,

$$\zeta(x) = 0.70798\varepsilon x^{1/3} - 1.04457\varepsilon^2 x^{2/3}. \tag{1.3.18}$$

Finally, by applying Van Dyke's composite expansion $\left(C_n \equiv E_n + H_n - E_n H_n\right)$, the following composite streamwise velocity is obtained:

$$C_2 u = \varepsilon x^{1/3} f_2'(\theta) + \varepsilon^2 x^{2/3} f_3'(\theta) + O\left(\varepsilon^3\right). \tag{1.3.19}$$

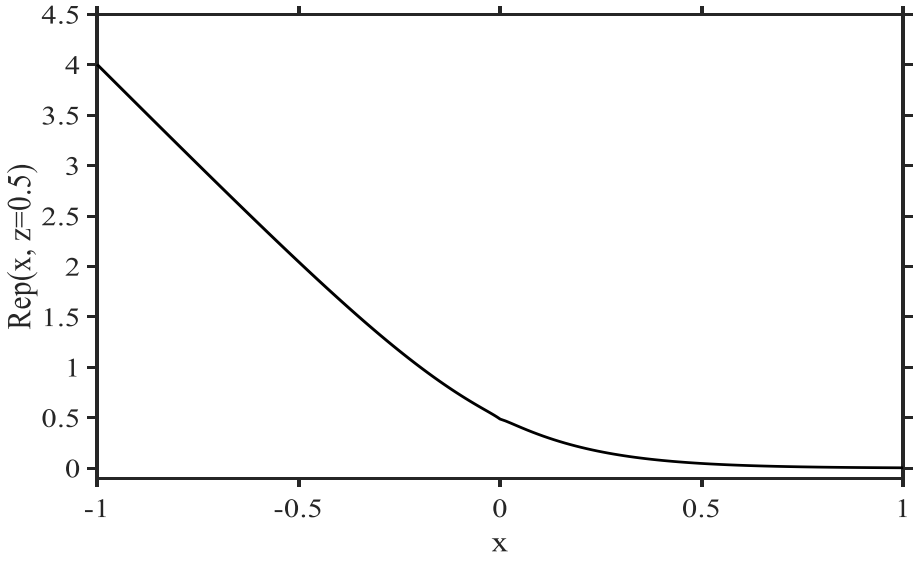

Figure 1.7: Pressure development along the centerline with distance x (Tillett 1968).

The pressure profile along the centerline is plotted against the distance x in figure 1.6. From the figure, it is clear that the pressure retains its Poiseuille level inside the channel except very close to the channel exit. This behavior will be contrasted with the pressure distribution for the coating process.

From the figures 1.2 b, 1.3 b and 1.5, it is visible that as the fluid emerges from the channel in the form of a jet, it experiences a drastic change in the shear stress level at the channel exit, i.e. the value of shear stress suddenly becomes zero on the free surface from a finite value at the wall which causes a stress singularity to form. This type of singularity produces a major hindrance in the theoretical methodology. On the other hand, the inclusion of the singularity and its immediate surroundings is inevitable if a computational scheme is implemented because of the need for whole domain discretization (Saffari and Khayat 2008). The singularity region affects the rest of the flow in the domain significantly and is difficult to handle numerically if a satisfactory level of accuracy is required. On the contrary, due to the similarity nature of the flow near the free surface, asymptotic analysis can become a viable alternative since the singularity is circumvented completely in the formulation (Khayat 2014; Khayat 2017).

Interfacial and free surface flows are intrinsically complex because of the unknown location/shape of the free surface. Incidentally, the presence of stress singularity with the free surface makes both the problem and solution substantially more complicated. A combination of numerical and analytical schemes has also been proposed for tackling this type of problem (Shi et al. 2004). Although mesh refinement provides higher accuracy by capturing the singularity more effectively, at the same time, it leads to the presence of stronger flow gradients that are difficult to handle numerically (Pasquali & Scriven 2002). By writing the flow equations in the curvilinear coordinate system, Tsukiji and Takahashi (1987) avoided the difficulty associated with the unknown free surface. However, their approach complicates the flow equations. On the other hand, perhaps, the asymptotic analysis provides a deeper understanding of the flow structure near the singularity by identifying two distinct regions: a boundary layer close to the free surface, which extends without including the singularity point, and a core region where the flow remains almost fully developed. In this case, the insertion of the singularity is not essential given the

similarity characteristics of the flow in the boundary layer close to the free surface. Asymptotic analysis has been implemented successfully for flows in the visco-capillary limit (Goren and Wronski 1966; Ruschak and Scriven 1977; Higgins 1982; Benilov et al. 2008) and in the visco-inertia limit close to the present study (Tillett 1968; Philippe and Dumargue 1991; Khayat 2017). Miyake et al. (1979) carried out a similar approach for a vertical jet falling under the influence of gravity. Wilson (1986) applied a local similarity transformation for the axisymmetric viscous-gravity jet of the boundary layer type flow near the free surface. For the non-Newtonian flow, for instance, see the works of Zhao and Khayat (2008), Saffari and Khayat (2008) and Khayat (2014). More recently, using the asymptotic approach, Khayat (2016 a, b) investigated the jet flow coming out from a hydrophobic channel.

1.4 Historical overview on coating flows

The coating is a process where a thin layer of liquid is applied to a solid/flexible moving substrate (Weinstein & Ruschak, 2004). In other words, a thin layer of liquid displaces the gas at a solid substrate (rigid/flexible), often moving (Iliopoulos & Scriven, 2005). This process is present in numerous industries (Fig 1.7).

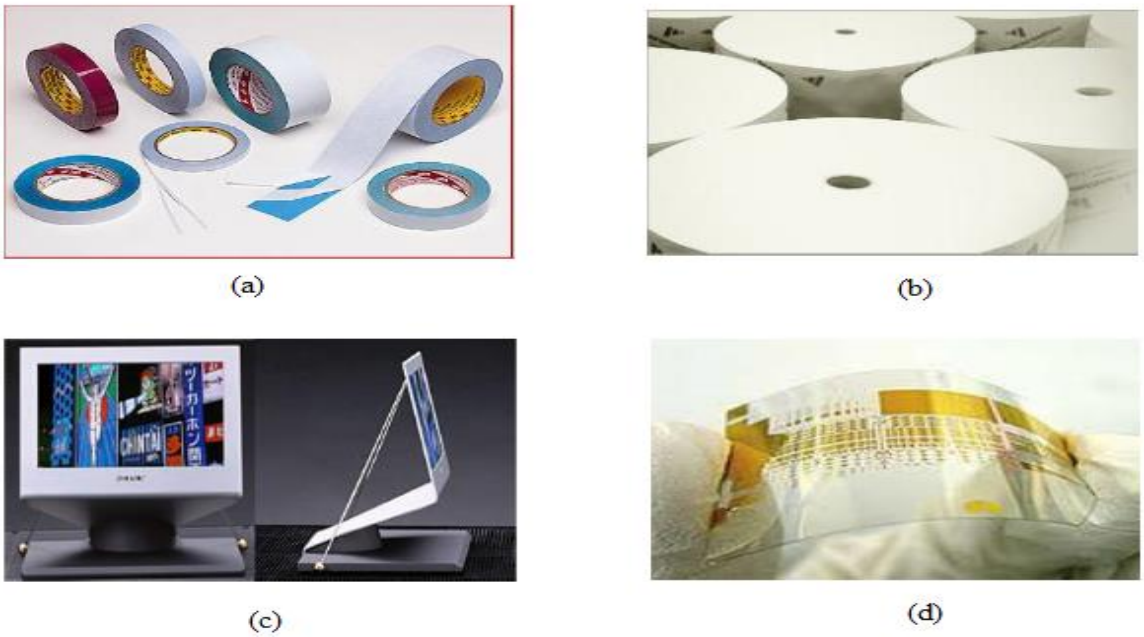

Figure 1.8: Different applications of coating processes (a) adhesive tapes, (b) paper, (c) thin displays and (d) transparent printed electronics (Araujo and Carvalho 2014).

For instance, food, textile, paper, adhesive tapes, magnetic disks and even in flexible and transparent electronics and thin displays (Araujo and Carvalho 2014; Lee et al. 2016; Maillard et al. 2016). Although various coating processes are currently available, they can be broadly categorized as the pre-metered or self-metered coating. Blade, dip and roll coating fall into the category of self-metered coating whereas slot, curtain and slide coating into the pre-metered one. As in the case of self-meter process, the thickness of the coating film depends as a whole on the geometry, liquid properties, and web speed. However, in a pre-metered process, the flow rate setting directly determines the coating thickness without the influence of the earlier mentioned parameters (Weinstein & Ruschak, 2004; Ruschak 1985).

Due to its importance in various industrial production processes, coating flow has been studied extensively in the past several decades. Ruschak (1976) performed a theoretical analysis based on film theory of Landau and Levich (1962) to determine the flow limit (effects of different parameters) of extrusion slot coating for the Newtonian fluid. In his work, he considered very small Capillary number by setting the coating speed close to zero. The Capillary number (Ca) is the ratio between the viscous to surface tension forces defined as, $\mathrm{Ca} = \frac{\mu V}{\sigma}$ where, μ is the viscosity, V is the coating speed and σ is the surface tension. To find out the film thickness in the slow flow (negligible inertia) limit he carried out a singular perturbation method and observed that film thickness became thinner with the smaller value of the Capillary number. He also noticed that gravity did not affect the flow much in the limit considered in the study. Higgins and Scriven (1980) extended Ruschak's analysis by incorporating the viscous effect in the coating bead (inside the channel) with variable meniscus location. They concluded that as the coating speed became higher, the dynamic contact angle increases which altered the coating behavior. Saito and Scriven (1981) carried out a finite element analysis on slot coating flow to examine the Capillary number effect on the curved meniscus close to static contact line and, showed that the downstream meniscus no longer remains attached with the slot at the higher Capillary number and lower flow rate. Through experiment, Lee et al. (1992) determined the minimum wet thickness for extrusion slot coating. In their experiment, the range of Reynolds number (Re) was low, i.e. from 0.2 to 24. The Reynolds number is the ratio of

inertia versus viscous forces expressed as $\mathrm{Re} = \frac{\rho V h}{\mu}$ where ρ is the fluid density, V is coating speed and h is the minimum coating thickness. The experiment was conducted using two different fluids: Glycerin-water solution and standard silicon oil. The minimum coating thickness was calculated using the formula, $h = \frac{Q}{VB}$ where Q is the volumetric flow rate in the slot die and B is the coating width. They noticed that there exists a critical Ca corresponding to each of the examined coating gaps. Beyond the critical Ca, the minimum wet thickness became constant regardless of the value of Ca. However, below the critical Ca, strong dependency on Ca was found. In addition, in the limit of their coating conditions, gravity influence on the minimum wet thickness was insignificant. Following the work of Lee et al. (1992), using the highly viscous fluid in the slot coater, Yu et al. (1995) investigated the possibility to reduce the minimum wet thickness. Interestingly, they found out that it is achievable if a low viscous fluid is used as a bottom carrier layer. Chang et al. (2007) investigated the slot coating process experimentally for low viscous fluid. In their experiment, a flow visualization technique was used to determine both the downstream and upstream meniscus and their effects on coating thickness. Three separate coating regions were viewed based on the fluid, die geometry and flow conditions. Beyond a critical Reynolds number (Re=20), both viscous and surface tension effects became negligible, and inertia dominated the flow. Ashmore et al. (2007) predicted the final film thickness of slot coating flow for different substrate geometry and non-Newtonian fluids at low Reynolds number (approximately from 0.6 to 12). They used a combination of the lubrication theory and the asymptotic approach for the study. It was observed that the elastic stress became significant in the strongly elastic limit. In turn, this dominated the film thickness behavior over the surface tension and viscous effects. However, the opposite trend was seen for the weakly elastic limit case.

The low-flow limit is an important aspect for slot coating, which is defined as the maximum substrate speed possible without any coating defects at a fixed minimum thickness or vice versa (Carvalho and Kheshgi, 2000). By modifying the viscocapillary model, Carvalho and Kheshgi (2000) developed a 2D numerical tool to study the effect of higher Capillary numbers in the low-flow limit of slot coating flow. At higher Capillary number ($Ca > 0.3$

), inertia started to dominate the flow. In fact, it delayed the onset of low-flow limit. By considering low Capillary and vanishing Reynolds numbers, Romero et al. (2004) conducted a study on the slot coating flow for a polymer solution to predict the low-flow limit. The minimum coating thickness increased as the fluid became more shear thickening. Again, Romero et al. (2006) investigated the onset of the low-flow limit of slot coating flow but this time using mildly viscoelastic fluid. Their results confirmed that for low Weissenberg number (ratio of elastic force to viscous force) and less flexible polymer molecules, the coating window (minimum thickness and maximum speed possible) was wider compared to the Newtonian fluid. Using a flow visualization technique, Lin et al. (2010) investigated the validity of a commercial 2D numerical simulation package on predicting the coating window for slot coating and, showed that the theoretical maximum coating speed without any defects was higher than the experimental one. More recently, Jang et al. (2013) proposed a model for slot coating by modifying the viscocapillary model to accommodate the high Capillary and to some extent inertia effects. Unlike the viscocapillary model, they had taken account of the pressure variation under the slot die, which enabled them to predict coating thickness at high Capillary and Reynolds numbers. They observed that when $\mathrm{Re} > 10$ due to significant inertia effect the film thickness decreased with increasing inertia and viscocapillary model did not show good agreement with the simulation at the higher Capillary number ($\mathrm{Ca} > 0.2$).

The experimental study conducted by Chu et al. (2006) analyzed the effect of inorganic particles and polymer additives in the slot coating flow. It was concluded that strong interactions of the polymer and additive particles extended the coating window by stabilizing the coating bead significantly. Moreover, the dimensionless coating thickness became constant for $\mathrm{Ca} > 0.1$. For the simulation, the coating speed was 0.55 m/s, which corresponds to Re around 12.16. In terms of Elastocapillary number, Bajaj et al. (2008) examined the influence of viscoelasticity of dilute polymer solutions on the slot coating flow (negligible inertia) and, concluded that increase in the fluid elasticity narrowed down the window for uniform coating. Chang et al. (2009) examined the start-up of slot coating flow. In particular, the effects of prewetting, viscosity, slot gap, coating gap and die lip length on start-up were investigated. Here, the Reynolds number was expressed as,

$\mathrm{Re} = \dfrac{\rho V_s^2}{\mu V_w / H}$ where V_s is the average speed in the slot, V_w is the speed of the substrate and H is coating gap. The ranges were from 1 to 47 for Reynolds number and from 0.02 to 0.11 for the Capillary number. They found out that coating surface prewetting plays an important role in reducing the start-up time requirement to reach steady state. In addition, at low Reynolds number, the formation of a steady upstream meniscus was quicker than the downstream one whereas at high Reynolds number the steady downstream meniscus formed first.

Earlier studies of Sullivan and Middleman (1986, 1987) on the blade coating were conducted to understand the fluid rheology and blade geometry effects on the coating performance. Both of the studies problem formulations were based on the classical lubrication theory of Cameron (1966). In the first, by neglecting gravity and inertia effects, it was found that the relative magnitude of shear thinning and elastic behaviors determined the limit of coating thickness. Extension of the computational domain, different pressure boundary condition, inertia and surface tension were incorporated in the second study. It was noticed that coating thickness became independent of the geometric parameters for highly elastic Boger fluid while a strong dependency was found for the Newtonian counterpart. In this investigation, they considered $\mathrm{Re} = 0.9$ and $\mathrm{Ca} < 4$, respectively. Pranckh and Scriven (1990) investigated the interactions of the blade, liquid and loading inside a blade coater from the elastrohydrodynamic point of view using lubrication and shell theory. Their theory provided a better approach than Saito and Scriven (1985) to predict the key principles that govern the deformation of the blade. Ro and Homsy (1995) carried out a double perturbation expansion for the small capillary number and Weissenberg number for Hele-Shaw flow by neglecting both gravity and inertia effects. They concluded that manifestation of the normal stress near the exit increased the film thickness. Ross et al. (1999) examined the blade coating flow between the blade and moving substrate for both Newtonian and non-Newtonian fluids using the lubrication theory (negligible inertia). They found that the blade geometry controlled the impact of weakly non-Newtonian and its Newtonian counterpart on the flow. Lee et al. (2002) examined the viscoelasticity effect on the free surface profile near the exit in the slot

coating flow for low to moderate Weissenberg number. In the low flow limit $(\mathrm{Re}=0)$, they observed that viscoelasticity was triggered by the onset of stress boundary layer at the interface. Consequently, a thicker film was obtained. Lliopoulos and Scriven (2005) studied the blade coating process numerically by focusing the influence of particle suspensions on the blade and substrate. Two types of blade geometry: trailing stiff and plowing were considered in the study. In addition, the applicability of the elastohydrodynamic theory of blade coating was broadened by including wear of the blades. They found out that the coating thickness increased with the Reynolds number. The same scenario was observed for the higher Capillary number. In fact, the coating thickness tapered off at the higher Capillary number. In their study, the approximate ranges of the two numbers were, respectively, $0<\mathrm{Re}<55$ and $10<\mathrm{Ca}<30$. Mitsoulis and Athanasopoulos (2010) examined the blade coating process for different blade geometry and fluid property. They found that low shear thinning $(\mathrm{n}>0.3)$ increased the film thickness while high shear thinning $(\mathrm{n}<0.3)$ decreased the film thickness.

1.5 Motivation

The use of printed electronics and thin photographic films are increasing day by day due to their involvement in the production of thin displays, solar cells, and electrodes for lithium-ion batteries. Typically, the production of these products involves high-speed coating processes such as the slot coating and the blade coating. The range of the coating speed can vary approximately from 5 m/min to 100 m/min in those processes. At this coating speed, inertia effect becomes significant (high Reynolds number) due to the lower viscosity of the coating fluid $(<20\,\mathrm{mPas})$ (Chang et al. 2007; Hong et al. 2013; Jang and Song 2013). The increase in Reynolds number can be illustrated by the following two examples. First, taking the values of the coating speed (C), fluid viscosity (μ), density (ρ) and coating gap (D) from Chang et al. (2007) as 10 m/s, 10 mPa s, 1151 kg/m^3 and 0.0002 m, respectively. In this case, the calculated Reynolds number $\left(\mathrm{Re}=\frac{\rho \mathrm{CD}}{\mu}\right)$ becomes 230. Now, from Chu et al. (2006), the corresponding values are 2 m/s, 11.7 mPa s (obtained at a nominal shear rate of 1000 s^{-1}), 1030 kg/m^3 and 0.0003 m. Consequently, the value of Reynolds number reads 53. The magnitudes of the pressure gradients in the above cases in

terms of non-dimensional pressure gradient G are 0.1 and 0.3, respectively. It is clear from the above examples that inertia must be considered in the high-speed coating processes to get a better understanding of the flow behaviors. In the current analysis, a mathematical model has been developed for the slot, and the blade coating flows by considering moderate inertia effect, i.e. moderate Reynolds number (Reynolds number approximately from 10 to a few hundred), which has been neglected in the previous studies.

Another important aspect in the theoretical analysis of the coating flows is the presence of the singularity at the channel exit. As discussed before, capturing this singularity is numerically difficult, yet necessary for more accurate prediction and a better understanding of the flow behavior outside the channel. However, most of the numerical studies on the coating flow overlooked this singularity effect in their formulation. For example, Mitsoulis (2010) conducted a numerical simulation of the blade coating process using the finite element analysis. From the figures 6 to 8 of Mitsoulis (2010), it is evident that not only the shear stress but also the pressure and the normal stress exhibit a singularity at the channel exit. This cannot be ignored since the singularity dominates the flow close to the exit, which eventually determines the accuracy of the prediction of the coating thickness and flow. In addition, numerical schemes tend to smooth out the singularity whereas the asymptotic approach used in the present study provides a better understanding of the flow in the vicinity of the singularity.

1.6 Summary

In conclusion, the current chapter introduces the problem in a general manner by focusing on the slot and the blade coating processes. The flow characteristic near the channel exit governs the flow nature further downstream where the free surface jet acquires a uniform thickness. Moreover, the presence of stress singularity and unknown shape of the free surface complicates the problem. In the next chapter, a mathematical model will be developed to capture the singularity along with the shape of the free surface under the action of moderate inertia. It is expected that the present study will help the coating industries by enhancing the understanding of the singularity and responses of the velocity fields, free surface shape and the stress fields to the singularity.

Chapter 2

2 Free surface moving wall jet flow near the channel exit

2.1 Problem formulation

Consider the flow of an incompressible fluid emerging out from a two-dimensional channel of width D with fluid density ρ and fluid viscosity μ. The fluid properties correspond to the Newtonian fluid. In the figure 2.1, the flow configuration is schematically depicted in the (X, Z) plane . The X-axis is considered along with the lower stationary wall, and the Z-axis is taken across the channel in the transverse direction. The channel exit coincides at X=0 which is the origin for both axes. Note that the upper case letters represent the dimensional form whereas lower case letters denote the non-dimensional form. The fluid is depositing on the forward moving wall, which is moving at a velocity C in the positive X direction. The flow is driven by the simultaneous action of the translation of the upper wall and an applied adverse or favorable pressure gradient (dP/dX) inside the channel and, i.e. Couette-Poiseuille flow. The stream function of the base Couette-Poiseuille flow becomes,

$$\Psi = \frac{1}{2\mu}\frac{dP}{dX}\left(\frac{Z^3}{3} - D\frac{Z^2}{2}\right) + \frac{CZ^2}{2D}. \qquad (2.1.1)$$

Non-dimensional variables are introduced by measuring the lengths with respect to channel width, D, stream function with respect to CD and pressure with respect to ρC^2.

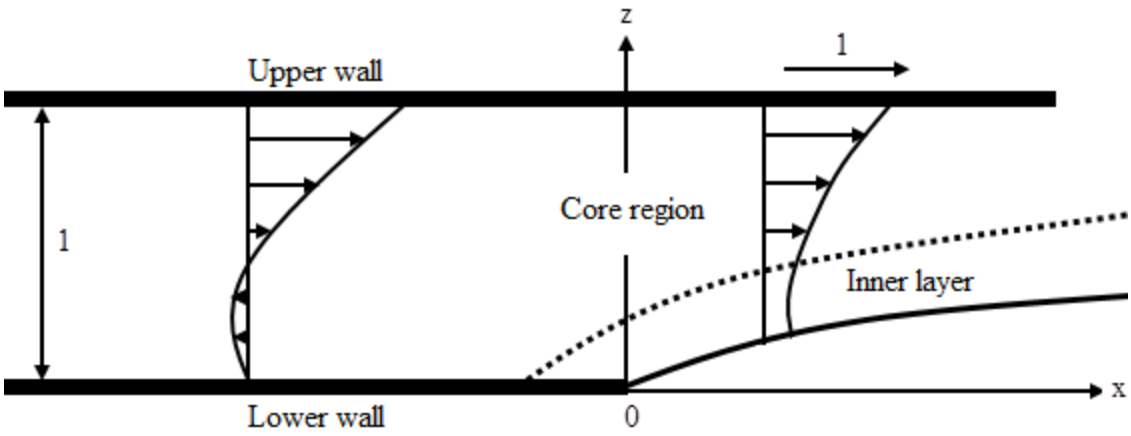

(a)

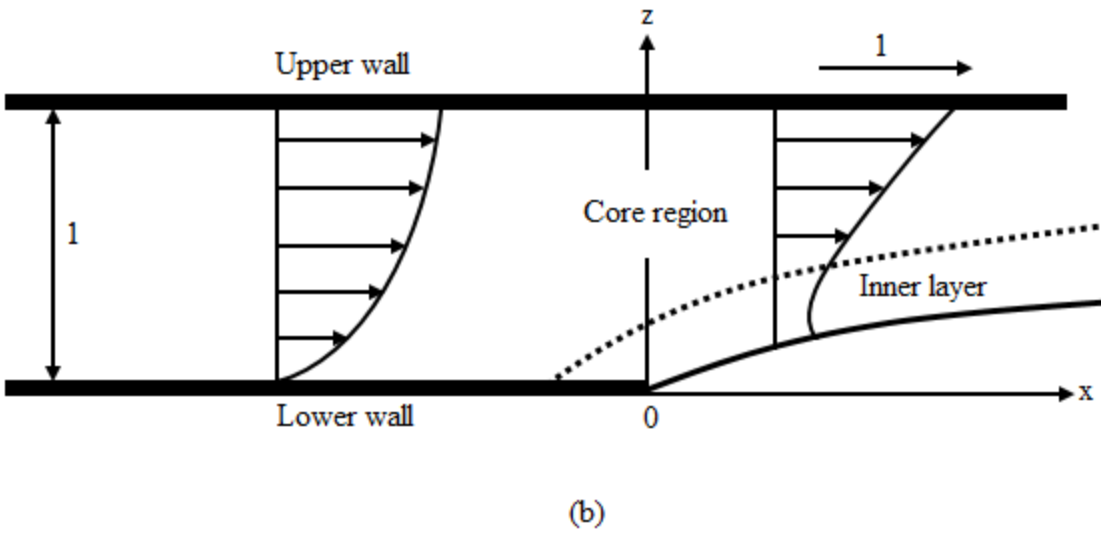

Figure 2.1: Schematic illustration of the free surface wall jet of (a) the slot coating and (b) the blade coating (dimensionless notions are used).

In the current problem, two major dimensionless parameters appear, namely, Reynolds number, Re and the non-dimensional pressure gradient, G and are expressed as,

$$\mathrm{Re} = \frac{\rho C D}{\mu}, \qquad G = \frac{D^2}{2\mu C}\frac{dP}{dx}. \tag{2.1.2}$$

Thus, the equation (2.1.1) will turn out to be the leading order solution in the core region and is conveniently introduced here as,

$$\psi_0(z) = (1-G)\frac{z^2}{2} + G\frac{z^3}{3}. \tag{2.1.3}$$

In the current study, the Reynolds number, Re is assumed to be moderately large and $G = O(1)$. If $G = 0$, the flow is only driven by the forward wall translation and if $G \to -\infty$ or $G \to \infty$, is solely induced by the pressure gradient. Typically, the value of G varies from -0.05 to -0.20 in the blade coating process and from 0.05 to 0.20 in the slot coating process (Llipoulos and Scriven 2005; Mitsoulis 2010; Chin et al. 2010, Lin et al. 2010). For a steady laminar two-dimensional flow, the non-dimensional conservation of momentum equations take the following forms:

$$\psi_z\psi_{xz} - \psi_x\psi_{zz} = -p_x + \frac{1}{Re}\left(\psi_{xxz} + \psi_{zzz}\right), \tag{2.1.4a}$$

$$\psi_x\psi_{xz} - \psi_z\psi_{xx} = -p_z - \frac{1}{Re}\left(\psi_{xxx} + \psi_{xzz}\right). \tag{2.1.4b}$$

2.2 The Kinematic and dynamic boundary conditions on the free surface

The kinematic boundary condition implies that the normal velocity of the particle on the free surface follows the normal velocity of the surface itself. In other words, the fluid does not cross the free surface (Middleman 1995).

The dynamic boundary condition (see figure 2.2) on the free surface means that there is no traction on the free surface i.e. $\vec{F} = \vec{\sigma}\cdot\vec{n} = 0$.

Therefore, we can write,

$$\left(\vec{F}\cdot n\right)_x = \sigma_{xx}n_x + \sigma_{xz}n_z = 0, \tag{2.2.1}$$

$$\left(\vec{F}\cdot n\right)_z = \sigma_{zx}n_x + \sigma_{zz}n_z = 0. \tag{2.2.2}$$

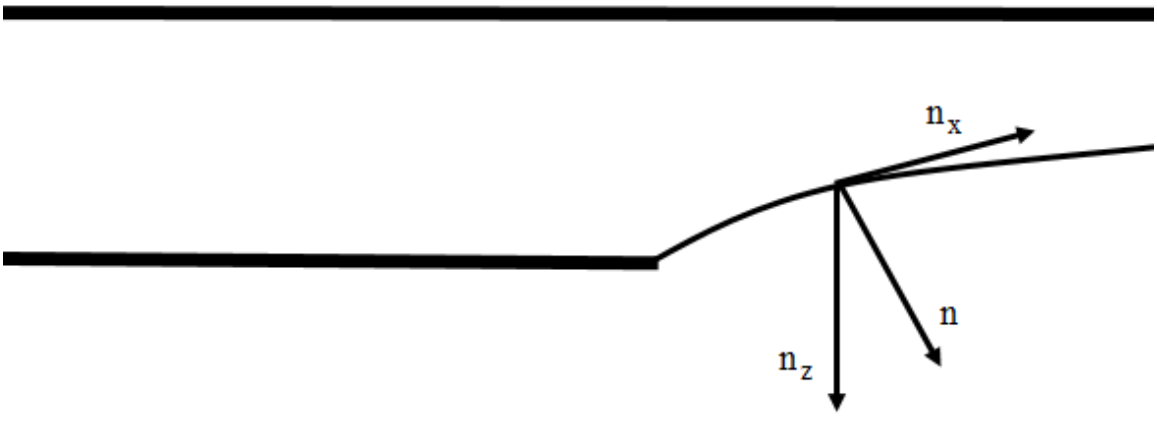

Figure 2.2: Schematic representation of the dynamic boundary condition on the free surface.

For the Newtonian viscous fluid,

$$\sigma_{xx} = -\mathrm{Re}\,p + 2\frac{\partial u}{\partial x} = -\mathrm{Re}\,p + 2\psi_{xz}, \tag{2.2.3}$$

$$\sigma_{xz} = \sigma_{zx} = \frac{\partial u}{\partial z} + \frac{\partial w}{\partial x} = \psi_{zz} - \psi_{xx}, \tag{2.2.4}$$

$$\sigma_{zz} = -\mathrm{Re}\,p + 2\frac{\partial w}{\partial z} = -p - 2\psi_{zx}. \tag{2.2.5}$$

The components of normal $\vec{n}$ are given by,

$$n_x = \frac{\zeta'}{\sqrt{\zeta'^2 + 1}} \text{ and } n_z = -\frac{1}{\sqrt{\zeta'^2 + 1}}. \tag{2.2.6}$$

From now on, the subscript denotes the partial differentiation. Substituting the expressions (2.2.3)-(2.2.5) into the equations (2.2.1) and (2.2.2), and after rearranging the terms the following equations are obtained:

$$p\zeta' - \frac{1}{\mathrm{Re}}\left(2\zeta'\psi_{xz} - \psi_{zz} + \psi_{xx}\right) = 0, \tag{2.2.7}$$

$$p + \frac{1}{\mathrm{Re}}\left[\left(\psi_{zz} - \psi_{xx}\right)\zeta' + 2\psi_{zx}\right] = 0. \tag{2.2.8}$$

Finally, for $x > 0$, the kinematic and dynamic boundary conditions at the free surface, $z = \zeta(x)$, are,

$$\psi = 0, \tag{2.2.9a}$$

$$p\zeta' - \frac{1}{\mathrm{Re}}\left(2\zeta'\psi_{xz} - \psi_{zz} + \psi_{xx}\right) = 0, \tag{2.2.9b}$$

$$p + \frac{1}{\mathrm{Re}}\left[\left(\psi_{zz} - \psi_{xx}\right)\zeta' + 2\psi_{zx}\right] = 0. \tag{2.2.9c}$$

Here, a prime denotes total differentiation. Inside the channel $(x < 0)$, the following conditions must be satisfied:

$$\psi_z = 1, \qquad \psi = \left(1 - \frac{G}{6}\right), \quad \text{at} \qquad z = 1, \tag{2.2.10a}$$

$$\psi_z = 0, \qquad \psi = 0, \qquad \text{at} \qquad z=0, \tag{2.2.10b}$$

$$\psi\left(x \to -\infty, z\right) \to \left(1-G\right)\frac{z^2}{2} + G\frac{z^3}{3} \quad \text{as} \qquad x \to -\infty. \tag{2.2.10c}$$

To the lowest order, it is assumed that the flow retains its base Couette-Poisueille profile (2.1.3). Due to the presence of a stress singularity at the exit, the flow behavior changes as it comes out from the channel in the form of a free surface wall jet. This condition would not be imposed in the proper inviscid limit since there is no mechanism (viscous) exists that diffuses the stress singularity. Then all the conditions of the problem would be satisfied by simply postulating that the base profile stays unchanged in the whole jet region (similar to a Newtonian free jet (Tillett 1968)). However, no uniqueness theorem exists for this inviscid problem. It is plausible that other solutions might exist. Nevertheless, in the present study, it is assumed that the fully developed Couette-Poiseuille flow is everywhere in the proper inviscid limit (see also Saffari & Khayat (2008) for the viscoelastic case). By implementing this assumption, to the lowest order, it can be concluded that the flow in the core of the jet is not affected by the flow in the boundary layer region close to the free surface. However, it is expected that the boundary layer induce perturbations to the base Couette-Poiseuille flow, when the higher order terms are included, both for the flow upstream and downstream of the channel exit. This postulation is analogous to the one made by Smith (1979) for the tube flow with severe constriction. In Smith's case, the core flow also satisfies the inviscid flow equations to the leading order. Further discussion on the current and Smith's formulation is provided in section 2.5. Other asymptotic studies on the interactive boundary layers are discussed in the book by Sobey (2005). When the fluid detaches itself from the wall of the channel, a boundary layer is formed very close to the free surface due to the vanishing of the wall shear stress at the exit, which is denoted here as a *free surface or inner* layer. This thin layer and the jet contraction (or expansion) affect the *core* of the jet, with the core layer remaining predominantly of the inviscid rotational character.

This inviscid layer cannot extend to the moving upper wall, where significant viscous shearing occurs, forcing the formation of an *upper-wall layer* near the moving upper wall. Similarly, the core flow must also adjust to the viscous shearing flow in the *lower-wall layer* upstream of the stress singularity at the exit. In other words, given the predominantly inviscid character of the core flow, the core solution cannot satisfy the no-slip condition at both walls (Khayat 2017). Different flow regions for the moving wall jet are shown schematically in the figure 2.3. In each of the region, different physical mechanisms dominate the flow with corresponding characteristic length scales. In particular, the flow in the region close to the free surface downstream of the channel exit, i.e. the *inner* region, is shear dominated by boundary layer characteristics.

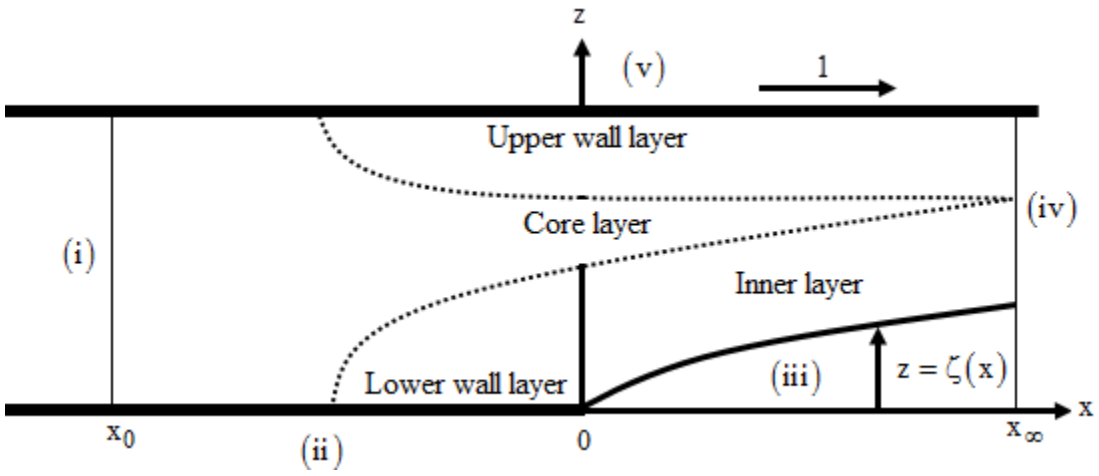

Figure 2.3: Schematic depiction of the computational domain (all notations are dimensionless). The boundary layers are depicted along the free surface (dotted lines), upper wall and lower wall. Five segments of the control volume analysis are also shown.

In between the inner region and the moving wall, the *core* region, both shear ($\frac{\partial u}{\partial z}$) and elongation ($\frac{\partial u}{\partial x}$) prevail because of the high proportion of the Couette-Poiseuille character of the flow and contraction of the jet. The core region also extends to upstream from the channel exit. The effect of the drop in shear stress diffuses upstream inside the channel ($x < 0$) over a distance x_0 where fully developed Couette-Poiseuille flow is recovered, and downstream $(x > 0)$ towards the moving wall over a distance x_∞, at which point the flow

is entirely of the boundary layer type. Near the free surface and lower wall, boundary layer type solutions are determined. Outside the channel, a similarity solution is sought in the inner layer, which is then matched onto the core solution outside of the exit. After that, the outside core flow is matched onto the solution in the core region inside the channel. An important observation is that between the inner and lower-wall layers no matching is required for the similarity flow at $x = 0$. The inclusion of the singularity is not essential here because of the similarity nature of the flow. This constitutes a major advantage of the current formulation. As discussed before, part of the formulation in each layer is similar to the symmetric free jet formulation carried out by Tillett (1968).

2.3 Flow in the free-surface or inner layer

A change in coordinate is introduced by letting $y = z - \zeta(x)$ to examine the boundary layer structure close to the free surface. In addition, the scaling in the transverse direction is changed by writing $y = \varepsilon\eta$, where $\varepsilon = Re^{-\alpha}$ is the small parameter in the present problem and the value of α is to be determined. One can write $\zeta(x) = \varepsilon h(x)$ by assuming that the height ζ of the free surface is of the same order of magnitude as the boundary layer thickness h and hereafter work with h. It is not necessary to assume that $h(x) = O(1)$ as $\varepsilon \to 0$; examination of the equation (2.3.2a) shows that the inner expansion developed in the current section holds only when $h = o\left(\varepsilon^{-1}\right)$, i.e. ζ tends to 0 with ε. In the matching section it will be shown that indeed $h = O(1)$. Now, following Tillett (1968) and Philippe & Dumargue (1991), the following change in coordinates is introduced, namely,

$$x = \xi, \qquad z = \varepsilon(\eta + h). \tag{2.3.1}$$

Substituting the transformed variables into equations (2.1.4a) and (2.1.4b) and after making the necessary rearrangement, it is concluded that,

$$\psi_\eta\psi_{\xi\eta}-\psi_\xi\psi_{\eta\eta}=-\varepsilon^2\left(p_\xi-h'p_\eta\right)+\varepsilon^{\left(\frac{1}{\alpha}-1\right)}\psi_{\eta\eta\eta}+\varepsilon^{\left(\frac{1}{\alpha}+1\right)}\left(\psi_{\xi\xi\eta}-2h'\psi_{\xi\eta\eta}+h'^2\psi_{\eta\eta\eta}-h''\psi_{\eta\eta}\right), \tag{2.3.2a}$$

$$-\psi_\eta\psi_{\xi\xi}+\psi_\xi\psi_{\xi\eta}+h''\psi_\eta^2+h'\left(\psi_\eta\psi_{\xi\eta}-\psi_\xi\psi_{\eta\eta}\right)=-p_\eta-\varepsilon^{\left(\frac{1}{\alpha}-1\right)}\left(\psi_{\xi\eta\eta}-h'\psi_{\eta\eta\eta}\right)-\varepsilon^{\left(\frac{1}{\alpha}+1\right)}\left(\frac{\partial}{\partial\xi}-h'\frac{\partial}{\partial\eta}\right)^3\psi. \tag{2.3.2b}$$

From equations (2.2.9) the boundary conditions on the free surface i.e. at $\eta=0$ become,

$$\psi=0, \tag{2.3.3a}$$

$$\varepsilon\left(h'p+\psi_{\eta\eta}\right)-\varepsilon^{\left(\frac{1}{\alpha}-1\right)}\left[2h'\left(\psi_{\xi\eta}-h'\psi_{\eta\eta}\right)+\left(\frac{\partial}{\partial\xi}-h'\frac{\partial}{\partial\eta}\right)^2\psi\right]=0, \tag{2.3.3b}$$

$$p+\varepsilon^{\left(\frac{1}{\alpha}-1\right)}\left(2\psi_{\xi\eta}-h'\psi_{\eta\eta}\right)-\varepsilon^{\left(\frac{1}{\alpha}+1\right)}h'\left(\frac{\partial}{\partial\xi}-h'\frac{\partial}{\partial\eta}\right)^2\psi=0. \tag{2.3.3c}$$

The aim is to find a solution of the equations of (2.1.4) in the form of an boundary layer expansion in ε. In order to match this to the core Couette- Poisueille flow, it is necessary to have $\psi\sim\varepsilon^2\eta^2\sim y^2$ as $\eta\to\infty$ in the inner region, to lowest order in ε. Therefore, ψ must be of order ε^2. In order to determine the value of α, the convective and viscous terms must balance. This is achieved upon taking the value of $\alpha=1/3$ similar to the case of Newtonian jet (Tillett 1968; Miyake 1979; Philippe & Dumargue 1991) as well to the non- Newtonian jet (Khayat 2014). The streamwise and transverse velocity components are now expressed in terms of the stream function as $u=\psi_z=\frac{1}{\varepsilon}\psi_\eta$ and $w=-\psi_x=-\psi_\xi+h'\psi_\eta$, respectively. Considering the fact that the streamwise velocity u in the inner region must match the velocity $u\to(1-G)z+Gz^2$ in the core region, it is

concluded that u is of order ε. The order of the transverse velocity can be found by writing the continuity equation in terms of the inner variables,

$$\varepsilon u_\xi - \varepsilon h' u_\eta + w_\eta = 0. \tag{2.3.4}$$

Clearly, w is of order ε^2. Consequently, the momentum conservations equations (2.3.2) reduce to,

$$\begin{aligned}\psi_\eta\psi_{\xi\eta} - \psi_\xi\psi_{\eta\eta} = &-\varepsilon^2\left(p_\xi - h' p_\eta\right)\\ &+\varepsilon^2\psi_{\eta\eta\eta} + \varepsilon^4\left(\psi_{\xi\xi\eta} - 2h'\psi_{\xi\eta\eta} + h'^2\psi_{\eta\eta\eta} - h''\psi_{\eta\eta}\right),\end{aligned} \tag{2.3.5a}$$

$$\begin{aligned}&-\psi_\eta\psi_{\xi\xi} + \psi_\xi\psi_{\xi\eta} + h''\psi_\eta^2 + h'\left(\psi_\eta\psi_{\xi\eta} - \psi_\xi\psi_{\eta\eta}\right)\\ &\qquad = -p_\eta - \varepsilon^2\left(\psi_{\xi\eta\eta} - h'\psi_{\eta\eta\eta}\right) - \varepsilon^4\left(\frac{\partial}{\partial\xi} - h'\frac{\partial}{\partial\eta}\right)^3\psi.\end{aligned} \tag{2.3.5b}$$

Similarly, the boundary conditions on the free surface i.e. at $\eta = 0$ can be rewritten as,

$$\psi = 0, \tag{2.3.6a}$$

$$\varepsilon\left(h' p + \psi_{\eta\eta}\right) - \varepsilon^3\left[2h'\left(\psi_{\xi\eta} - h'\psi_{\eta\eta}\right) + \left(\frac{\partial}{\partial\xi} - h'\frac{\partial}{\partial\eta}\right)^2\psi\right] = 0, \tag{2.3.6b}$$

$$p + \varepsilon^2\left(2\psi_{\xi\eta} - h'\psi_{\eta\eta}\right) - \varepsilon^4 h'\left(\frac{\partial}{\partial\xi} - h'\frac{\partial}{\partial\eta}\right)^2\psi = 0. \tag{2.3.6c}$$

The inner expansion for ψ begins with a term in ε^2. This assumption holds until contrary evidence is found. Therefore, the expansion precedes in powers of ε so that,

$$\psi(\xi,\eta) = \varepsilon^2\Psi_2(\xi,\eta) + \varepsilon^3\Psi_3(\xi,\eta) + \cdots. \tag{2.3.7}$$

Similarly, h is expanded as,

$$h(\xi)=\varepsilon^{-1}\zeta(\xi)=h_0(\xi)+\varepsilon h_1(\xi)+\cdots. \tag{2.3.8}$$

From (2.3.5)-(2.3.7), it is concluded that pressure p in the inner layer is of order ε^4. Hence,

$$p(\xi,\eta)=\varepsilon^4 P_4(\xi,\eta)+\varepsilon^5 P_5(\xi,\eta)+\cdots. \tag{2.3.9}$$

Recalling that $u=\frac{1}{\varepsilon}\psi_\eta$ and $w=-\psi_\xi+h'\psi_\eta$, then the velocity components take the following form,

$$u(\xi,\eta)=\varepsilon U_1(\xi,\eta)+\varepsilon^2 U_2(\xi,\eta)+\cdots, \tag{2.3.10}$$

$$w(\xi,\eta)=\varepsilon^2 W_2(\xi,\eta)+\varepsilon^3 W_3(\xi,\eta)+\cdots \tag{2.3.11}$$

In this case, $U_1=\Psi_{2\eta}$, $U_2=\Psi_{3\eta}$ and $W_2=-\Psi_{2\xi}+h_0'\Psi_{2\eta}$, and so on.

2.3.1 Flow in the inner layer to $O(\varepsilon^2)$

To leading order in ε, equation (2.3.5a), reduce to,

$$\Psi_{2\eta}\Psi_{2\xi\eta}-\Psi_{2\xi}\Psi_{2\eta\eta}=\Psi_{2\eta\eta\eta}. \tag{2.3.1.1}$$

The above problem is similar to the case of symmetric free jet (Tillett 1968) with different boundary conditions. The corresponding boundary conditions are obtained from (2.3.6), namely

$$\Psi_2(\xi,0)=\Psi_{2\eta\eta}(\xi,0)=0. \tag{2.3.1.2a}$$

To complete the problem for Ψ_2, another boundary condition is required. This is the matching condition, which will be obtained later, namely,

$$\Psi_2(\xi,\eta)\sim(1-G)\frac{\eta^2}{2}\ \text{as}\ \eta\to\infty. \tag{2.3.1.2b}$$

Following Tillett (1968) a similarity solution can be carried out for Ψ_2, which is written here as,

$$\Psi_2(\xi,\eta) = \xi^{2/3} f_2(\theta), \tag{2.3.1.3}$$

where $\theta = \eta\xi^{1/3}$ is the similarity variable. The equation for $f_2(\theta)$ is given by,

$$3f_2''' + 2f_2 f_2'' - f_2'^2 = 0. \tag{2.3.1.4}$$

Subject to the following boundary conditions:

$$f_2(0) = f_2''(0) = 0, \tag{2.3.1.5a}$$

$$f_2(\theta) \sim (1-G)\frac{\theta^2}{2} \text{ as } \theta \to \infty. \tag{2.3.1.5b}$$

Condition (2.3.1.5b) is achieved from matching, which will be discussed in section 2.8. For large θ, it is possible to obtain an asymptotic solution, subject to condition (2.3.1.5b), to read,

$$f_2(\theta \to \infty) \sim (1-G)\frac{(\theta + c_1)^2}{2}, \tag{2.3.1.6}$$

where c_1 is a G dependent constant determined from the numerical integration.

A common form of the problems (2.3.1.4)-(2.3.15) can easily be derived for all the values of G and is given by,

$$3g_2''' + 2g_2 g_2'' - g_2'^2 = 0. \tag{2.3.1.7}$$

Subject to the following boundary conditions:

$$g_2(0) = g_2''(0) = 0, \tag{2.3.1.8a}$$

$$g_2(\theta) \sim \frac{t^2}{2} \text{ as } t \to \infty, \tag{2.3.1.8b}$$

where $f_2 = b_2 g_2$ and $t = \frac{\theta}{a}$. Both a and b_2 are constants. Similarly, for large θ, the asymptotic solution becomes,

$$g_2(t \to \infty) \sim \frac{(t + d_1)^2}{2}. \tag{2.3.1.9}$$

The problem (2.3.1.7)-(2.3.1.8) is solved as an initial-value problem, where equation (2.3.1.7) is integrated subject to the conditions (2.3.1.8a) and a guessed value of the slope at the origin. The slope g_2' is adjusted until a reasonable matching is achieved between the solution and its asymptotic form (2.3.1.8b) at large t, or, more precisely, between g_2'' and 1. The integration is carried out over the domain $[0, t_\infty]$, where t_∞ corresponds to a relatively large value of t. A value of $t_\infty = 6$ is turned out to be sufficiently large to secure the matching within an imposed tolerance. Matching the numerical solution with its asymptotic counterpart (2.3.1.9) gives the value of d_1. From the figure 2.4, it is convenient to observe that the initial slope is approximately $g_2'(0) = 1.61090$ and the value of d_1 is approximately equal to 0.8920. The value of the similarity function f_2, its derivative and the constant c_1 for each G are determined from the following relations:

$$f_2(\theta) = (1-G)^{1/3} g_2(t), \qquad f_2'(\theta) = (1-G)^{2/3} g_2'(t). \tag{2.3.1.10}$$

So, the slope at the origin becomes,

$$f_2'(0) = (1-G)^{2/3} g_2'(0). \tag{2.3.1.11}$$

And the constant,

$$c_1 = (1-G)^{-1/3} d_1. \tag{2.3.1.12}$$

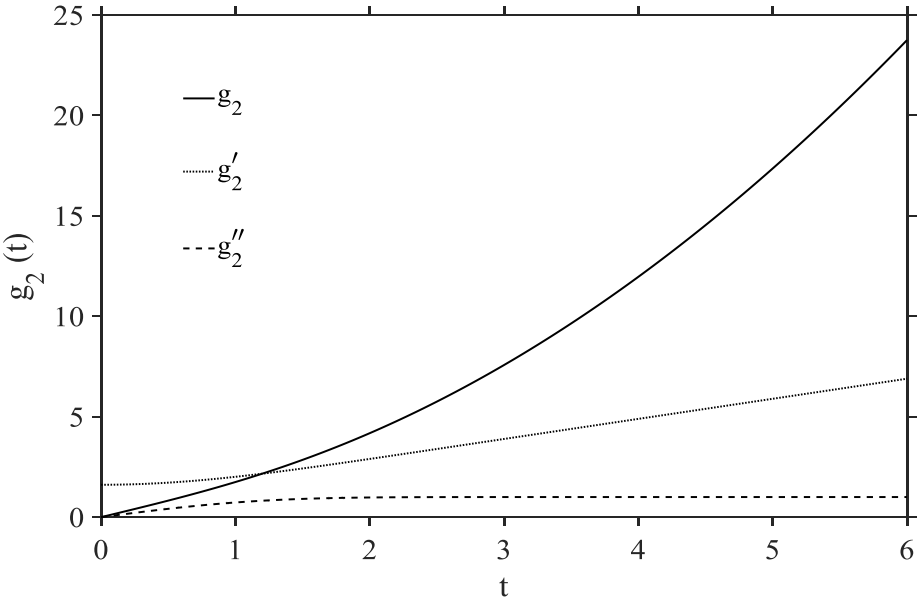

Figure 2.4: Variation of the function g_2, g_2' and g_2'' with t for all the G values.

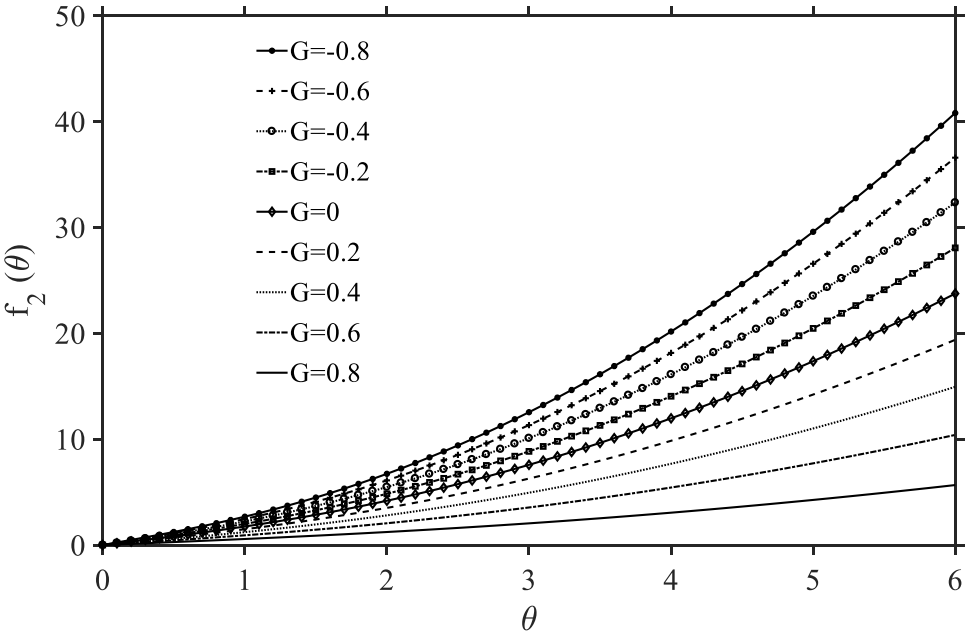

Figure 2.5: Variation of similarity function f_2 with θ for all the G values.

Figure 2.4 displays the dependence of g_2 on t for all the G values. The figure does not reflect clearly the flow behavior with respect to the parameter G. All it says that the function g_2 and its slope increase monotonically with t for the every G value. The effect of G on the similarity function f_2 can easily be seen in the figure 2.5. From the figure, it is obvious that f_2 increases essentially linearly with G, pointing to a strengthening of the flow with the pressure gradient, which is also reflected by the increase in the slope f_2'. However, different scenarios are observed for the positive and negative G values. In particular, as the value of G increases positively, the flow is actually weakening which is understandable since G positive means that the pressure gradient is acting adversely. Therefore, increasing the magnitude of the adverse pressure gradient will reduce the effect of the wall velocity, which will eventually lead to a weaker flow. This behavior is more evident in the figure 2.6 where the initial slope $f_2'(0)$ and the constant c_1 are plotted against the parameter G. Of particular interest, the value of the initial slope $f_2'(0)$, which is directly related to the streamwise velocity component u on the free surface.

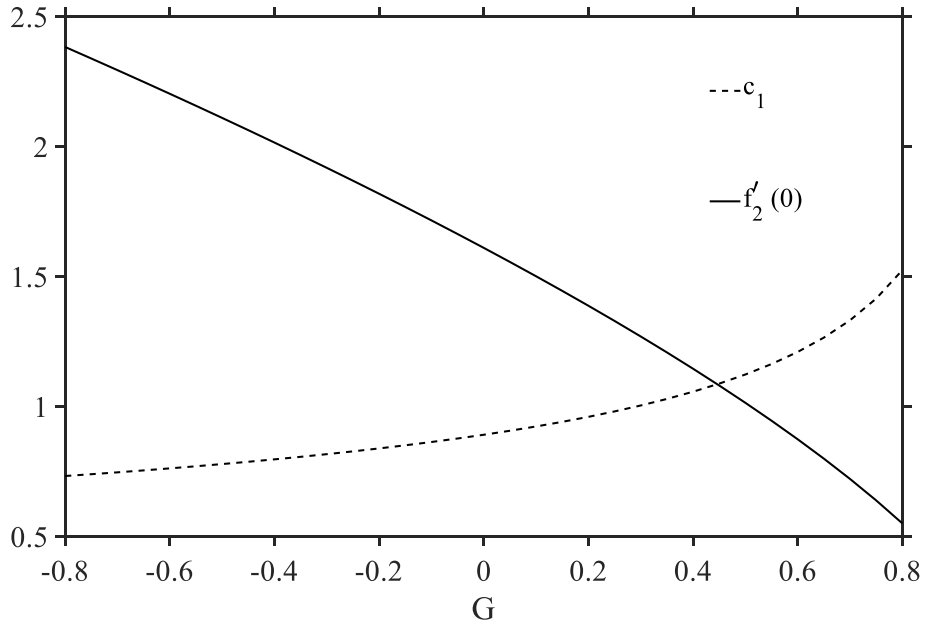

Figure 2.6: Dependence of the initial slope $f_2'(0)$ and c_1 on the parameter G.

The figure suggests that the velocity is decreasing with the positive increasing values of G, which confirms the weakening of the flow with the adverse pressure gradient indeed (see figure 2.10a). For the negative G values, initial slope $f_2'(0)$ shows an opposite trend, which indicates the increase in the velocity u (see figure 2.10b). This, in turn, reflects the strengthening of the flow with the favorable pressure gradient. Interestingly, for the positive G values, c_1 shows a contrasting behavior of the initial slope. This has a significant consequence on the influence of adverse pressure gradient on the film height. The film height increases with the increasing values of positive G as opposed to the velocity at the free surface, which is shown in the figure 2.12a. However, this is not the case for the negative G cases where the reduction of the film height with G is observed (see figure 2.12b).

2.3.2 Flow in the inner layer to $O(\varepsilon^3)$

To next order in ε (2.3.5a) becomes,

$$\Psi_{2\eta}\Psi_{3\xi\eta} + \Psi_{3\eta}\Psi_{2\xi\eta} - \Psi_{2\xi}\Psi_{3\eta\eta} - \Psi_{3\xi}\Psi_{2\eta\eta} = \Psi_{3\eta\eta\eta}. \tag{2.3.2.1}$$

The boundary conditions are,

$$\Psi_3(\xi,0) = \Psi_{3\eta\eta}(\xi,0) = 0. \tag{2.3.2.2a}$$

Matching provides the third boundary condition, which is,

$$\Psi_3(\xi,\eta) \sim 2\eta^3 \text{ as } \eta \to \infty. \tag{2.3.2.2b}$$

Similar to before, Ψ_3 also admits a similarity solution of the form (Tillett 1968),

$$\Psi_3(\xi,\eta) = \xi f_3(\theta), \tag{2.3.2.3}$$

where $\theta = \eta\xi^{1/3}$ is the similarity variable. The equation for $f_3(\theta)$ is given by,

$$3f_2'f_3' - 2f_2f_3'' - 3f_2''f_3 = -3f_3'''. \tag{2.3.2.4}$$

Subject to the following boundary conditions:

$$f_3(0) = f_3''(0) = 0, \tag{2.3.2.5a}$$

$$f_3(\theta) \sim G\frac{\theta^3}{3} \text{ as } \theta \to \infty. \tag{2.3.2.5b}$$

For large θ, an asymptotic solution similar to the free surface jet (Tillett 1968; Saffari & Khayat 2008; Khayat 2014) is possible to obtain, namely,

$$f_3(\theta \to \infty) \sim \frac{G}{3}\left[(\theta + c_1)^3 - \frac{6}{1-G}\right] + c_2(\theta + c_1). \tag{2.3.2.6}$$

Similarly, the common form of problem (2.3.2.4)-(2.3.2.5) for all the values of G is given by,

$$3g_3''' + 2g_2g_3'' - 3g_2g_3' + 3g_2''g_3 = 0. \tag{2.3.2.7}$$

Subject to the following boundary conditions:

$$g_3(0) = g_3''(0) = 0, \tag{2.3.2.8a}$$

$$g_3(\theta) \sim \frac{t^3}{3} \text{ as } t \to \infty. \tag{2.3.2.8b}$$

where $f_3 = b_3 g_3$ and $t = \frac{\theta}{a}$. Both a and b_3 are constants. Condition (2.3.2.8b) is obtained from matching, which will be discussed in section 2.8. The asymptotic solution reads,

$$g_3(t \to \infty) \sim \frac{1}{3}\left[(t + d_1)^3 - 6\right] + d_2(t + d_1). \tag{2.3.2.9}$$

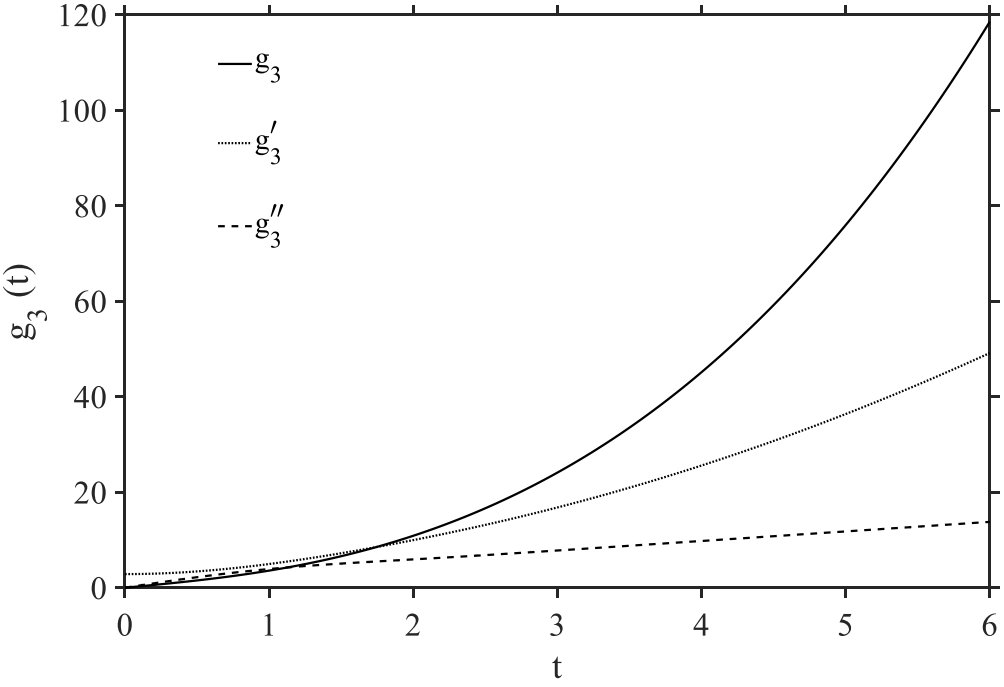

Figure 2.7: Variation of the function g_3, g_3' and g_3'' with t for all the G values.

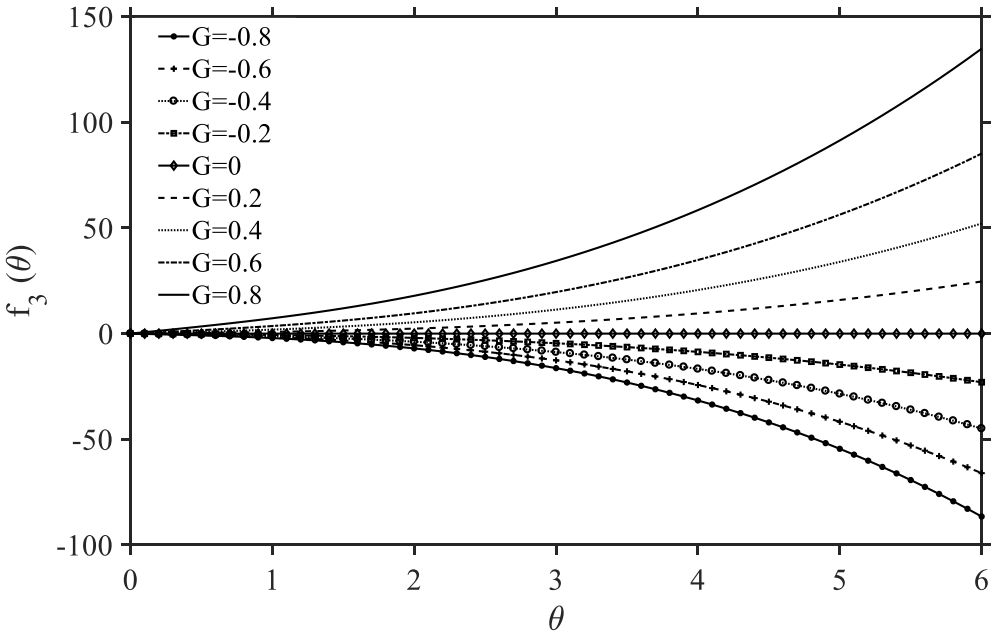

Figure 2.8: Variation of similarity function f_2 with θ for all the G values.

The value of constant $d_2(1.65404)$ is determined from the numerical integration of equation (2.3.2.7). Although the solution procedure is similar to before, the problems (2.3.1.7)-(2.3.1.8) and (2.3.2.7)-(2.3.2.8) are solved as a coupled system. Figure 2.7 depicts the profiles of function g_3 with t. Here also, the effect of G on the flow is not evident and the true picture is displayed in the figure 2.8. For the positive values of G, both f_3 and f_3' are always turn out to be positive, indicating to a higher order strengthening effect of pressure gradient on the flow close to the free surface whereas a higher order weakening effect is visible for the negative G values due to the negative values of both f_3 and f_3'. This can also be seen upon taking the velocity u to the third order by using the expressions (2.3.10), (2.3.1.3) and (2.3.2.3) respectively,

$$u(x,\theta) = \varepsilon x^{1/3} f_2'(\theta) + \varepsilon^2 x^{2/3} f_3'(\theta). \tag{2.3.2.10}$$

At the free surface $(z = \zeta)$, the velocity becomes,

$$u(x, z = \zeta) = \varepsilon x^{1/3} f_2'(0) + \varepsilon^2 x^{2/3} f_3'(0). \tag{2.3.2.11}$$

It is to be noted that for pure Couette flow ($G = 0$) case, to capture the higher order effect, one needs to proceed to the next order i.e. to order ε^4. The following expressions are used to determine the value of the similarity function f_3, its derivative and the constant c_2:

$$f_3(\theta) = G(1-G)^{-1} g_3(t), \qquad f_3'(\theta) = G(1-G)^{-2/3} g_3'(t). \tag{2.3.2.12}$$

Now, the slope at the origin becomes, namely,

$$f_3'(0) = G(1-G)^{-2/3} g_3'(0). \tag{2.3.2.13}$$

And the constant,

$$c_2 = G(1-G)^{-2/3} d_2 \tag{2.3.2.14}$$

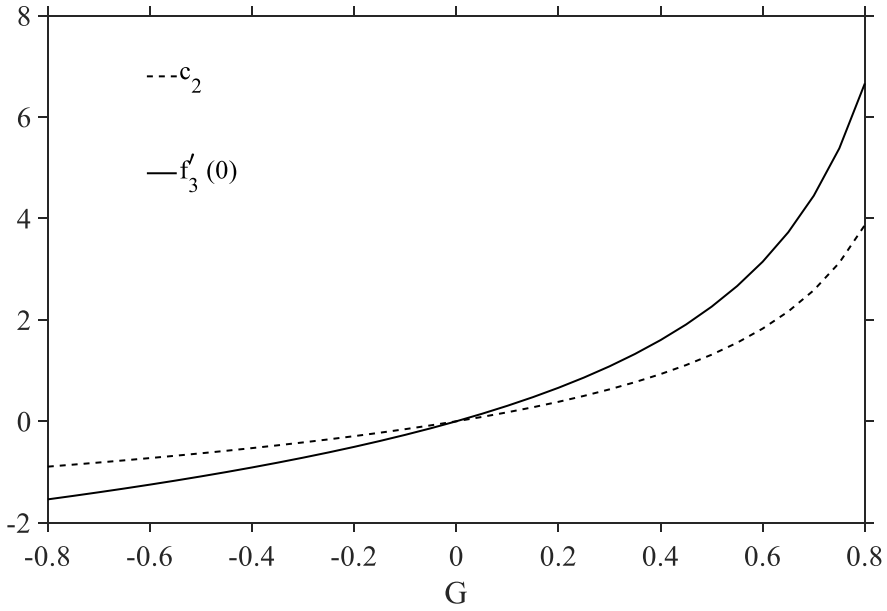

Figure 2.9: Dependence of the initial slope $f_3'(0)$ and c_2 on the parameter G.

Figure 2.9 illustrates the dependence of the initial slope $f_3'(0)$ and c_2 on G. Surprisingly, both the initial slope $f_3'(0)$ and c_2 follow an increasing trend with the positive G values, indicating higher order strengthening effect of the adverse pressure gradient on the flow near the free surface. In contrast, a decreasing trend is observed for the negative values of G, pointing to a higher order weakening effect of the favorable pressure on the flow close to the free surface. Now, along with the slopes in figures 2.6 and 2.9, the expression (2.3.2.11) provides the dependence of the free surface velocity u on the pressure gradient, which is depicted in the figure 2.10 for all the G values. From the figure, it is clear that the free surface velocity u diminishes in the case of favorable pressure gradient and grows for the adverse pressure gradient upon adding the higher order term. Figure 2.11 displays the effect of inertia on the free surface velocity u. Expression (2.3.2.11) and the figure both suggest that $u(x, z=\zeta)$ increases monotonically with x. In the figure 2.11a, apparent decrease in the surface velocity is observed due to the scaling used in the current formulation. The true picture is reflected in the figure 2.11b where the Reynolds number multiplies the streamwise velocity. The depthwise velocity w and the free surface height

will become available once the free surface height is determined from matching in the section 2.8. However, at this stage, it is helpful to discuss the influence of pressure gradient and inertia on both of them. The free surface height is given by (refer to section 2.8 for details),

$$\zeta(x) = \varepsilon c_1 x^{1/3} + \varepsilon^2 \frac{c_2}{(1-G)} x^{2/3}. \tag{2.3.2.15}$$

By recalling the equations (2.3.11), (2.31.3) and (2.3.2.3), to third order, the transvers velocity component is obtained, to read,

$$\begin{aligned} w(x,\theta) = -\varepsilon^2 &\left[\frac{x^{-1/3}}{3}(2f_2 - \theta f_2') - x^{1/3} h_0' f_2' \right] \\ -\varepsilon^3 &\left[f_3 - \frac{\theta}{3} f_3' - x^{2/3} f_3' h_0' - x^{1/3} h_1' f_2' \right]. \end{aligned} \tag{2.3.2.16}$$

At the free surface, (2.3.2.16) reduces to,

$$w(x, z=\zeta) = \frac{\varepsilon^2}{3} \xi^{-1/3} c_1 f_2'(0) + \frac{\varepsilon^3}{3}\left[c_1 f_3'(0) + \frac{2c_2}{1-G} f_2'(0) \right]. \tag{2.3.2.17}$$

The jet surface profiles for different levels of pressure gradient are shown in the figure 2.12, reflecting a monotonic increase with distance x. The film gets thicker with the increment in the level of favorable pressure gradient whereas it becomes thinner with the adverse pressure gradient. The figure also suggests that the jet always contracts near the exit regardless of the direction of the pressure gradient. Figure 2.13 displays the inertia influence on the jet surface. The effect of inertia is similar to the favorable pressure gradient, which tends to increase the jet thickness as its value becomes higher. The transverse velocity w profiles are plotted against the distance for the different G values in the figure 2.14. It is clear from the figure that the depth wise velocity gradually diminishes with x after the jump at the channel exit for any G values. This means that elongation is only dominant in a region very close to the channel exit. The figure also indicates that there is a significant departure in the transverse velocity for the positive G values.

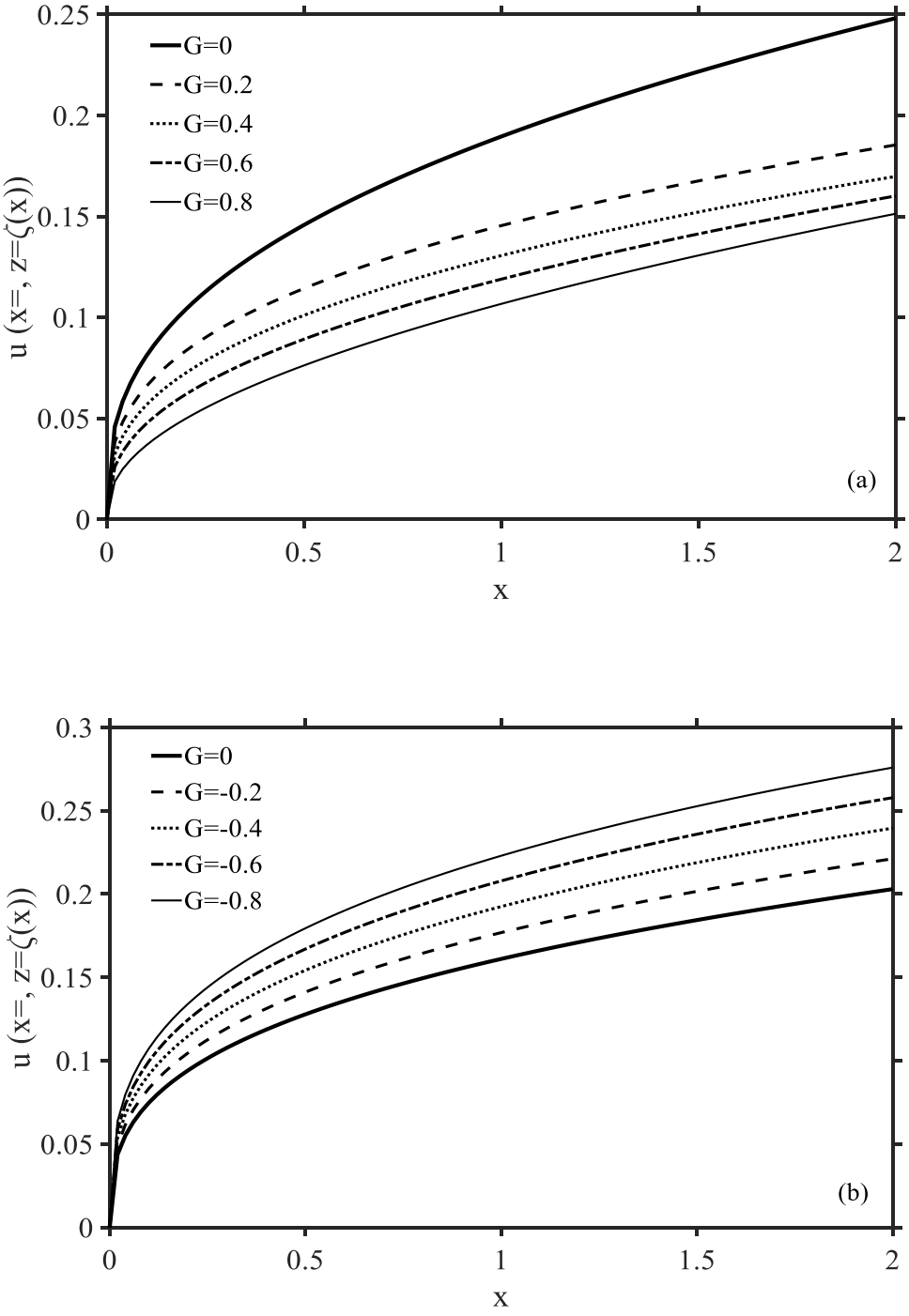

Figure 2.10: Influence of pressure gradient (a) adverse $\left(G \in [0, 0.8]\right)$ and (b) favorable $\left(G \in [0, -0.8]\right)$ on the streamwise velocity u at the free surface $z = \zeta(x)$ for $\varepsilon = 0.1$.

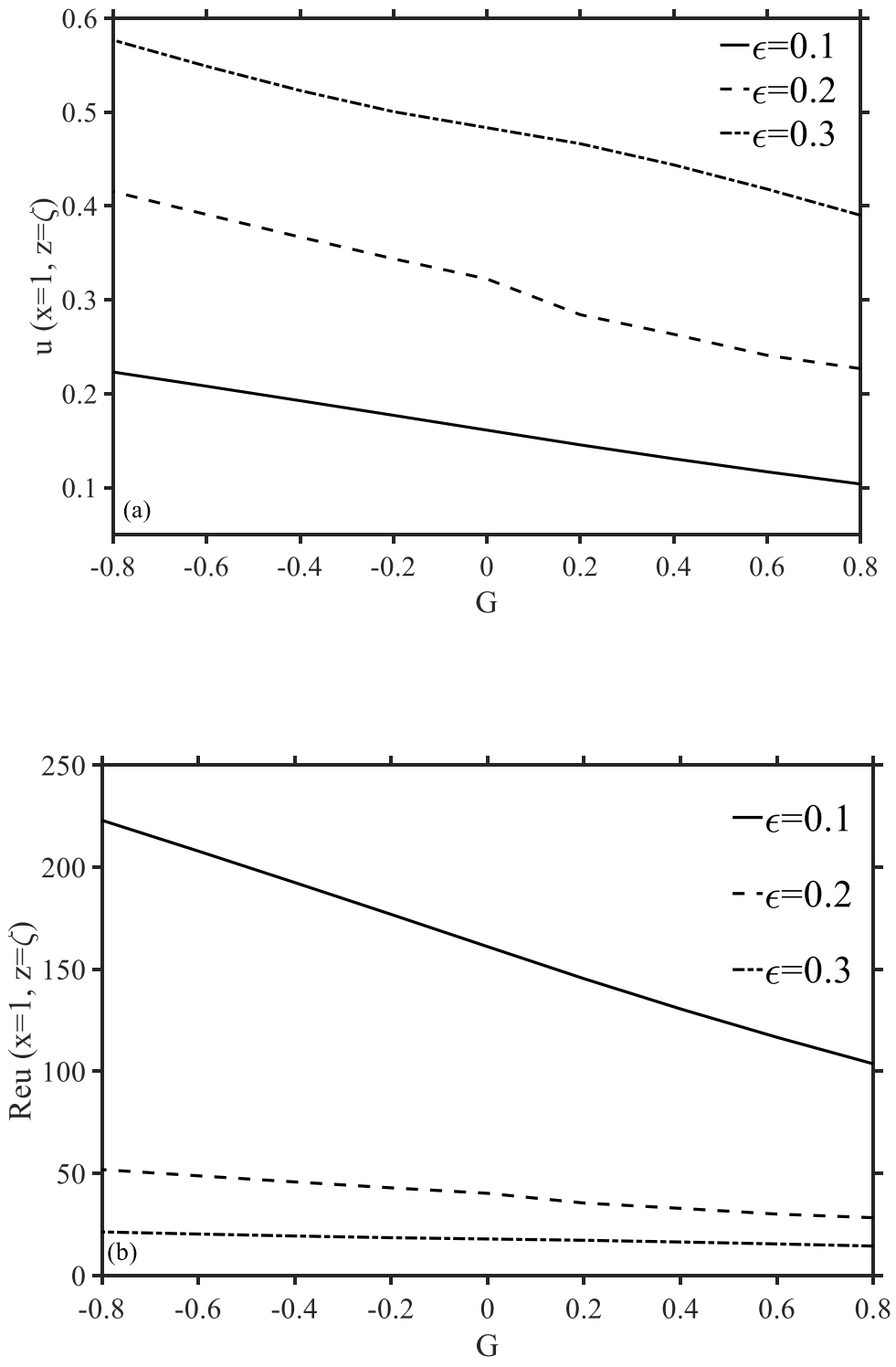

Figure 2.11: Influence of inertia on the streamwise velocity $u(x=1, z=\zeta)$ at the free surface $z=\zeta(x)$ (a) for different ε and (b) $\mathrm{Re}\, u(x=1, z=\zeta)$.

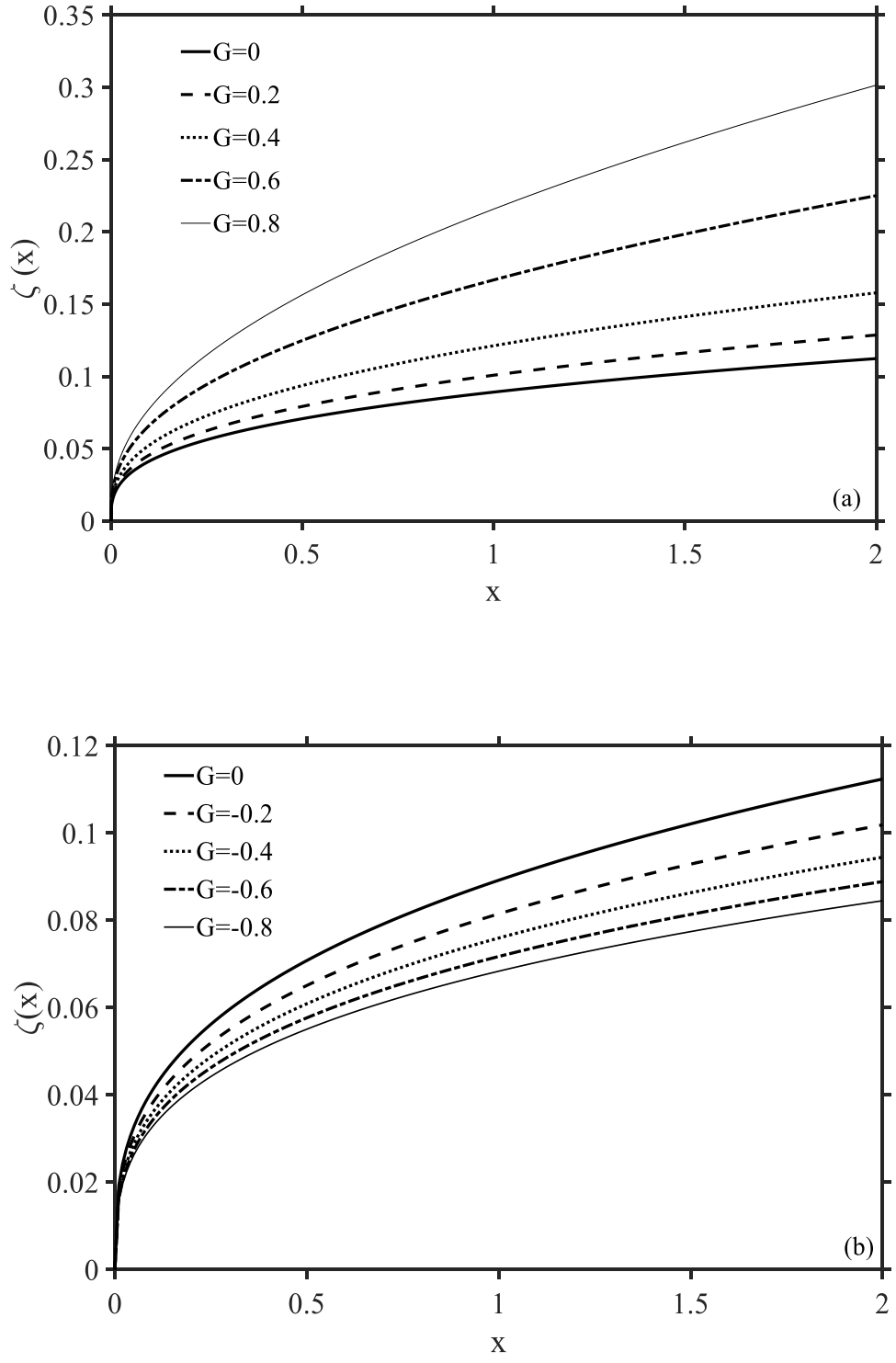

Figure 2.12: Influence of pressure gradient (a) adverse $\left(G \in [0, 0.8]\right)$ and (b) favorable $\left(G \in [0, -0.8]\right)$ on free surface $z = \zeta(x)$ for $\varepsilon = 0.1$.

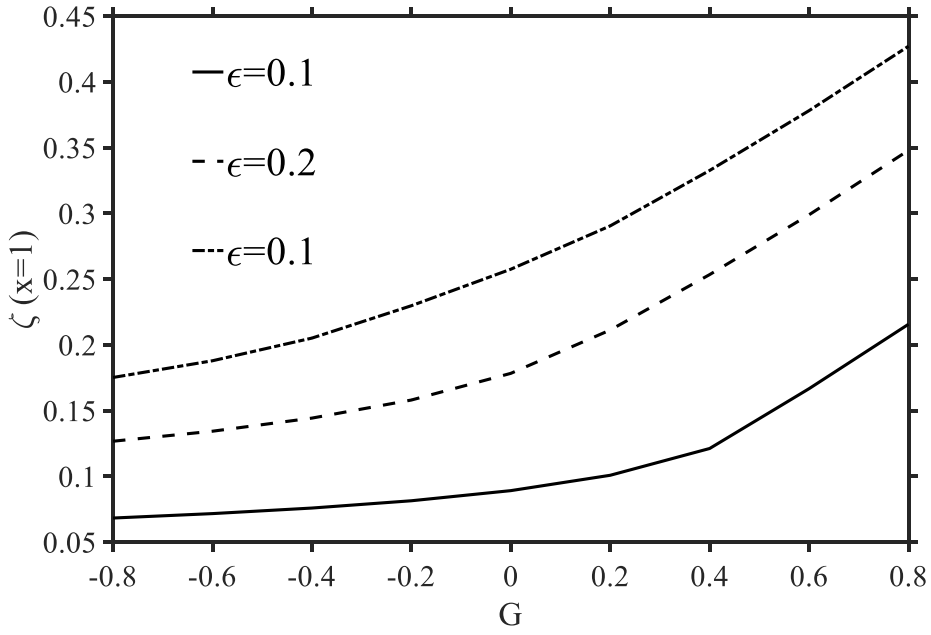

Figure 2.13: Influence of inertia on the jet surface $\zeta(\mathrm{x}=1)$.

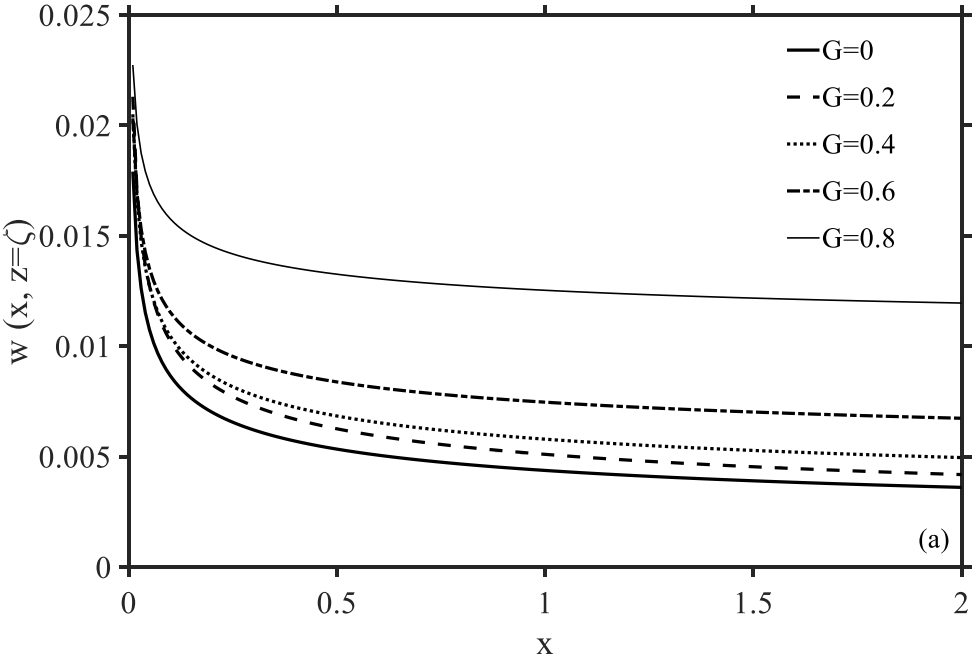

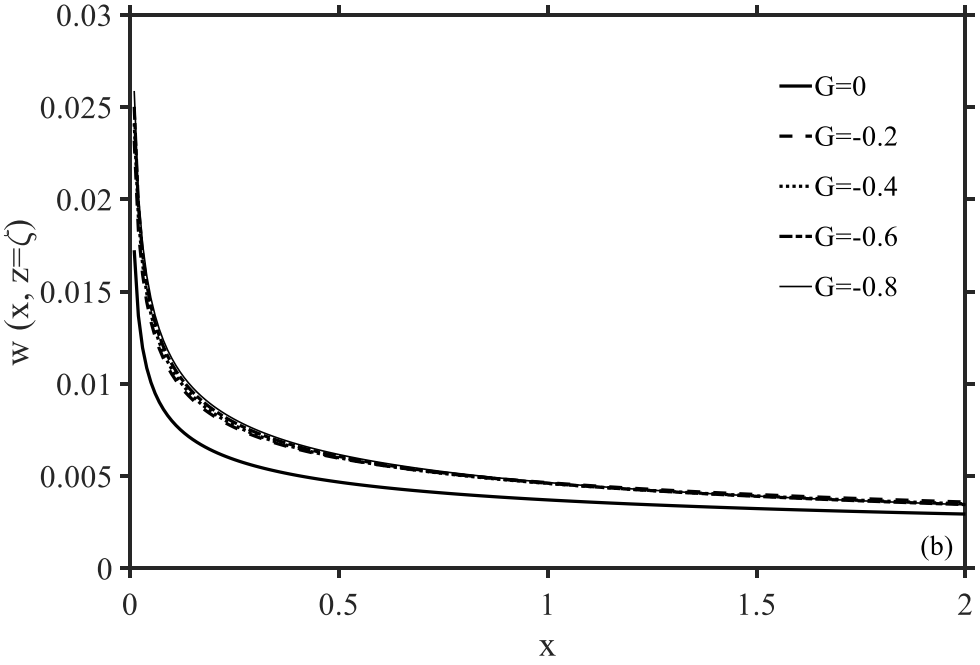

Figure 2.14: Influence of pressure gradient (a) adverse $\left(G \in [0, 0.8]\right)$ and (b) favorable $\left(G \in [0, -0.8]\right)$ on the transverse velocity, $w\left(x, z = \zeta\right)$ at the free surface, $z = \zeta\left(x\right)$ for $\varepsilon = 0.1$.

Figure 2.15 displays the surface curvature variation with the inclination angle for $\varepsilon = 0.2$ and $G \in [0, 0.8]$. From the figure, it is visible that the curvature decreases with the increasing adverse pressure gradient. This agrees with the fact that the more positive the value of G becomes the more contraction of the free surface occurs. The results in the figure 2.15 are overall qualitatively similar to the numerical results of Saito & Scriven (1981) and Lee et al. (2002) (refer to figure 23a of Lee et al. 2002) for the slot coating flow. However, in the present case, the surface curvature shows a change in the concavity at low inclination angle as opposed to the linear growth predicted for the slot coating flow in the previous studies. This might happen due to the high inertia effect considered in the current analysis. The effect of inertia on the surface curvature are shown in the figure 2.16 for G=0.4. Inertia affects the surface curvature in a contrasting manner to the pressure gradient by increasing the value of curvature.

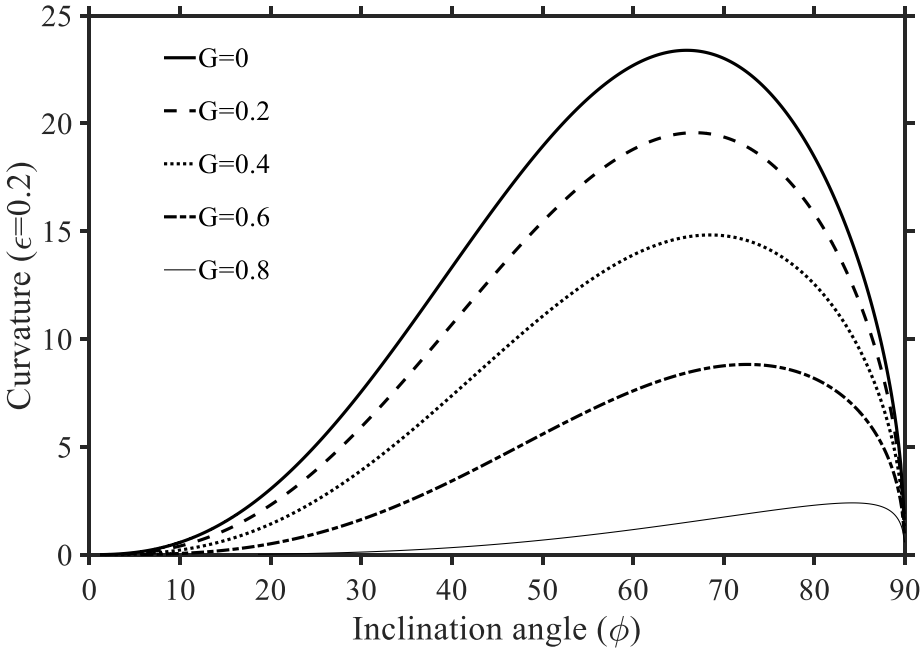

Figure 2.16: Free surface curvature variation with the inclination angle for $G \in [0, 0.8]$ and $\varepsilon = 0.2$

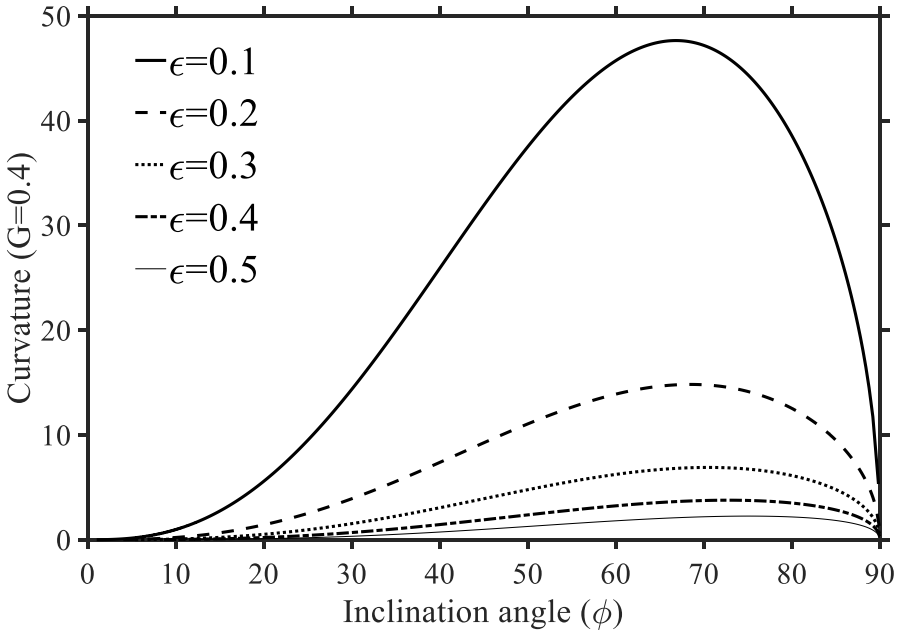

Figure 2.15: Effect of inertia on the free surface curvature with the inclination angle for G=0.4

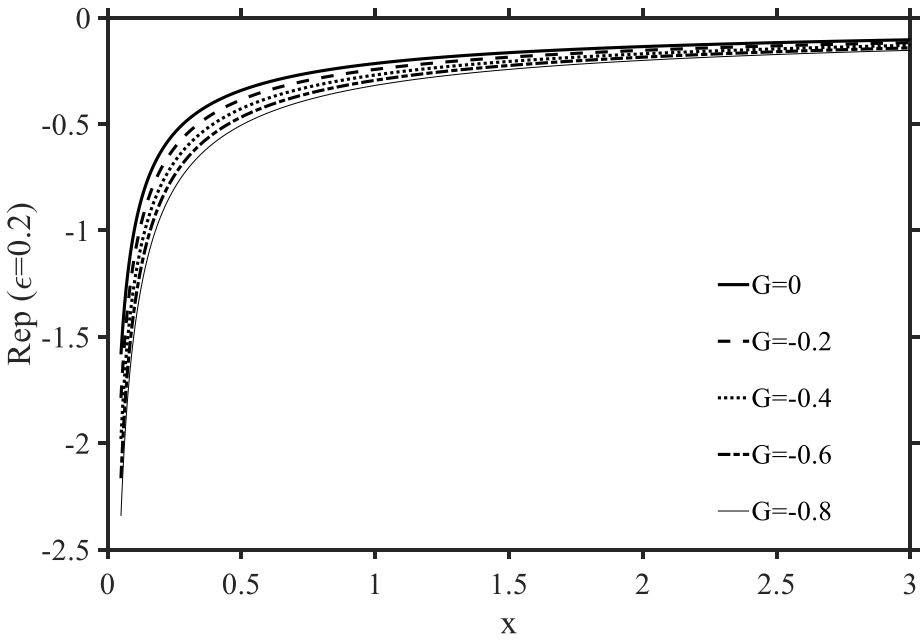

Figure 2.17: Development of the pressure along the free surface with distance x for $\varepsilon = 0.2$ and for $G \in [0, -0.8]$.

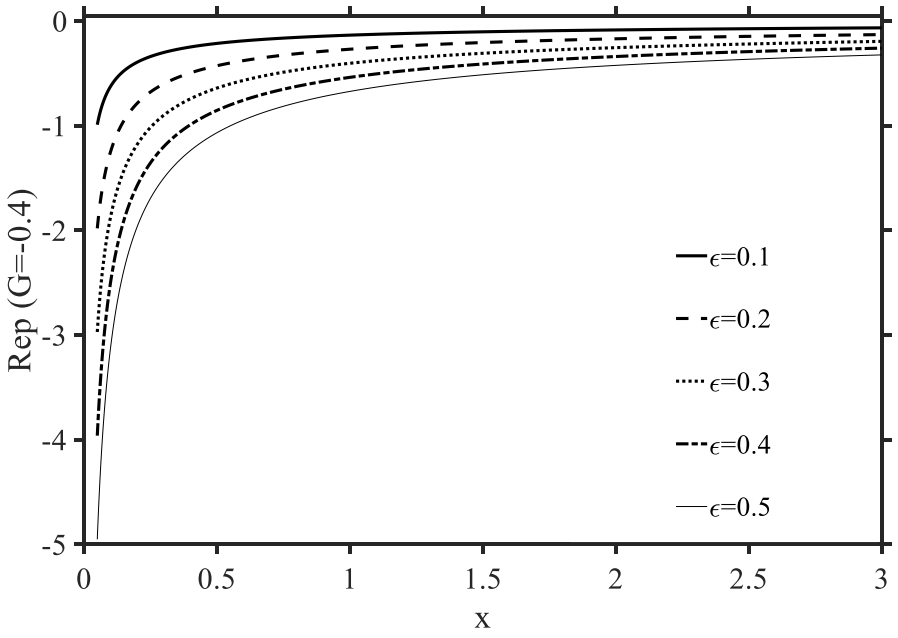

Figure 2.18: Effect of inertia on the pressure along the free surface for G=-0.4.

Figures 2.17 and 2.18 display the effects of pressure gradient and inertia on the pressure along the free surface, respectively. A sharp variation of the pressure occurs very close to the exit in both cases due to the singularity effect (figure 2.17). In addition, the pressure reaches to zero level rapidly for higher inertia than the lower inertia (see figure 18).

The effect of inertia on the film thickness at a specific x location (x=1) for different levels of the pressure gradient is depicted in the figure 2.19. The figure shows that the film thickness increases with the Reynolds number, and an asymptotic behavior of the film thickness at higher Reynolds number is also reflected in the figure 2.19. Surprisingly, this behavior is independent of the direction and magnitude of the pressure gradient. Usually, the high Reynolds number flows exhibit this behavior since the viscous effect becomes negligible when $\mathrm{Re} \to \infty$. Eventually, the flow will act as an inviscid flow with the film thickness becomes equal to the channel gap. Moreover, as the magnitude of adverse pressure gradient increases, the film thickness gets thinner, and an opposite trend is observed for the favorable case.

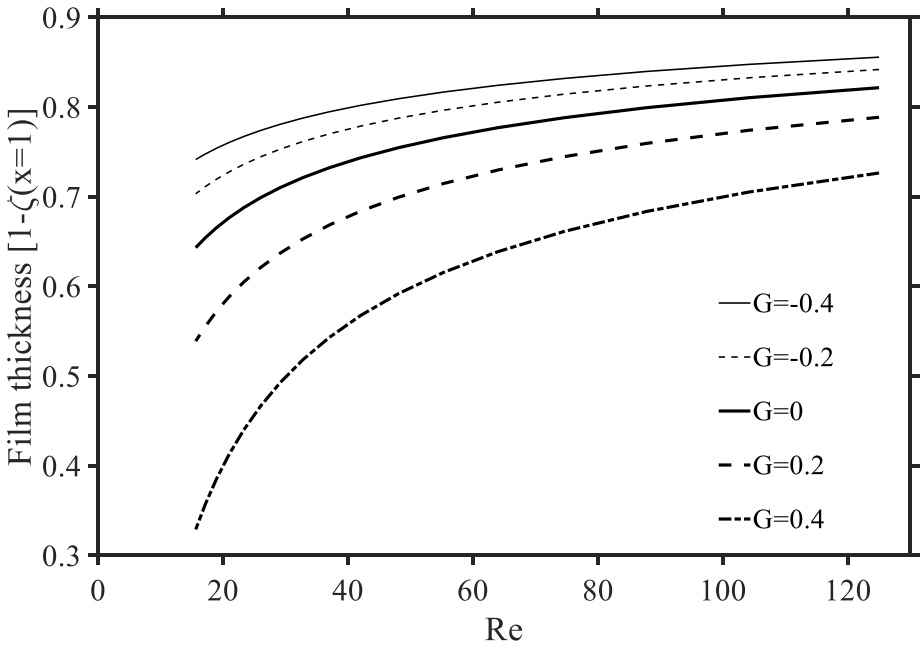

Figure 2.19: Development of the film thickness with Re for different level of pressure gradient ($G \in [-0.4, 0.4]$).

2.4 Flow in the lower wall layer

The flow structure in the boundary layer near the lower wall is examined separately in this section. In this layer, similar to the free-surface layer, the transverse coordinate near the boundary will be denoted by $y = \varepsilon\eta$, where ε is the same small parameter used before. To examine the lower-wall layer i.e. the structure of the boundary layer close to the lower wall upstream of the channel exit, the near-wall coordinates are changed as $x = \xi$ and $y = z = \varepsilon\eta$. Similar to the inner layer, matching with the core flow upstream of the channel exit shows that $\psi \sim (1-G)\frac{y^2}{2} = (1-G)\frac{\varepsilon^2\eta^2}{2}$ as $\eta \to \infty$. Therefore, ψ must have the order of ε^2 close to the lower wall. In this case, the non-dimensional momentum conservation equations (2.1.4), along with the no-slip, no penetration (2.210a and 2.2.10b) and upstream (2.2.10c) conditions are,

$$\psi_\eta\psi_{\xi\eta} - \psi_\xi\psi_{\eta\eta} = -\varepsilon^2 p_\xi + \varepsilon^2\psi_{\eta\eta\eta} + \varepsilon^4\psi_{\xi\xi\eta}, \tag{2.4.1a}$$

$$\psi_\eta\psi_{\xi\xi} - \psi_\xi\psi_{\xi\eta} = p_\eta + \varepsilon^2\psi_{\xi\eta\eta} + \varepsilon^4\psi_{\xi\xi\xi}, \tag{2.4.1b}$$

$$\psi(\xi, \eta = 0) = \psi_\eta(\xi, \eta = 0) = 0, \tag{2.4.1c}$$

$$\psi(\xi \to -\infty, \eta) \sim (1-G)\frac{\varepsilon^2\eta^2}{2} + G\frac{\varepsilon^3\eta^3}{3}. \tag{2.4.1d}$$

The streamwise and transverse velocity components become,

$$u = \frac{1}{\varepsilon}\psi_\eta, \tag{2.4.2}$$

$$w = -\psi_\xi. \tag{2.4.3}$$

Noting from the expressions (2.4.1) that p is of order ε^2, the flow field expansion reads,

$$\psi(\xi, \eta) = \varepsilon^2\Psi_2(\xi, \eta) + \varepsilon^3\Psi_3(\xi, \eta) + \cdots, \tag{2.4.4}$$

$$p(\xi,\eta) = \varepsilon^2 P_2(\xi,\eta) + \varepsilon^3 P_3(\xi,\eta) + \cdots . \tag{2.4.5}$$

A hierarchy of problems is obtained to different orders by inserting (2.4.4) and (2.4.5) in (2.4.1). Only one boundary condition in the x direction is required for each problem. Accordingly, the condition in the equation (2.4.1d) which is the far-upstream condition is adequate for the problems to be well posed. This, in turn, eliminates the necessity of matching with the inner layer flow at the channel exit (x = 0). In addition, it is not required to introduce rescaling in the streamwise (x) direction unless one wants to capture the flow structure very close to the origin. Consequently, the order of x is assumed to remain at least of O(1); an upstream distance very close to the origin, i.e. from the channel exit is precluded in the current formulation. This is not the case of the flow in a constricted (dilated) channel, where the streamwise direction x is rescaled in terms of the inverse power of the indentation slope (and the Reynolds number), which makes it possible to capture the flow close to the inception of the constriction (dilation). In order to determine the flow through and past the constriction (dilation) (Smith 1976) rescaling of x is essential. However, in the present case, the flow is discontinuous through the singularity.

To determine the additional boundary conditions needed to solve the problem (2.4.1) matching between the lower-wall and the core layers is considered next. From the core layer first recall that, the perturbations $\psi_1(x,z) = \psi_2(x,z) = 0$. Thus, equation (2.5.2) is conveniently written here as,

$$\psi(x,z) = (1-G)\frac{y^2}{2} + G\frac{y^3}{3} + \varepsilon^3 \psi_3(x, z = y) + \cdots . \tag{2.4.6}$$

Applying E_0 (refer to equation 2.8.1 in the section 2.8) in (2.4.6), it is clear that,

$$E_0\psi = (1-G)\frac{y^2}{2} + G\frac{y^3}{3}. \tag{2.4.7}$$

When the inner variable expansion H_3 is applied, it is clear that,

$$H_3E_0\psi = (1-G)\frac{\varepsilon^2\eta^2}{2} + G\frac{\varepsilon^3\eta^3}{3} = (1-G)\frac{y^2}{2} + G\frac{y^3}{3}. \qquad (2.4.8)$$

Also, from (2.4.4), $H_3\psi = \varepsilon^2\Psi_2 + \varepsilon^3\Psi_3$. Setting $H_3E_0\psi = E_0H_3\psi$, it is deduced that $\Psi_2 \sim (1-G)\frac{\eta^2}{2}$ and $\Psi_3 \sim G\frac{\eta^3}{3}$ for large η.

To the leading order, equations (2.4.1) reduce to,

$$\Psi_{2\eta}\Psi_{2\xi\eta} - \Psi_{2\xi}\Psi_{2\eta\eta} = -P_{2\xi} + \Psi_{2\eta\eta\eta}, \qquad P_{2\eta} = 0. \qquad (2.4.9)$$

The boundary conditions for the above problems are,

$$\Psi_2(\xi, \eta = 0) = \Psi_{2\eta}(\xi, \eta = 0) = 0, \qquad (2.4.10a)$$

$$\Psi_2(-\xi, \eta) \sim (1-G)\frac{\varepsilon^2\eta^2}{2}. \qquad (2.4.10b)$$

To the next order, the expressions (2.4.1) lead to the following problems,

$$\Psi_{2\eta}\Psi_{3\xi\eta} - \Psi_{3\xi}\Psi_{2\eta\eta} = -P_{3\xi} + \Psi_{3\eta\eta\eta}, \qquad P_{3\eta} = 0. \qquad (2.4.11)$$

Subject to the following boundary conditions,

$$\Psi_3(\xi, \eta = 0) = \Psi_{3\eta}(\xi, \eta = 0) = 0, \qquad (2.4.12a)$$

$$\Psi_3(-\xi, \eta) \sim G\frac{\varepsilon^3\eta^3}{3}. \qquad (2.4.12b)$$

Matching the pressure leads to,

$$P_{2\xi}(\xi, \eta) = 0, \qquad P_{3\xi}(\xi, \eta) = 2G. \qquad (2.4.13)$$

Incidentally, it is not difficult to show that the solutions to $O(\varepsilon^2)$ and $O(\varepsilon^3)$ are,

$$\Psi_2(\xi,\eta)=(1-G)\frac{\eta^2}{2}, \qquad P_2(\xi,\eta)=0, \tag{2.4.14}$$

$$\Psi_3(\xi,\eta)=G\frac{\eta^3}{3}, \qquad P_3(\xi,\eta)=2G\xi. \tag{2.4.15}$$

Thus, up to $O(\varepsilon^3)$, the flow does not deviate and preserves its Couette-Poiseuille character near the lower wall.

Before proceeding to the next order, it is necessary to determine the inner value $\psi_3(x<0, z\to 0)$ for the core flow problem at this stage. First noting from (2.4.6) that

$$E_3\psi=(1-G)\frac{y^2}{2}+G\frac{y^3}{3}+\varepsilon^3\left[\psi_3(x,0)+y\psi_{3y}(x,0)+\frac{1}{2}y^2\psi_{3yy}(x,0)+...\right]. \tag{2.4.16}$$

Hence,

$$H_3E_3\psi=(1-G)\frac{y^2}{2}+G\frac{y^3}{3}+\varepsilon^3\psi_3(x,0). \tag{2.4.17}$$

Also, from (2.4.4), (2.4.14) and (2.4.15),

$$H_3\psi=(1-G)\frac{y^2}{2}+G\frac{y^3}{3}. \tag{2.4.18}$$

This leads to,

$$E_3H_3\psi=(1-G)\frac{y^2}{2}+G\frac{y^3}{3}. \tag{2.4.19}$$

Matching (2.4.17) and (2.4.19) yields,

$$\psi_3(x<0, z=0)=0. \tag{2.4.20}$$

This is the required to determine the core flow upstream of the channel exit (refer to the problem (2.5.5) in the next section).

Now, from (2.4.1) the equations for Ψ_4 and P_4 are,

$$\Psi_{2\eta}\Psi_{4\xi\eta} - \Psi_{4\xi}\Psi_{2\eta\eta} = -P_{4\xi} + \Psi_{4\eta\eta\eta}, \qquad P_{4\eta} = 0. \qquad (2.4.21)$$

Clearly, $P_4(\xi,\eta) \equiv P_4(\xi)$. Indeed, the above expression confirms that the problem is of the boundary-layer type, which requires only one boundary condition in the streamwise direction. Next, the matching condition is sought, which is needed in addition to the wall conditions to determine the disturbances Ψ_4 and P_4.

Taking m = 4 and n = 3 in (2.4.6) (refer to section 2.8),

$$H_4E_3\psi = 3y^2 - 2y^3 + \varepsilon^3 y\psi_{3y}(x, z=0) = (1-G)\frac{y^2}{2} + G\frac{y^3}{3} + \varepsilon^4\eta\psi_{3z}(x, z=0). \quad (2.4.22)$$

And comparing with

$$E_3H_4\psi = (1-G)\frac{y^2}{2} + G\frac{y^3}{3} + \varepsilon^4\Psi_4, \qquad (2.4.23)$$

yields the desired matching condition for large η, namely,

$$\Psi_4(\xi, \eta\to\infty) \sim \eta\psi_{3z}(x, z=0), \qquad (2.4.24)$$

where $\psi_{3z}(\xi, z=0) = \sum_{n=1}^{\infty} \frac{A_n}{\beta_n} e^{\beta_n\xi} V_n'(z=0)$ is deduced from (2.5.10). It is to be noted that $V_n'(z=0)$ is obtained from the solution of the eigenvalue problem (2.5.8), with β_n being the eigenvalues. In addition, the coefficients A_n are obtained from matching the upstream and downstream core flow at x = 0 as per (2.5.15). In the table 1 and table 2, the values A_n for the first six modes are stated.

By using (2.4.14) and eliminating the pressure gradient from the expression (2.4.21), finally, the problem for $\Psi_4(\xi,\eta)$ becomes,

$$(1-G)\eta\Psi_{4\xi\eta\eta} = \Psi_{4\eta\eta\eta\eta}, \tag{2.4.25a}$$

$$\Psi_4(\xi,\eta=0) = \Psi_{4\eta}(\xi,\eta=0) = 0, \qquad \Psi_4(\xi\to-\infty,\eta)\sim 0, \tag{2.4.25b}$$

$$\Psi_4(\xi,\eta\to\infty)\sim\eta\sum_{n=1}^{\infty}\frac{A_n}{\beta_n}e^{\beta_n\xi}. \tag{2.4.25c}$$

Following Khayat (2017), the problem (2.4.25) is solved by seeking a similarity solution of the form $\Psi_4(\xi,\eta)=\sum_{n=1}^{\infty}\frac{A_n}{\beta_n}e^{\beta_n\xi}F_n(\eta)$, where the functions $F_n(\eta)$ are governed by

$$F_n''''=(1-G)\eta\beta_n F_n'', \tag{2.4.26a}$$

$$F_n(0)=F_n'(0)=0, \qquad F_n'(\infty)\sim 1, \qquad F_n''(\infty)\sim 0. \tag{2.4.26b}$$

Problem (2.4.26) is a two-point boundary-value, which is solved numerically for each mode separately. Figure 2.20 illustrates the profiles of $F_n'(\eta)$ for the first six modes for the values of G=0.4, reflecting a monotonic growth of $F_n(\eta)$ and its derivatives. Predominantly, significant departure is observed for the first mode ($\beta_1=3.5161$) from the rest modes. This, in turn, reflects the dominance of the first mode on the velocity. Since $F_n''(\eta=0)$ and $F_n'''(\eta=0)$ are directly related to the shear stress at the wall and pressure, respectively, their values are listed in the table 1 and table 2. In particular, for all modes, $F_n''(\eta=0)>0$ and $F_n'''(\eta=0)<0$. To the current order, using equations (2.4.2), (2.4.3) and (2.4.4) the velocity components are given by

$$u(\xi,\eta)=(1-G)\varepsilon\eta+G\varepsilon^2\eta^2+\varepsilon^3\sum_{n=1}^{\infty}\frac{A_n}{\beta_n}e^{\beta_n\xi}F_n'(\eta), \tag{2.4.27}$$

$$w(\xi,\eta) = -\varepsilon^4 \sum_{n=1}^{\infty} \frac{A_n}{\beta_n} e^{\beta_n \xi} F_n(\eta). \tag{2.4.28}$$

In this case, the pressure and wall shear stress at the lower wall turn out to be,

$$p(\xi,\eta) = \varepsilon^3 2G\xi + \varepsilon^4 \sum_{n=1}^{\infty} \frac{A_n}{\beta_n} e^{\beta_n \xi} F_n'''(\eta=0), \tag{2.4.29}$$

$$\tau(\xi,\eta=0) = 1 - G + \varepsilon^2 \sum_{n=1}^{\infty} \frac{A_n}{\beta_n} e^{\beta_n \xi} F_n''(\eta=0). \tag{2.4.30}$$

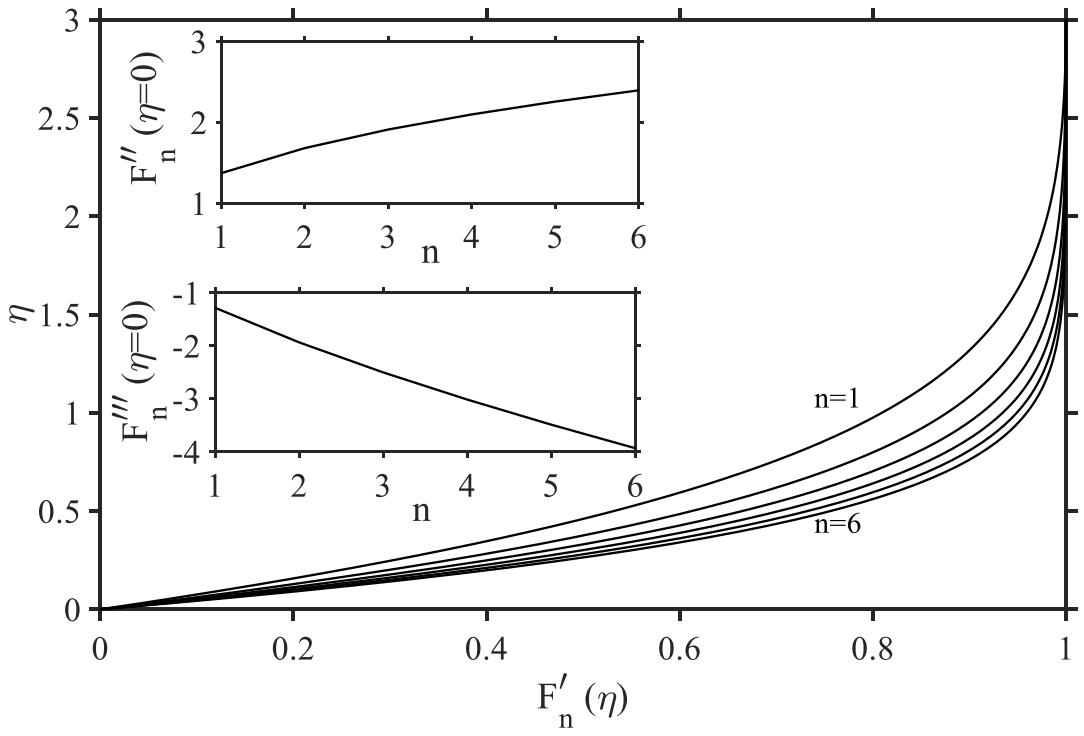

Figure 2.20: the profiles of $F_n'(\eta)$ for the first six eigen modes (G=0.4). Also the values of $F_n''(\eta=0)$ and $F_n'''(\eta=0)$ are shown in the insets.

So, the asymptotes for the velocity components become,

$$u(\xi,\eta\to\infty) \sim (1-G)\varepsilon\eta + G\varepsilon^2\eta^2 + \varepsilon^3 \sum_{n=1}^{\infty} \frac{A_n}{\beta_n} e^{\beta_n \xi}, \tag{2.4.31}$$

$$w\left(\xi,\eta\to\infty\right)\sim-\varepsilon^4\sum_{n=1}^{\infty}\frac{A_n}{\beta_n}e^{\beta_n\xi}. \tag{2.4.32}$$

The flow development near the lower wall is depicted in the figures 2.21 and 2.22 for G=0.4 and G=-0.4, respectively. In the figures, the disturbances profiles of the streamwise (2.21) and depthwise (2.22) velocities are shown at equal intervals for $-0.25<x<0$. As expected, in the limit $x\to-\infty$ both disturbances vanish exponentially. Likewise, the asymptote reflecting the extent of the (inviscid) character of the core flow does not satisfy adherence at the lower wall. When the fluid approaches the exit, a significant elongation is noticed, which is reflected from the drastic departure of the value of $W_4\left(x=0,z\right)$ from zero. The shear stress at the wall always turns out to be positive. Thus, it is confirmed that there is no possibility of separation upstream of the channel exit along the lower wall. In the figures 2.23 and 2.24, the influence of inertia on the development of the pressure and the shear stress along the lower wall upstream of the channel exit are illustrated, respectively. Interestingly, the pressure remains close to the Poiseuille level. Depending on the sign of G, it increases/decreases essentially linearly all the way to the exit, but reaches a positive/negative level at the exit. Surprisingly, the level of shearing decreases with increasing inertia for any G value, which indicates flattening of the velocity profile near the channel exit. Both the shear stress and the pressure exhibit singularity at x = 0. This is because when the fluid moves along the lower wall and emerges along the jet free surface, it experiences vanishing shear stress and pressure at the free surface. However, the pressure and the wall shear stress are remained to Couette-Posieuille level upstream of the channel exit.

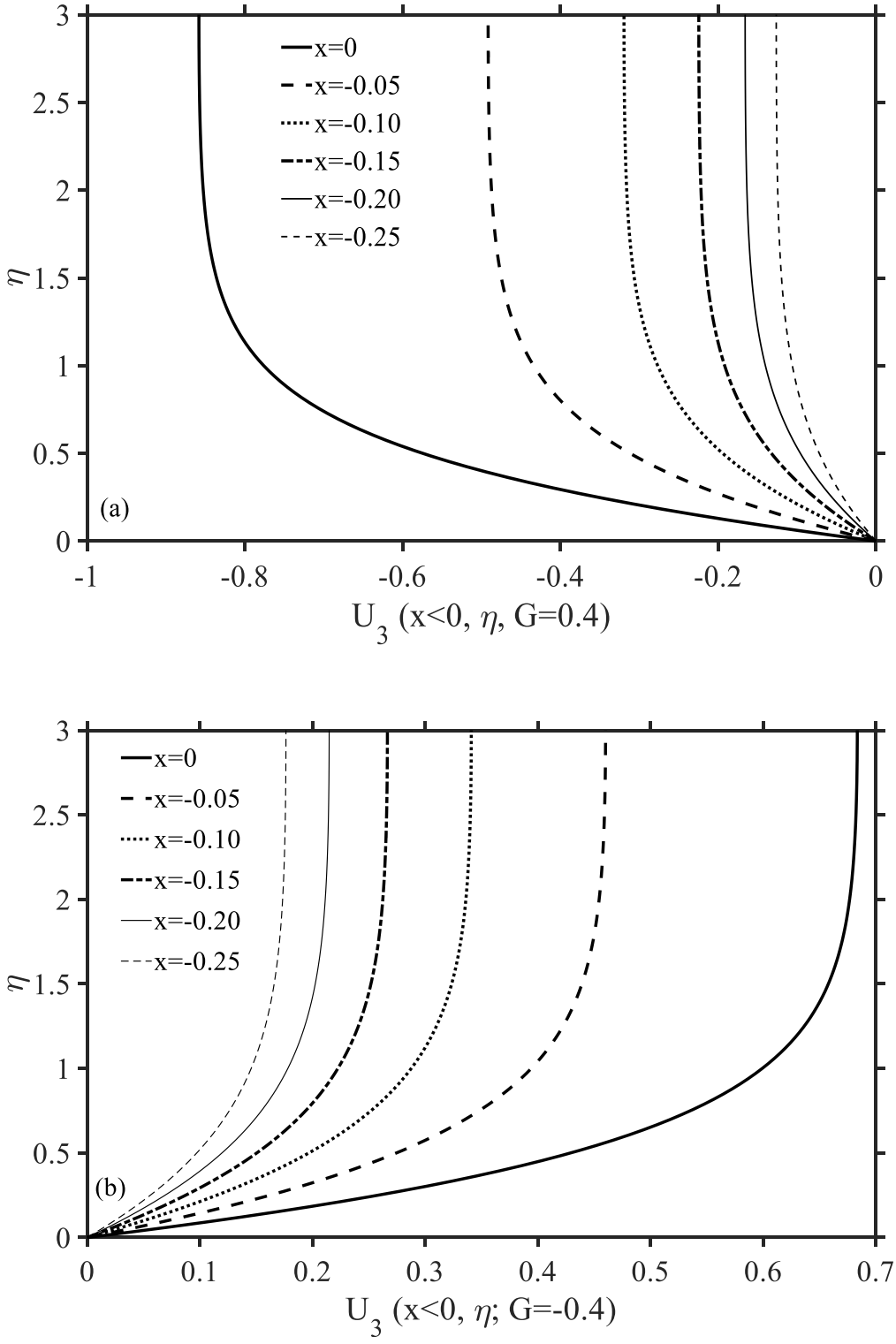

Figure 2.21: Streamwise velocity disturbance profiles near the lower wall for (a) G=0.4 and (b) G=-0.4.

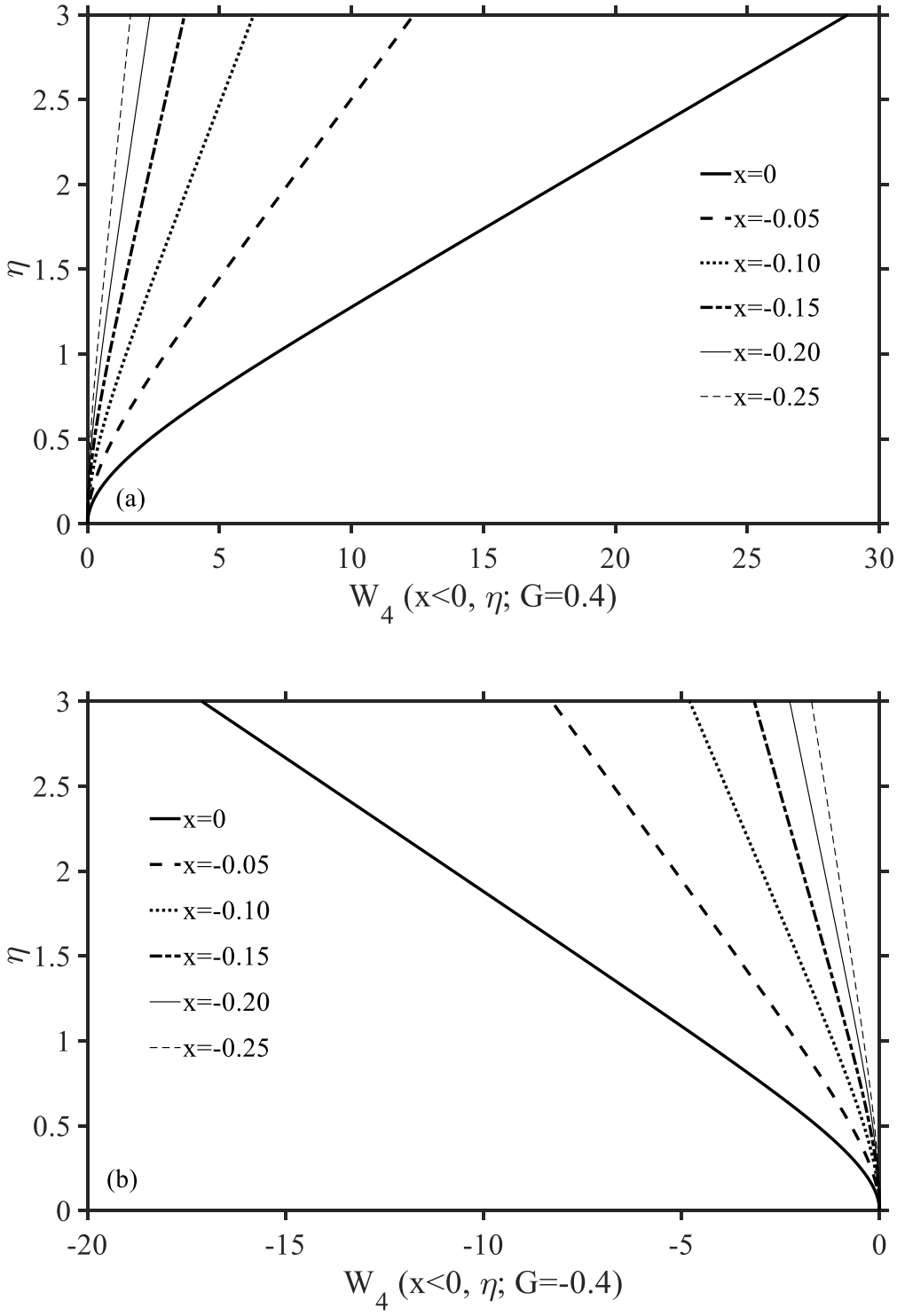

Figure 2.22: Transverse velocity disturbance profiles near the lower wall for (a) G=0.4 and (b) G=-0.4.

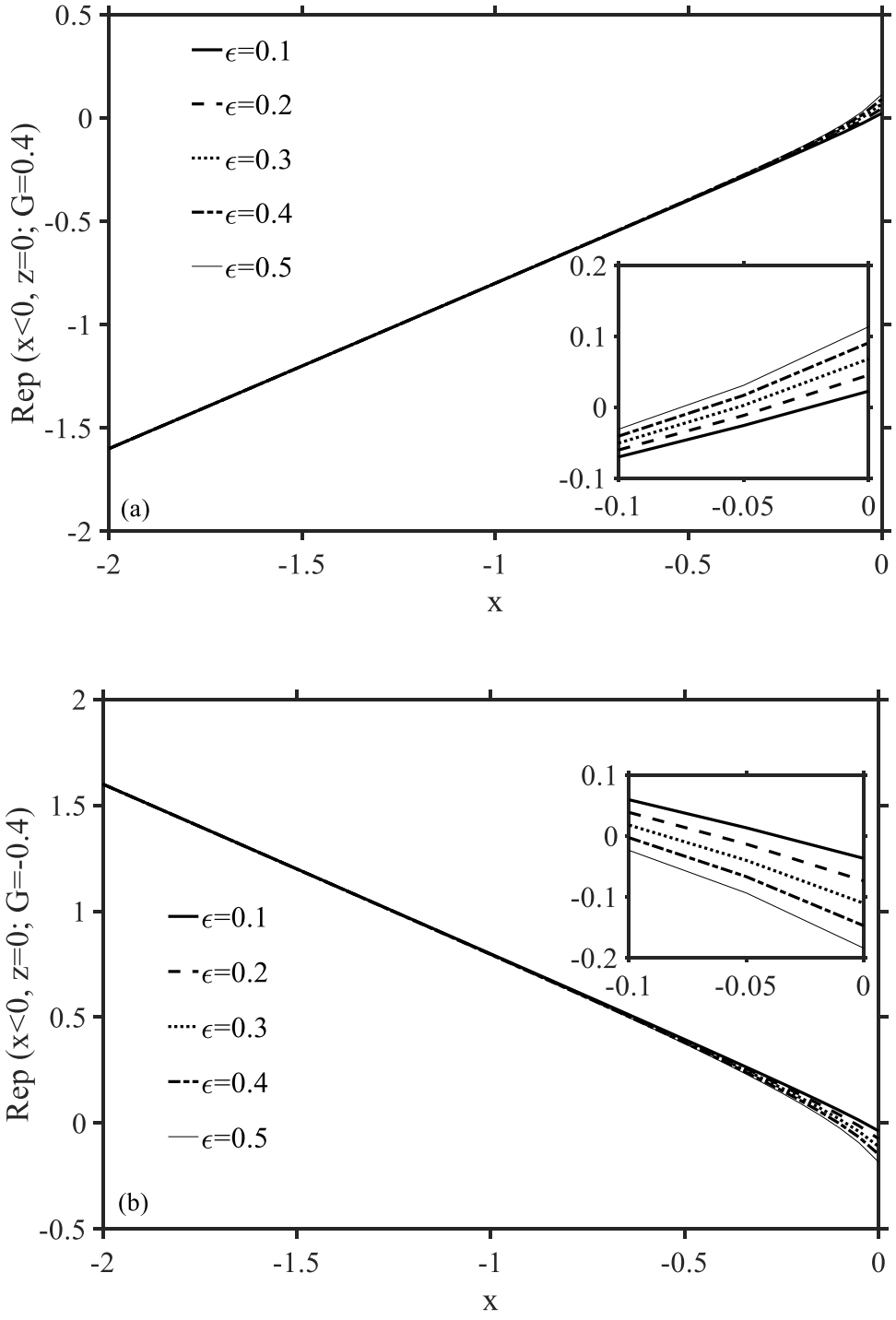

Figure 2.23: Influence of inertia on pressure along the lower wall for (a) G=0.4 and (b) G=-0.4.

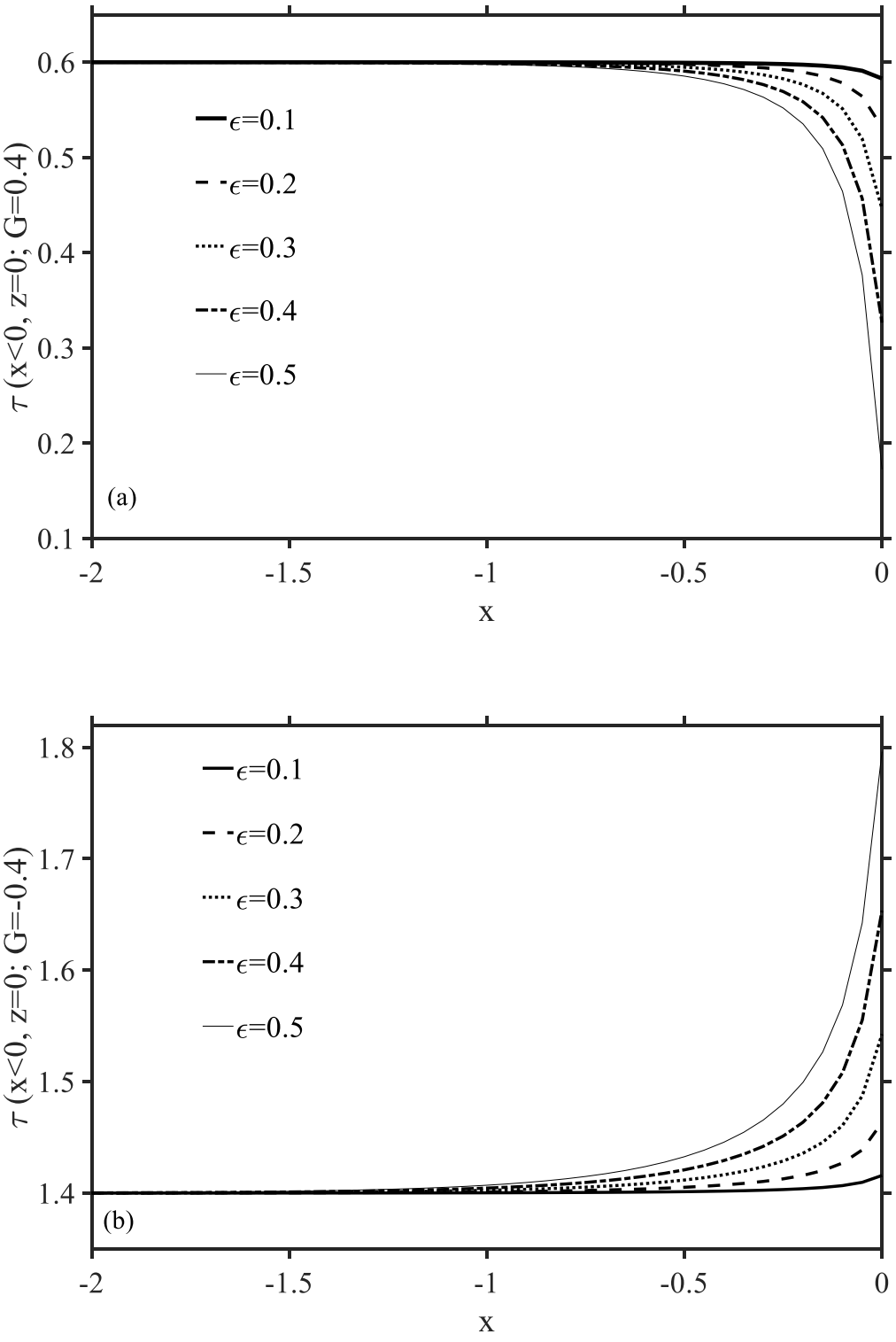

Figure 2.24: Influence of inertia on the wall shear stress along the lower wall for (a) G=0.4 and (b) G=-0.4.

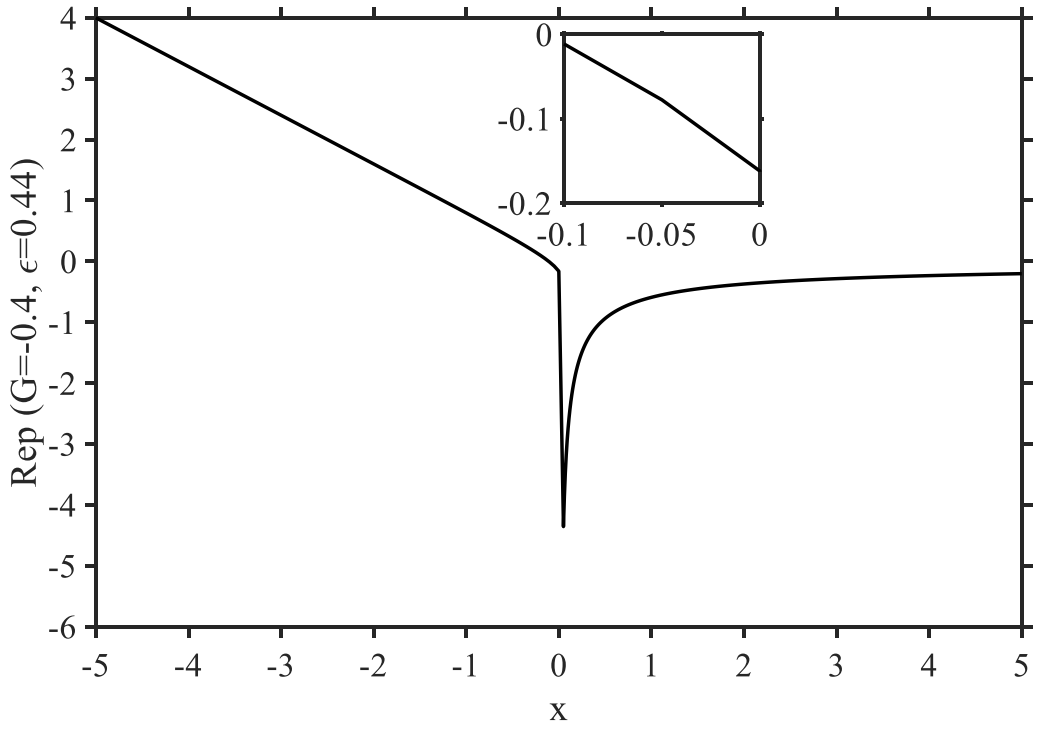

Figure 2.25: Pressure profile along the lower wall and free surface for $\varepsilon = 0.44$ and G=-0.4. Inset shows the magnification of the area very close to the exit inside the channel.

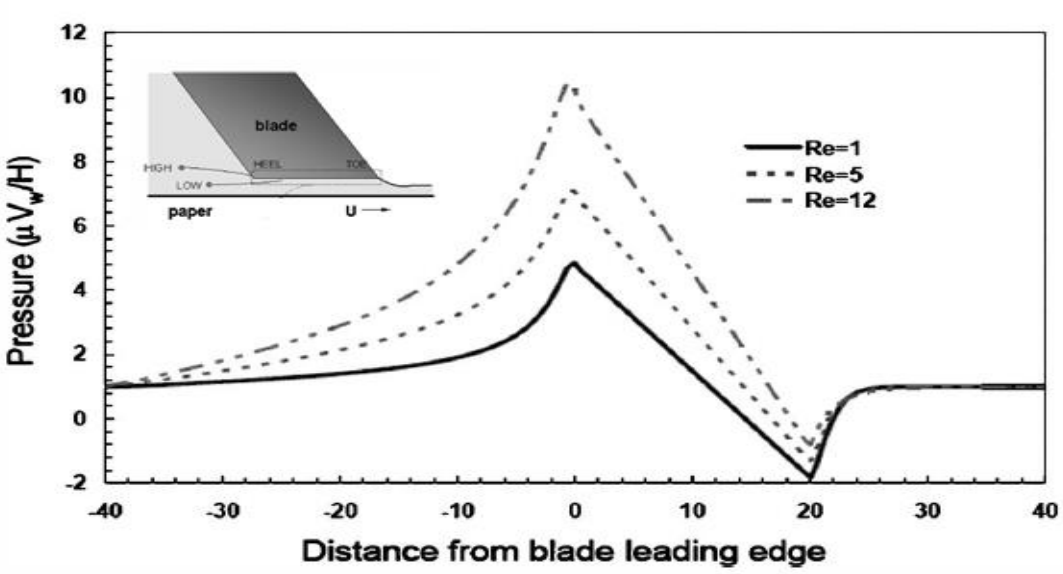

Figure 2.26: Pressure profile for trailing stiff blade geometry for Re=12 (figure 9 of Lliopoulos and Scriven 2005). Inset shows the blade configuration (figure 4 of Lliopoulos and Scriven 2005).

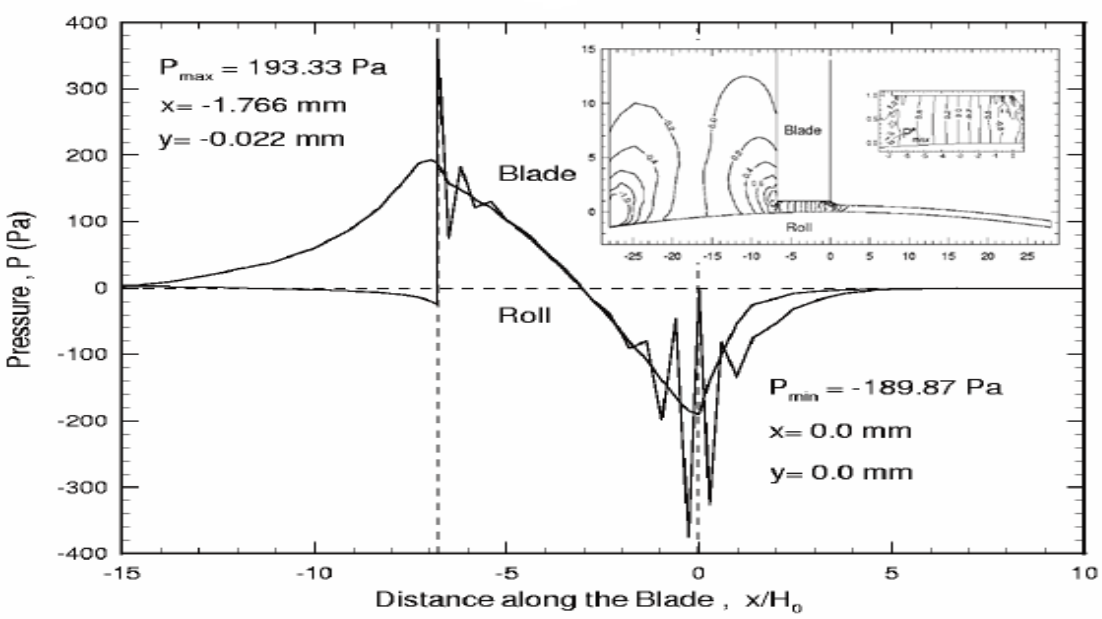

Figure 2.27: Pressure distribution in the blade coating of a shear-thinning fluid obeying the Carreau model for S010 geometry (figure 11b of Mitsoulis and Athanasopoulos 2010). Inset shows the S010 geometry (figure 11a of Mitsoulis and Athanasopoulos 2010).

In the figure 2.25, the pressure profile along the lower wall and on the free surface is plotted for G=-4 and $\varepsilon = 0.44$. The pressure decreases essentially linearly with the distance and drops lower than the ambient value at the region close to the exit both upstream and downstream. This is due to the acceleration of the flow as it moves along the curved free surface. Gradually, it rises back to the ambient level, i.e. to zero. This behavior agrees qualitatively well with the numerical results of the blade coating flow of Lliopoulos and Scriven (2005) and Mitsoulis and Athanasopoulos (2010). For the convenience, the pressure profiles along the blade and on the free surface of the above-mentioned investigations are illustrated in the figures 2.26 and 2.27, respectively. From the figure 2.26, it can be seen that as the Reynolds number increases less dip in the pressure occurs along the blade close to the exit, and the pressure on the frees surface also diminishes quickly to zero with the increasing level of inertia. Similar trends are found from the current analysis, which are depicted in the figures 2.23 b and 2.18, respectively. However, a

singularity in the pressure is present in the current results that cannot be seen in both of the numerical analyses.

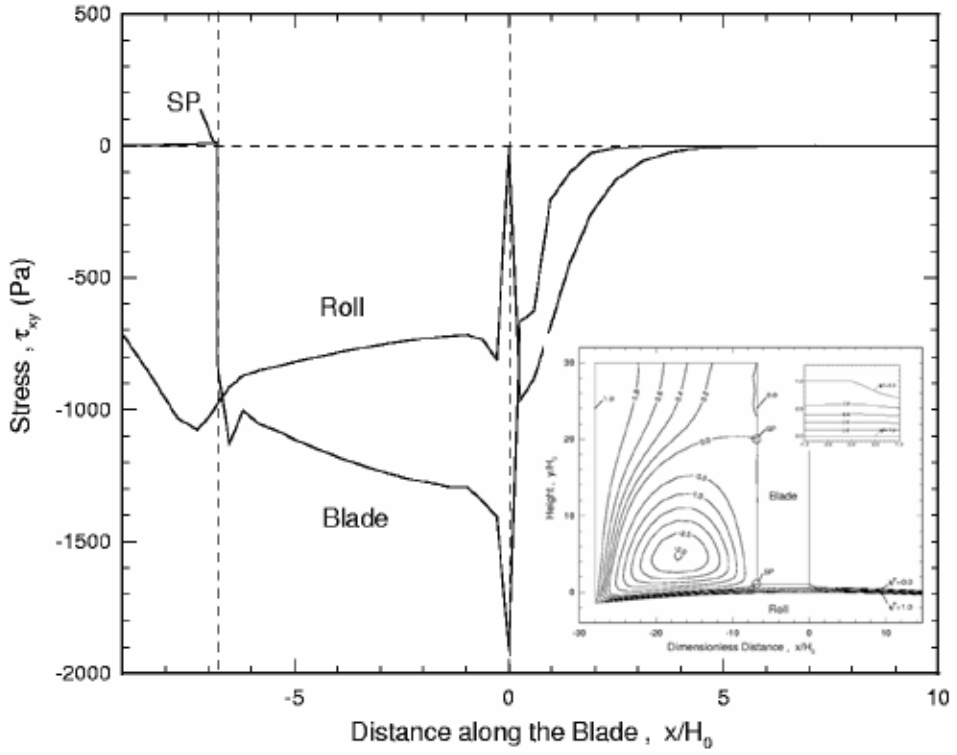

Figure 2.28: Axial shear stress profile along the blade wall and roll for a Newtonian fluid in the S010 geometry (figure 8a of Mitsoulis and Athanasopoulos 2010). Inset shows the S010 geometry (figure 7a of Mitsoulis and Athanasopoulos 2010).

Figure 2.24b illustrates the shear stress development at the lower wall for the different level of inertia and G=-0.4. From the figure, it is evident that the shear stress retains its Couette-Poiseuille level inside the channel expect very close to the exit. A jump in the shear stress value is observed very close to the channel exit since the fluid starts to feel the presence of singularity upon approaching the exit. This characteristic is reminiscent of the numerical result obtained by Mitsoulis and Athanasopoulos (2010) for the shear stress along the blade, which is presented in the figure 2.28 for convenience purpose. However, the discrepancy in the direction of the jump is due to the different geometric orientation considered in the present study.

2.5 Flow in the core layer

For convenience, the core region is divided into two different regions: outside the channel ($x > 0$) and inside the channel ($x < 0$) from the exit ($x = 0$). In this layer, the solution of the problems (2.1.4) is sought in each of the regions separately. For this purpose, equations (2.1.4) are conveniently rewritten here as

$$\psi_z\psi_{xz} - \psi_x\psi_{zz} = -p_x + \varepsilon^3\left(\psi_{xxz} + \psi_{zzz}\right) \tag{2.5.1a}$$

$$\psi_x\psi_{xz} - \psi_z\psi_{xx} = -p_z - \varepsilon^3\left(\psi_{xxx} + \psi_{xzz}\right) \tag{2.5.1b}$$

The stream function and pressure are represented here by the following outer expansions:

$$\psi = \psi_0 + \varepsilon\psi_1 + ..., \tag{2.5.2a}$$

$$p = p_0 + \varepsilon p_1 + \cdots. \tag{2.5.2b}$$

Here, $\psi_0 = (1-G)z + Gz^2$ is just the basic Couette- Poiseuille flow stream function provided in (2.1.3). For $m > 0$, ψ_m corresponds to the higher order terms that denote the deviation from the base flow due to its interaction with the boundary layers. This behavior of the base flow is similar to the laminar free jet flow (Tillett 1968; Saffari & Khayat 2008; Khayat2014; Khayat 2017) and tube or channel flow with a constriction (Smith 1979). To leading order, the fully developed profile is applied in such cases also. At high Reynolds number, Smith studied the flow for three different levels of constriction: fine, moderate (1976) and sever (1979). The constriction severity is reflected in the obstacle characteristic slope, which is of $O\left(Re^{-1/3}\right)$ and $O\left(Re^{-1/6}\right)$ for fine and moderate constrictions, respectively. Smith defined the Reynolds number Re based on the tube diameter and maximum velocity. In this case, the non-linear influence of the obstacle in the upstream is absent, and the core flow is just an inviscid rotational perturbation of the base flow. The current problem also encounters the similar situation, where the jet contraction resembles

to a fine to moderate constriction, and outside the inner and wall layers, the core flow is of the inviscid elliptic, but linear in nature.

In contrast, for severe constriction, the obstacle slope is of O(1). Therefore, this creates a significant upstream influence on the core flow. The current problem does not correspond to this level of constriction severity as mentioned before. Note that regardless of the constriction level of severity, the flow field expansion takes the same form. Hence, the above expansion (2.5.2a) is the same as expansion (2.1) for the flow with a severe constriction (Smith 1979). Although the leading order terms in (2.1) do not exactly correspond to fully developed flow, they still satisfy the inviscid equations of motion.

Due to the elliptic nature of the governing equations, the deviation from base flow will also extend to the region $x<0$ upstream of the channel exit $x=0$. Following these assumptions, a hierarchy of equations is obtained to each order upon inserting expressions (2.5.2) into equations (2.1.4). To leading order $p_0(x,z)=0$. For $m=1$ and $n=2$, the matching conditions obtained in section 2.4 and 2.8, and the condition $\psi_{m>0}(x\to-\infty,z)=0$, lead to the vanishing of the stream function and pressure everywhere. More explicitly,

$$\psi_1(x,z)=\psi_2(x,z)=p_1(x,z)=p_2(x,z)=0. \tag{2.5.3}$$

To next order, $m=3$, equations (2.1.4) lead to

$$\psi_{0z}\psi_{3xz}-\psi_{3x}\psi_{0zz}=-p_{3x}+2G, \tag{2.5.4a}$$

$$-\psi_{0z}\psi_{3xx}=-p_{3z}. \tag{2.5.4b}$$

Upon eliminating p_3 from the above equations, the following equation is obtained for ψ_3:

$$\nabla^2\psi_{3x}-\frac{\psi_{0zzz}}{\psi_{0z}}\psi_{3x}=0, \tag{2.5.5}$$

where $\nabla^2 = \frac{\partial^2}{\partial x^2} + \frac{\partial^2}{\partial z^2}$. Noting that $w_3 = -\psi_{3x}$, the following boundary-value problem is obtained for the ranges - $-\infty \le x \le \infty$ and $0 \le z \le 1$:

$$\nabla^2 w_3 - \frac{2G}{(1-G)z + Gz^2} w_3 = 0, \tag{2.5.6a}$$

$$\begin{aligned} &w_3(x,1) = 0, \\ &w_3(x,0) = 0 \qquad \text{for} \quad x < 0, \\ &w_3(x, z \to 0) = \frac{2G}{1-G} \quad \text{for} \quad x > 0, \\ &w_3 \quad \text{bounded as } |x| \to \infty. \end{aligned} \tag{2.5.6b}$$

Matching between the inner and core flow provides the condition $w_3(x > 0, z \to 0) = \frac{2G}{1-G}$ (see section 2.8 for details). The non-homogeneity of the boundary condition prohibits the vanishing of the solution. Even though the formulation is common to both core flow regions, they will be examined separately for convenience purpose.

2.5.1 Flow in the core layer upstream of the channel exit $(x < 0)$

Now, consider the core flow in the region inside the channel ($x < 0$). Equation (2.5.6a) is a second order linear equation with non-constant coefficient in z. In this case, the following form of the solution is achieved using the separation of variable argument (Tillett 1968):

$$w_3(x < 0, z) = -\psi_{3x} = -\sum_{n=1}^{\infty} A_n e^{\beta_n x} V_n(z). \tag{2.5.1.1}$$

Here, V_n are the shape functions and governed by the following eigenvalue problem:

$$V_n'' + \left(\beta_n^2 - \frac{2k}{z + kz^2}\right) V_n = 0, \qquad V_n(0) = Vn(1) = 0, \tag{2.5.1.2}$$

where, $k = \frac{G}{1-G}$ and β_n is real and positive.

G		n	β_n	A_n	$F_n''(0)$	$F_n'''(0)$
	0.2	1	3.3111	-0.3824	1.4768	-1.4896
		2	6.3965	-0.4362	1.8357	-2.3061
		3	9.5102	-0.4559	2.0948	-3.0036
		4	12.6362	-0.4655	2.3030	-3.6301
		5	15.7661	-0.4704	2.4792	-4.2072
		6	18.9010	-0.4731	2.6337	-4.7478
	0.4	1	3.5161	-0.6998	1.3716	-1.2825
		2	6.5498	-0.9442	1.6817	-1.9347
		3	9.6320	-1.0565	1.9115	-2.5008
		4	12.7380	-1.1182	2.0980	-3.0127
		5	15.8540	-1.1553	2.2567	-3.4858
		6	18.9780	-1.1788	2.3962	-3.9299
	0.6	1	3.7694	-0.8580	1.2333	-1.0313
		2	6.7715	-1.4400	1.4876	-1.5117
		3	9.8205	-1.7996	1.6815	-1.9341
		4	12.9010	-2.0293	1.8409	-2.3191
		5	15.9972	-2.1829	1.9775	-2.6764
		6	19.1061	-2.2900	2.0980	-3.0126
	0.8	1	4.0890	-0.6949	1.0314	-0.7053
		2	7.1231	-1.5502	1.2119	-0.9945
		3	10.1600	-2.3609	1.3552	-1.2514
		4	13.2170	-3.0486	1.4758	-1.4876
		5	16.2901	-3.6094	1.5806	-1.7083
		6	19.3780	-4.0628	1.6740	-1.9169

Table 1: Values for the first six modes for $[G \in 0.2, 0.8]$

		n	β_n	A_n	$F_n''(0)$	$F_n'''(0)$
G	-0.2	1	2.9983	0.4175	1.6333	-1.8245
		2	6.1950	0.3737	2.0788	-2.9577
		3	9.3580	0.3607	2.3851	-3.8937
		4	12.5123	0.3541	2.6276	-4.7257
		5	15.6610	0.3497	2.8317	-5.4885
		6	18.8090	0.3463	3.0100	-6.2013
	-0.4	1	2.8452	0.8381	1.6951	-1.9658
		2	6.1234	0.6838	2.1799	-3.2524
		3	9.3060	0.6434	2.5062	-4.2991
		4	12.4710	0.6242	2.7631	-5.2256
		5	15.6262	0.6121	2.9788	-6.0735
		6	18.779	0.6035	3.1670	-6.8652
	-0.6	1	2.7680	1.2564	1.7497	-2.0947
		2	6.0642	0.9460	2.2717	-3.5322
		3	9.2630	0.8723	2.6162	-4.6849
		4	12.4370	0.8385	2.8862	-5.7017
		5	15.5980	0.8180	3.1125	-6.6310
		6	18.755	0.8036	3.3097	-7.4979
	-0.8	1	2.6733	1.6088	1.7986	-2.2136
		2	6.0140	1.1374	2.3561	-3.7996
		3	9.2271	1.0337	2.7175	-5.0545
		4	12.4090	0.9873	2.9995	-6.1582
		5	15.5750	0.9597	3.2356	-7.1656
		6	18.7350	0.9405	3.4411	-8.1047

Table 2: Values for the first six modes for $\left[G \in -0.2, -0.8\right]$

Since the above problem is an eigenvalue problem, it is solved numerically subject to the additional boundary condition $V_n'(0) = 1$.The first six eigenvalues are tabulated in the table 1 and table 2 for the values of G from 0.2 to 0.8 and from -0.2 to -0.8, respectively.

Figure 2.29 depicts the dependence of the shape functions on the corresponding eigenvalues. Interestingly, V_n decreases with n whereas β_n increases. This facilitates reasonable convergence after only a few modes.

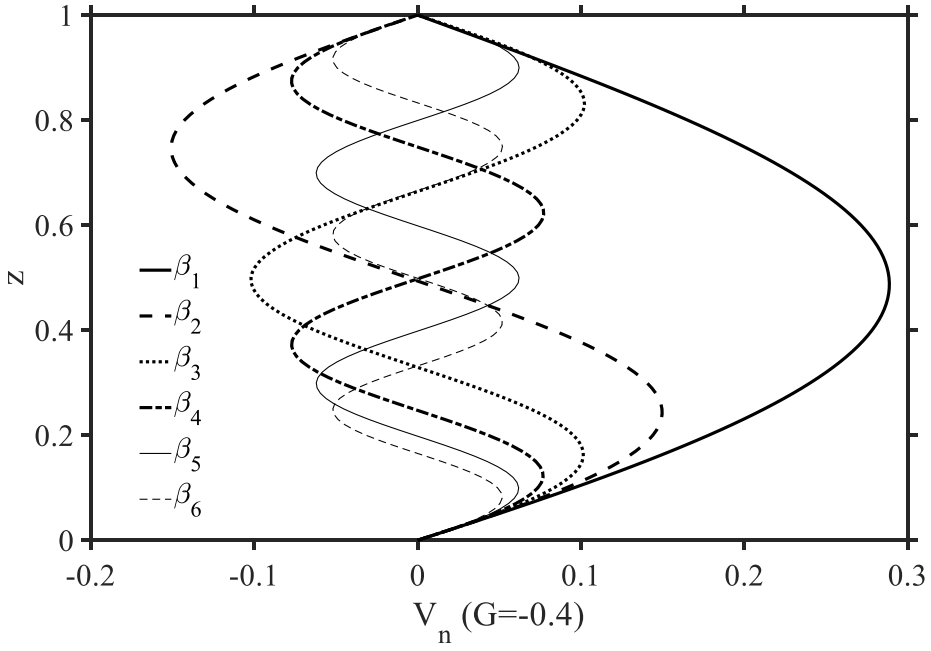

Figure 2.29: Shape function V_n vs z for the first six Eigen modes for $G = -0.4$.

By integrating expression (2.5.1.1) subject to $\psi_3(x \to -\infty, z) = 0$, leads to

$$\psi_3(x<0,z) = \sum_{n=1}^{\infty} \frac{A_n}{\beta_n} e^{\beta_n x} V_n(z). \tag{2.5.1.3}$$

So, the total stream function inside the channel becomes,

$$\psi(x<0,z) = (1-G)\frac{z^2}{2} + G\frac{z^3}{3} + \varepsilon^3 \sum_{n=1}^{\infty} \frac{A_n}{\beta_n} e^{\beta_n x} V_n(z). \tag{2.5.1.4}$$

The core streamwise velocity inside the channel to the order $O(\varepsilon^3)$ is given by,

$$u(x<0,z)=(1-G)z+Gz^2+\varepsilon^3\sum_{n=1}^{\infty}\frac{A_n}{\beta_n}e^{\beta_n x}V_n'(z). \qquad (2.5.1.5)$$

Finally, the coefficients A_n are obtained by matching the flow with the outside one at the channel exit, and will therefore be determined once the outside flow is considered.

2.5.2 Flow in the core layer downstream of the channel exit $(x>0)$

Downstream from the channel exit $x=0$, the solution of problem (2.5.5) takes the following form:

$$w_3(x>0,z)=-\psi_{3x}=\frac{2G}{1-G}V_0(z)+\sum_{n=1}^{\infty}A_n e^{-\beta_n x}V_n(z). \qquad (2.5.2.1)$$

Since, outside the channel the flow has to match with the inner layer flow, this matching forces the outside flow to have an additional term in the solution in the form of $V_0(z)$.

Here $V_0(z)$ satisfies the following equation and boundary conditions:

$$V_0''-\frac{2k}{z+kz^2}V_0=0,\quad V_0(0)=1,\qquad V_0(1)=0. \qquad (2.5.2.2)$$

Problem (2.5.2.2) admits an analytical solution in the form as,

$$V_0=2kz(1+kz)\ln\left(\frac{z}{1+kz}\right)+1+2kz+z(1+kz)\left[2k\ln(1+k)-\frac{1+2k}{1+k}\right]. \qquad (2.5.2.3)$$

The development of the function $V_0(z)$ with different G values is shown in the figure 2.30. As mentioned before, the coefficients A_n are found by matching both inside and outside w_3 at $x=0$. For this purpose, equating the expressions (2.5.1.1) and (2.5.2.1) at $x=0$, yields

$$V_0(z)=-\frac{1-G}{G}\sum_{n=1}^{\infty}A_n V_n(z). \qquad (2.5.2.4)$$

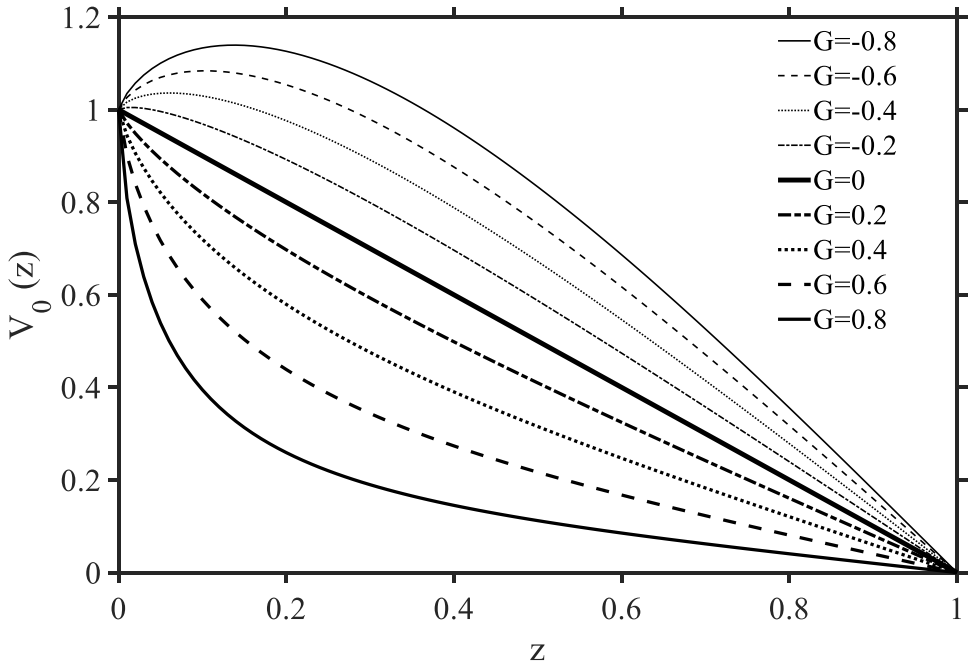

Figure 2.30: the profiles of function $V_0(z)$ for different G values

which is a spectral representation of $V_0(z)$ in terms of the orthogonal shape functions $V_n(z)$. Note that, by multiplying the equations in (2.5.1.2) and (2.5.2.2) by V_0 and V_n, respectively, then integrating, and using the conditions therein, it is not difficult to show that

$$\langle V_n U_0 \rangle = \frac{1}{\beta_n^2}, \tag{2.5.2.5}$$

where the brackets denote integration over the interval $0 \le z \le 1$. Consequently, using the orthogonality of the shape function, (2.5.2.4) yields

$$A_n = -\frac{G\langle V_n U_0 \rangle}{(1-G)\langle V_n^2 \rangle} = -\frac{G}{\beta_n^2 (1-G)\langle V_n^2 \rangle}. \tag{2.5.2.6}$$

Finally, the stream function is obtained by integration equation (2.5.2.1) and applying $\psi_3(x\to\infty, z=1)=0$, leads to

$$\psi_3(x>0,z)=-\frac{2G}{1-G}xV_0(z)+\sum_{n=1}^{\infty}\frac{A_n}{\beta_n}e^{-\beta_n x}V_n(z). \tag{2.5.2.9}$$

Therefore, the total stream function and streamwise velocity outside the channel take the following forms:

$$\psi(x>0,z)=(1-G)z^2+G\frac{z^3}{3}+\varepsilon^3\left[-\frac{2G}{1-G}xV_0(z)+\sum_{n=1}^{\infty}\frac{A_n}{\beta_n}e^{-\beta_n x}V_n(z)\right], \tag{2.5.2.10}$$

$$u(x>0,z)=(1-G)z+Gz^2+\varepsilon^3\left[-\frac{2G}{1-G}xV_0'(z)+\sum_{n=1}^{\infty}\frac{A_n}{\beta_n}e^{-\beta_n x}V_n'(z)\right]. \tag{2.5.2.11}$$

2.5.3 Pressure in the core layer and elsewhere

In this section the pressure distribution inside the core layer, inside and outside of the channel is considered. The pressure inside the channel is obtained by integrating equation (2.5.4b) subject to appropriate boundary conditions, which are determined as follows. First of all, recall from section 2.2 that the pressure in the inner layer was shown to be the order of ε^4. Therefore, for $x>0$, by matching the pressure in the core and inner layers it can be easily deduce that the pressure in the core region outside the channel vanishes at the interface between the two layers, or

$$p_3(x>0,z\to 0)=0. \tag{2.5.3.1}$$

Hence, at the channel exit, this gives to $p_3(x=0,z\to 0)=0$. Now, upon evaluating (2.1.3) and (2.5.1.1) at $z=0$, equation (2.5.4a) reduces to

$$p_{3x}(x<0,z=0)=2G. \tag{2.5.3.2}$$

Noting that the pressure must match a zero third order pressure from the inner solution at the channel exit, equation (2.5.3.2) is integrated subject to $p_3\left(x=0, z\to 0\right)=0$, which gives pressure near the wall inside the channel, namely,

$$p_3\left(x<0, z=0\right)=2Gx. \tag{2.5.3.3}$$

Now, upon inserting equation (2.1.3) and (2.5.1.1) into equation (2.5.4b), the expression for the transverse pressure gradient at any point inside the channel becomes

$$p_{3z}\left(x\le 0, z\right)=\left[\left(1-G\right)z+Gz^2\right]\sum_{n=1}^{\infty}A_n\beta_n e^{\beta_n x}V_n. \tag{2.5.3.4}$$

Which, upon using (2.5.1.2), is conveniently recast as,

$$p_{3z}\left(x\le 0, z\right)=-\sum_{n=1}^{\infty}\frac{A_n}{\beta_n}e^{\beta_n x}\left\{\left(\left[\left(1-G\right)z+Gz^2\right]V_n'\right)'-\left(\left[\left(1-G\right)+2Gz\right]V_n\right)'\right\}. \tag{2.5.3.5}$$

Finally, (2.5.3.5) is integrated subject to (2.5.3.3), leading to

$$p_3\left(x\le 0, z\right)=2Gx-\sum_{n=1}^{\infty}\frac{A_n}{\beta_n}e^{\beta_n x}\left\{\left[\left(1-G\right)z+Gz^2\right]V_n'-\left[\left(1-G\right)+2Gz\right]V_n\right\}. \tag{2.5.3.6}$$

Although Couette-Poiseuille conditions are theoretically recovered in the limit $x\to-\infty$, calculations based on expression (2.5.36) indicate that these conditions prevail essentially for x < - 1, corresponding to a distance approximately equal to one channel width. Now, consider the pressure outside the channel. Inserting expressions (2.1.3) and (2.5.2.1) into (2.5.4b) yields

$$p_{3z}\left(x\ge 0, z\right)=-\sum_{n=1}^{\infty}\frac{A_n}{\beta_n}e^{-\beta_n x}\begin{Bmatrix}\left(\left[\left(1-G\right)z+Gz^2\right]V_n'\right)'\\-\left(\left[\left(1-G\right)+2Gz\right]V_n\right)'\end{Bmatrix}. \tag{2.5.3.7}$$

Which, upon using (2.5.1.2), and integrating and matching with (2.5.3.6) at $x=0$ gives

$$p_3(x \geq 0, z) = -\sum_{n=1}^{\infty} \frac{A_n}{\beta_n} e^{-\beta_n x} \left\{ \left[(1-G)z + Gz^2 \right] V_n' - \left[(1-G) + 2Gz \right] V_n \right\}. \qquad (2.5.3.8)$$

Thus, the pressure is available at any point in the core region inside and outside the channel. Incidentally, these expressions are valid both in the inner and core layers as $\varepsilon^3 p_3(x,z)$ turns out to be equal to the composite pressure. In other words, the pressure everywhere is readily available and is given by $p(x,z) = \varepsilon^3 p_3(x,z) + O\left(\varepsilon^4\right)$. Figure 2.31 displays the influence of pressure gradient on the pressure distribution at the upper wall for different values of G. The pressure decreases monotonically with x and essentially becomes zero after some distance downstream of the channel exit. The figure also suggests that the core pressure is not affected by the G expect that when the magnitude increases it takes a bit longer distance to go to zero. The development of pressure in the core layer with different heights is presented in the figure 2.32. Surprisingly, regardless of the applied pressure gradient direction, the pressure decreases essentially linearly with distance x both upstream and downstream of the channel exit. Upon approaching to the channel exit, there is a sudden change in the slope from a constant value to a zero value. This is possibly the indication of the singularity, and close to the upper wall, the pressure changes smoothly. This behavior is reminiscent of a symmetric free jet where it tends to vanish essentially for any height downstream of the channel exit (refer to figure 3 in Tillett 1968). In fact, the figure also reflects that the jet contraction does not have any significant effect on the flow close to the upper wall, i.e. the effect is limited to the lower half of the core layer only.

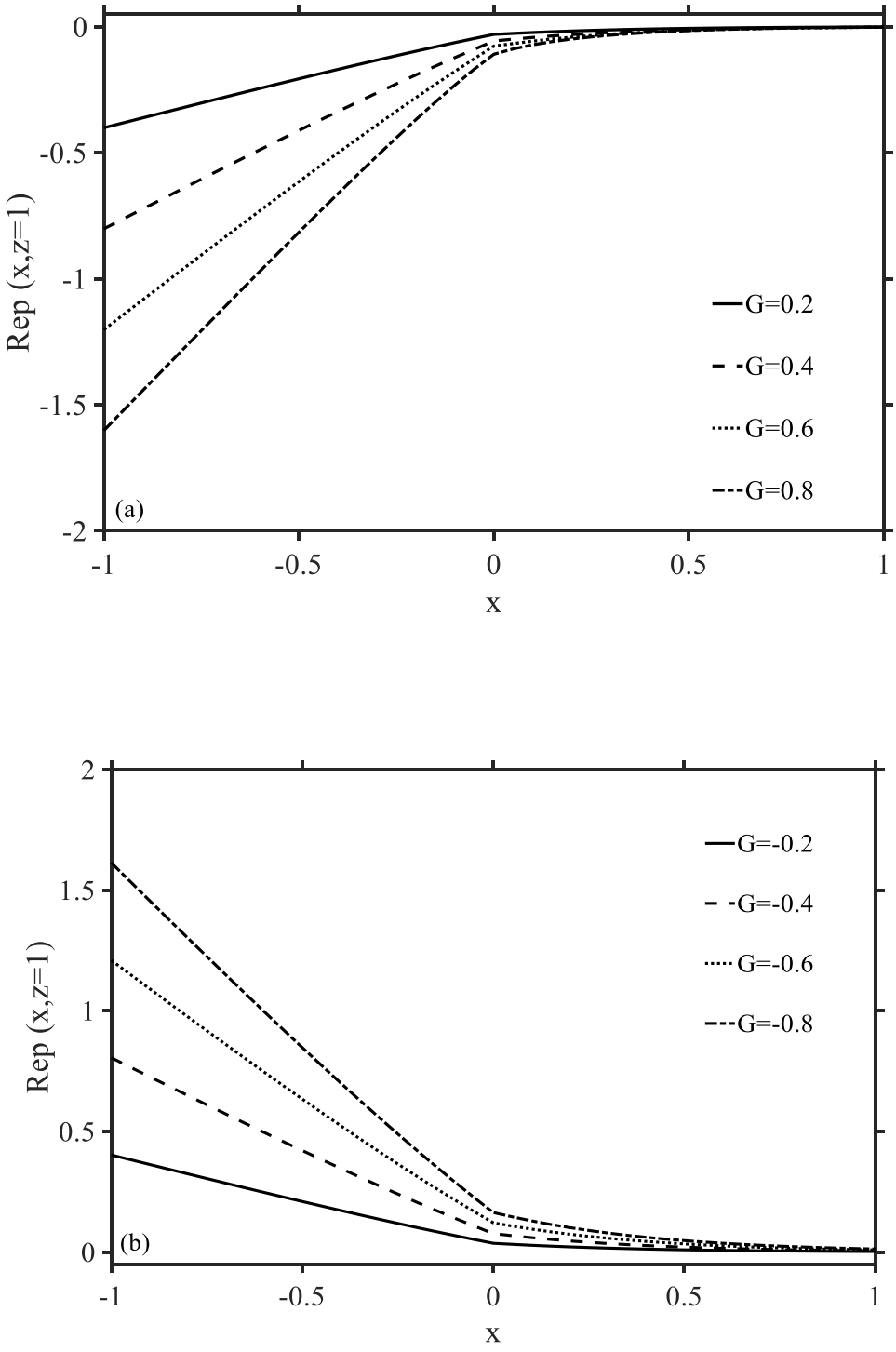

Figure 2.31: Influence of pressure gradient on the pressure distribution at the upper wall for (a) $G \in [0.2, 0.8]$ and (b) $G \in [-0.2, -0.8]$

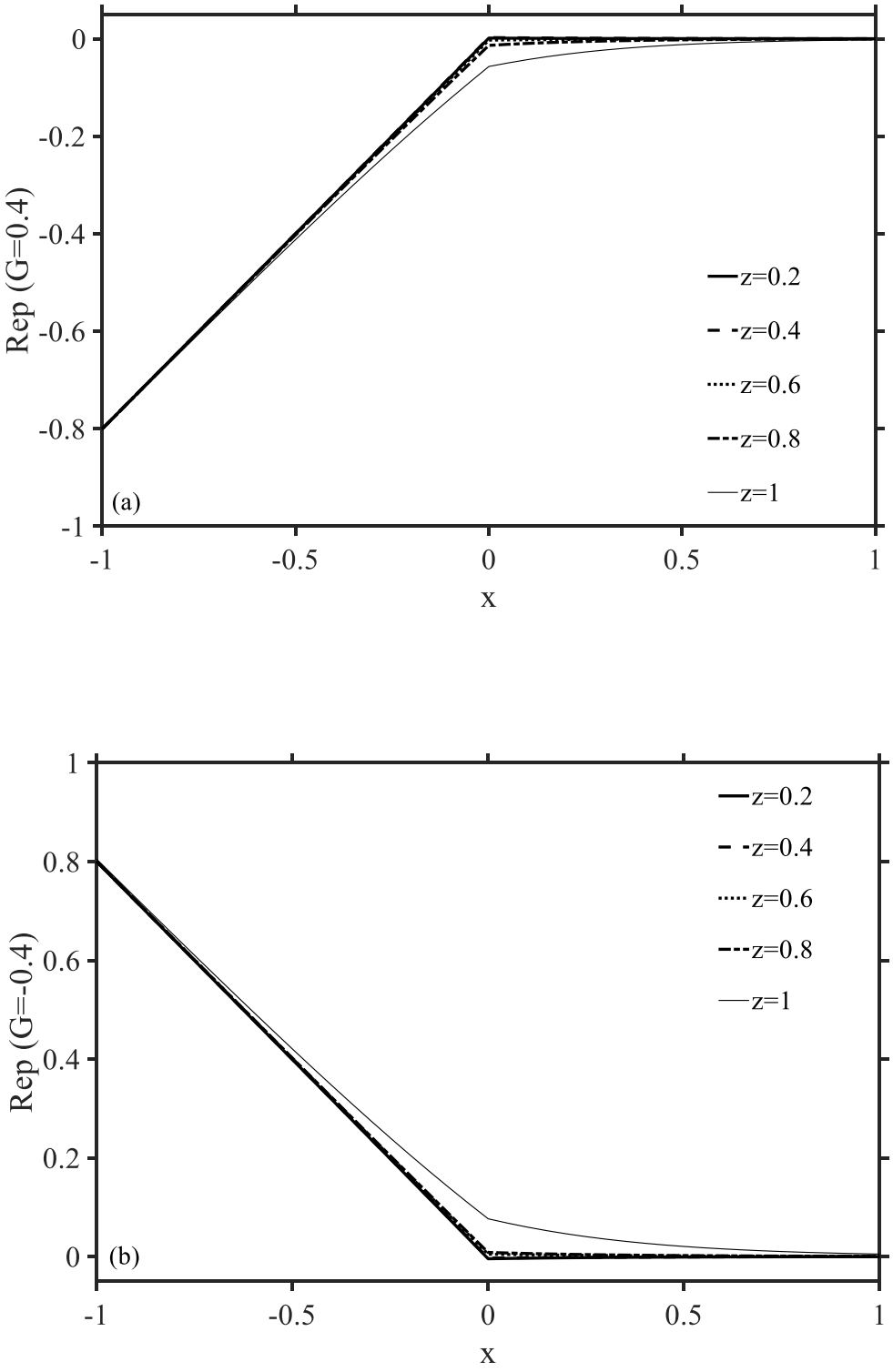

Figure 2.32: Pressure distribution at different heights for (a) G=0.4 and (b) G=-0.4.

2.6 Composite flow

The composite flow over the entire jet region is obtained by determining the composite velocity and pressure profile outside the channel. Following Van Dyke (1964), the composite expansion operator is defined by

$$C_n \equiv E_n + H_n - E_n H_n. \tag{2.6.1}$$

This expression provides a uniform approximation to order ε^n over the entire width of the jet. Given the availability of the treatment in the previous section, it is convenient to first generate $C_3\psi$, and then deduce $C_2 u$ and $C_2 w$. For n=m=3, the composite expansion for the stream function from (2.)-(2.113), namely,

$$\begin{aligned} C_3\psi = {} & \varepsilon^2 x^{2/3}\left[f_2(\theta) + \frac{G}{(1-G)} z^2 c_2 \right] \\ & + \varepsilon^3 \left\{ x f_3(\theta) + \psi_3(x,z) + \frac{2G}{1-G} + \left[(1-G)z + Gz^2 \right] h_2 \right\}. \end{aligned} \tag{2.6.2}$$

Even though the value of h_2 is required if the stream function is to be evaluated to $O(\varepsilon^3)$, this accuracy is not essential when the flow variables are determined. Differentiating the resulting stream function yields the desired composite velocity components,

$$C_2 u = u = \varepsilon x^{1/3} f_2'(\theta) + \varepsilon^2 x^{2/3}\left[f_3'(\theta) + \frac{2G}{(1-G)} z c_2 \right] + O(\varepsilon^3), \tag{2.6.3}$$

$$C_2 w = C_2 w(x,z) = -\frac{\varepsilon^2 x^{-1/3}}{3}\left[2 f_2(\theta) - \frac{f_2'(\theta + c_1)}{3} \right] + O(\varepsilon^3). \tag{2.6.4}$$

The above expressions dictate how the velocity profile changes over the entire jet width up to second order in ε. In the case of pressure, the non-zero contribution enters only to the third order, namely,

$$C_3 p = \varepsilon^3 p_3 + O(\varepsilon^4), \tag{2.6.5}$$

where p_3 is given by the expression (2.5.3.8). The effect of G on the flow field, i.e. streamwise and transverse velocities and pressure at the different x position between the free surface and upper moving wall are depicted in the figures 2.33, 2.34 and 2.35, respectively for $\varepsilon = 0.2$. The profiles of velocity u in the figure 2.33 reflect that despite the presence of significant depthwise velocity component (figure 2.34), the flow retains essentially its Couette-Poiseuille character at the channel exit. Downstream of the channel exit, there is growing slip on the free surface, which flattens the velocity profile. Eventually, the flow behavior changes from the fully developed Couette-Poiseuille to a uniform flow further downstream of the exit, i.e. at large x. The velocity profiles flatten more in the case of adverse pressure gradient (figure 2.33a) than the favorable case (figure 2.33c). However, the w profiles do not show any significant qualitative dependency on the G. It diminishes gradually with the distance x after the jump at the channel exit. Figure 2.34 confirms that the vertical flow component is essentially absent except near the free surface. Note that the flow exhibits the strong presence of both shear and elongation in the region close to the free surface. The transverse pressure gradient is particularly strong near the free surface due to sudden jump in the velocity w and shows an intricate variation across the jet. Given the vanishing of the normal force at the free surface and dominance of shear over the elongation, pressure tends to decay to zero over a relatively short distance from the channel exit (see figure 2.35). Note that for G=0 case, i.e. for pure Couette flow the pressure stays constant (figure 2.35b). In this case, to capture the pressure variation, one needs to calculate the order $O\left(\varepsilon^4\right)$ disturbances of the core flow.

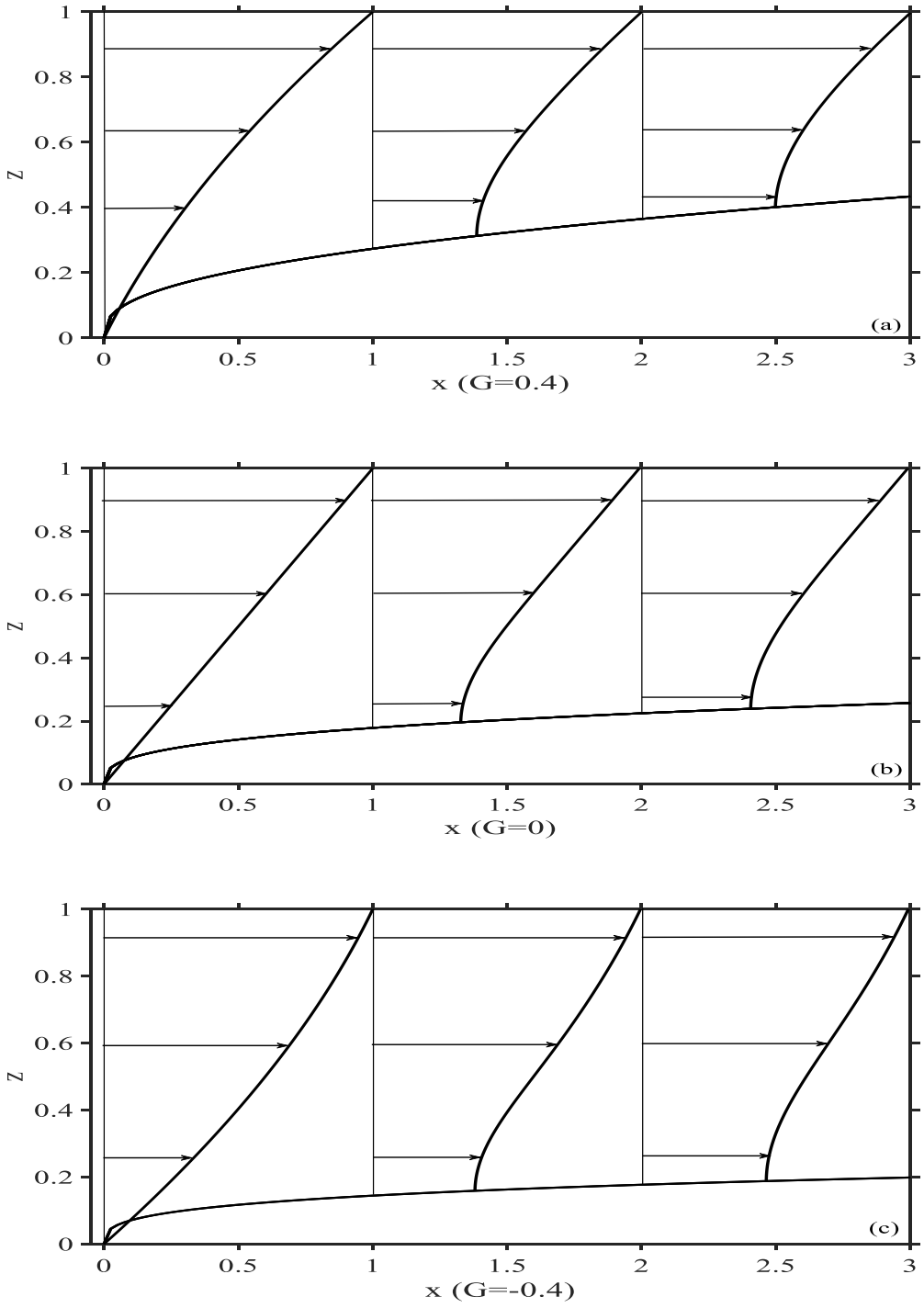

Figure 2.33: Composite Streamwise velocity profile over the entire jet region at different locations for (a) G=0.4, (b) G=0 and (c) G=-0.4 and for $\varepsilon = 0.2$. Vertical lines represent the corresponding x location.

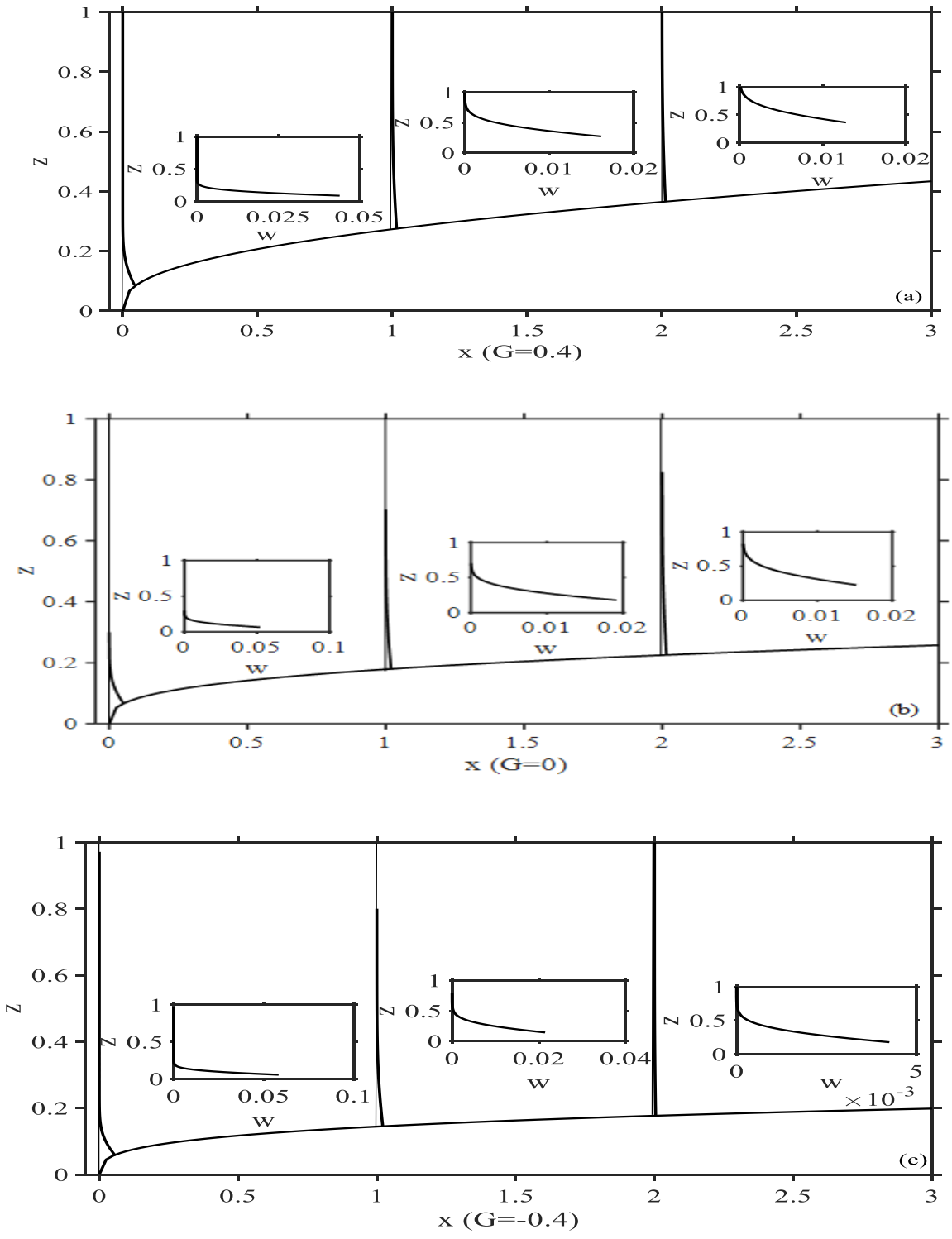

Figure 2.34: Composite transverse velocity profiles over the entire jet region at different locations for (a) G=0.4, (b) G=0 and (c) G=-0.4 and for $\varepsilon = 0.2$. Vertical lines represent the corresponding x locations and insets show the magnification of the velocity

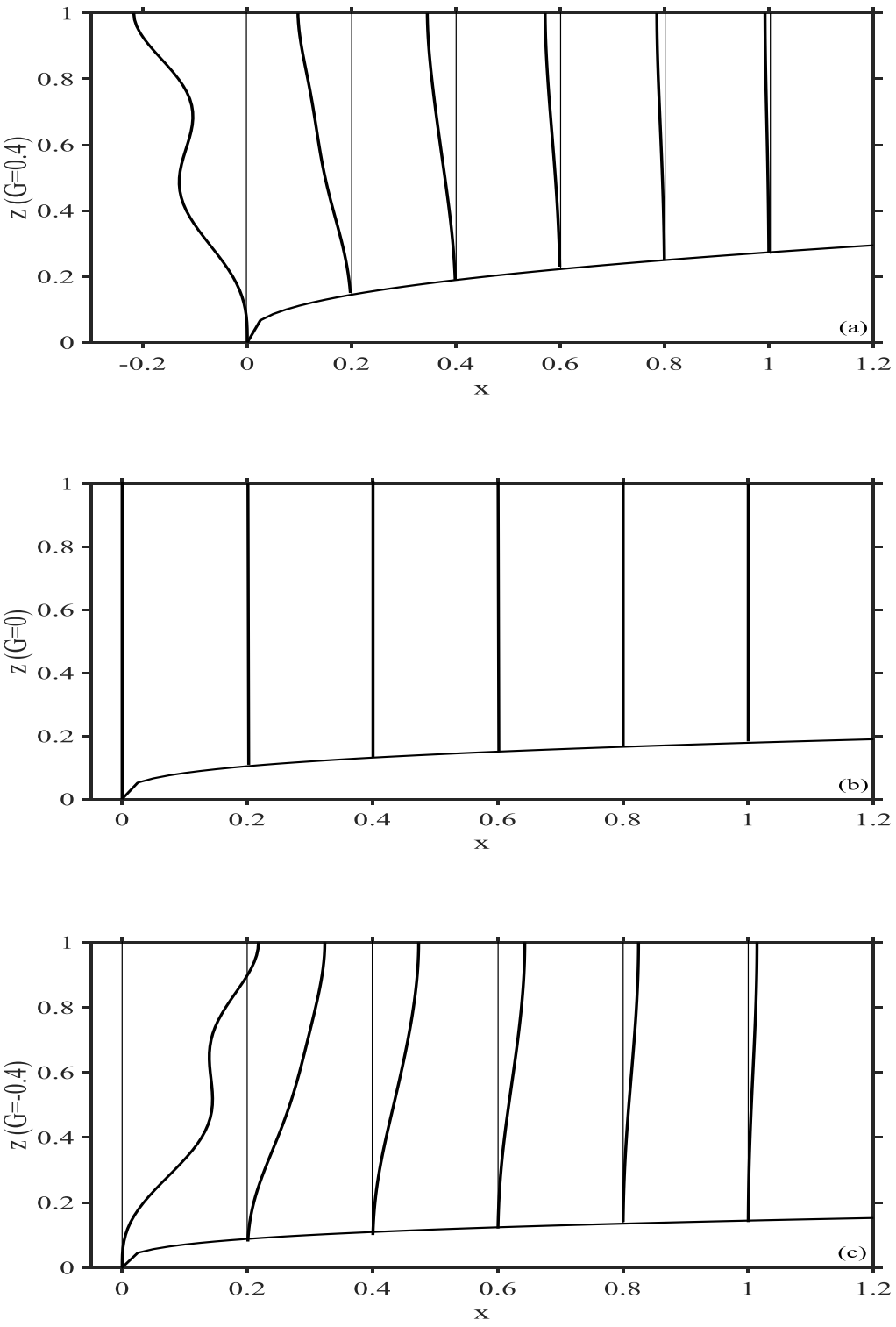

Figure 2.35: Composite pressure profiles across the jet width for (a) G=0.4, (b) G=0 and (c) G=-0.4 and for $\varepsilon = 0.2$. Vertical lines represent the corresponding x locations.

2.7 Flow far from the channel exit

In this current section, upon adopting the control volume approach the flow in the far downstream of the channel exit is examined. In this case, the non-dimensional momentum conservation equation is expressed in the integral form as,

$$\int_C (\boldsymbol{\sigma} - \mathbf{uu}) \cdot \mathbf{n} \mathrm{dl} = 0, \tag{2.7.1}$$

where, $\mathbf{u}$ is the velocity vector and $\boldsymbol{\sigma}$ is the total stress tensor, which is scaled similarly to the pressure (see section 2.1). Therefore,

$$\boldsymbol{\sigma} = -p\mathbf{I} + \varepsilon^3 \left(\nabla \mathbf{u} + \nabla \mathbf{u}^t \right). \tag{2.7.2}$$

More explicitly,

$$\sigma_{xx} = -p + 2\varepsilon^3 \psi_{xz}, \quad \sigma_{xz} = \sigma_{zx} = \varepsilon^3 \left(\psi_{zz} - \psi_{xx} \right), \ \sigma_{zz} = -p - 2\varepsilon^3 \psi_{xz}. \tag{2.7.3}$$

Here dl denotes a line element of the closed curve C. The five segments or arcs considered for the closed curve C are illustrated in figure 2.3: (i) a line $x = x_0 < 0,\ 0 \le z \le 1$ upstream, (ii) a segment $x_0 \le x \le 0,\ z = 0$ of the lower wall, (iii) a segment $0 \le x \le x_\infty,\ z = \zeta(x)$ of the lower free streamline or free surface, (iv) a line $x = x_\infty,\ \zeta(x_\infty) \le z \le 1$ downstream, and (v) the segment $x_0 \le x \le x_\infty,\ z = 1$ of the upper wall (see figure 2.3). Here x_∞ is the (dimensionless) relaxation length in the streamwise direction. Here, only the x component of equation (2.7.2) is considered. Since there is no traction on the free surface, number (iii) will not contribute in the analysis. Thus, the equation (2.7.1) reduces to,

$$\begin{aligned} &\int_0^1 \left[p - 2\varepsilon^3 \psi_{xz} + \psi_z^2 \right]_{x=x_0} dz - \int_{x_0}^0 \varepsilon^3 \psi_{zz}(x,0)\, dx \\ &- \int_{\zeta(x_\infty)}^1 \left[p - 2\varepsilon^3 \psi_{xz} + \psi_z^2 \right]_{x=x_\infty} dz + \int_{x_0}^{x_\infty} \varepsilon^3 \psi_{zz}(x,1)\, dx = 0. \end{aligned} \tag{2.7.4}$$

Obviously, the contribution to order $O\left(\varepsilon^3\right)$ will be consider only. Now, first consider the first integral. The flow is fully developed with no inner layer in the far upstream of the channel exit. In this case, based on (2.5.1.4) and (2.5.3.6), for large x_0, the first integral reads

$$\int_0^1\left[p-2\varepsilon^3\psi_{xz}+\psi_z^2\right]_{x=x_0}dz=2\varepsilon^3Gx_0+0+\frac{(1-G)^2}{3}+\frac{(1-G)G}{2}+\frac{G^2}{5}. \tag{2.7.5}$$

In addition, the second and fourth integrals are approximated up to $O\left(\varepsilon^3\right)$ and this yields

$$-\int_{x_0}^0\varepsilon^3\psi_{zz}(x,0)dx=\varepsilon^3(1-G)x_0, \tag{2.7.6}$$

$$+\int_{x_0}^{x_\infty}\varepsilon^3\psi_{zz}(x,1)dx=\varepsilon^3(1+G)(x_\infty-x_0). \tag{2.7.7}$$

Thus, upon substituting (2.7.5)-(2.7.7) into the equation (2.7.4) yields,

$$\int_\zeta^1\left[p-2\varepsilon^3\psi_{xz}+\psi_z^2\right]_{x=x_\infty}=\frac{(1-G)^2}{3}+\frac{(1-G)G}{2}+\frac{G^2}{5}+\varepsilon^3(1+G)x_\infty. \tag{2.7.8}$$

At large $x = x_\infty$, the jet reaches uniform speed W and width χ and the equation (2.7.8) reduces to,

$$W^2\chi=\frac{(1-G)^2}{3}+\frac{(1-G)G}{2}+\frac{G^2}{5}+\varepsilon^3(1+G)x_\infty. \tag{2.7.9}$$

For an incompressible fluid conservation of mass provides that,

$$W\chi=\int_0^1u_0dz==\frac{(1-G)}{2}+\frac{G}{3}. \tag{2.7.10}$$

Far downstream from the exit, if the jet velocity approaches the upper wall velocity 1, then the above equations reduce to,

$$\frac{x_\infty}{Re} = \frac{5 - G^2}{30(1+G)}, \tag{2.7.11}$$

$$\chi = \frac{3-G}{6}. \tag{2.7.12}$$

Equation (2.7.12) suggest that for a free surface moving wall jet flow the final film thickness is only a function of G, i.e. the applied pressure gradient. Moreover, in the absence of imposed pressure gradient inside the channel, i.e. for pure Couette flow a film thickness equal to the half width of the channel gap can be obtained. The thinner film thickness is possible by adding an adverse pressure gradient, i.e. for positive G cases. Increasing the magnitude of the favorable pressure gradient, i.e. negative G values will increase the film thickness. On the other hand, the length at which the jet attains a uniform width depends on both Reynolds number and G.

2.8 Matching between the inner and core layer

Matching between the inner and core layer at the interface provides the additional boundary conditions needed for solving different problems in each of the regions. Here, the matching rule developed by Van Dyke (1694) is adopted, namely,

$$E_n H_m \psi = H_m E_n \psi, \tag{2.8.1}$$

where m and n are integers. When the expansion is expressed in terms of the core variables, the core-expansion operator E_m truncates immediately after the term of order ε^n. The corresponding inner expansion operator is denoted by H_m. For successful application of the above matching rule, it is required that the stretching transformation between the inner and core variables must be expressed in the canonical form $y = \varepsilon\eta$. The core expansion in this case, must be written in terms of y, not z; otherwise, (2.8.1) can be satisfied only approximately. The two expressions in (2.8.1) must be exactly same, for all the values of

m and n. Depending on the values of m and n, different levels of matching are needed to obtain the boundary conditions for the inner and core solutions and also to determine the free surface height/displacement to each order in ε.

First, consider the matching to $O(\varepsilon)$. Recall that, to leading order, the stream function in the core region is, $\psi = (1-G)\frac{z^2}{2} + G\frac{z^3}{3}$, which is expressed in terms of y and h as

$$\psi = (1-G)\frac{(y+\varepsilon h)^2}{2} + G\frac{(y+\varepsilon h)^3}{3}. \tag{2.8.2}$$

For m=2 and n=0, applying E_0 on (2.8.2) gives

$$E_0\psi = (1-G)\frac{y^2}{2} + G\frac{y^3}{3}. \tag{2.8.3}$$

As this expression must be in inner variables when the operator H_2 is applied, it is rewritten in the following form:

$$E_0\psi = (1-G)\frac{\varepsilon^2\eta^2}{2} + G\frac{\varepsilon^3\eta^3}{3}. \tag{2.8.4}$$

Hence,

$$H_2E_0\psi = (1-G)\frac{\varepsilon^2\eta^2}{2} = (1-G)\frac{y^2}{2}. \tag{2.8.5}$$

To leading order, the inner expansion for the stream function is obtained from (2.3.1.3) as $\psi = \varepsilon^2\Psi_2$. Consequently, from (2.3.7), (2.3.1.3) and (2.3.1.6), at large θ, $H_2\psi$ is obtained in terms of outer variable as

$$H_2\psi = \varepsilon^2\Psi^2 = \varepsilon^2\xi^{2/3}f_2 = \varepsilon^2\xi^{2/3}\left\{(1-G)\frac{(\theta+c_1)^2}{2}\right\}$$
$$= \varepsilon^2\xi^{2/3}\left\{(1-G)\frac{\left(\eta\xi^{-1/3}+c_1\right)^2}{2}\right\}. \qquad (2.8.6)$$

Thus, $E_0H_2\psi = \varepsilon^2\Psi_2 = (1-G)\frac{y^2}{2}$, which when matched with (2.8.5), leads to $\Psi_2 \sim (1-G)\frac{\eta^2}{2}$ for large η. This is the condition (2.3.1.2b) or, equivalently (2.3.1.5b). Similarly, taking m=3 and n=0, leads to

$$H_3E_0\psi = (1-G)\frac{y^2}{2} + G\frac{y^3}{3}, \qquad (2.8.7)$$

$$E_0H_3\psi = E_0\left(\varepsilon^2\Psi_2 + \varepsilon^3\Psi_3\right). \qquad (2.8.8)$$

Which upon matching leads to, $\Psi_3 \sim 2\eta^3$ for large η. This is the condition (2.3.2.2b) or, equivalently (2.3.2.5b). Next, to determine h_0 and boundary condition for $\psi_1(x,z)$, consider the application of (2.8.1) for m=2 and n=1. Applying E_1 on (2.8.1),

$$E_1\psi = (1-G)\frac{y^2}{2} + G\frac{y^3}{3} + (1-G)y\varepsilon h_0 + Gy^2\varepsilon h_0 + \varepsilon\psi_1(x, y+\varepsilon h_0) \qquad (2.8.9)$$

Expanding about y,

$$\psi_1(x, y+\varepsilon h_0) = \psi_1(x,y) + \varepsilon h_0\psi_{1y}(x,y) + \frac{(\varepsilon h_0)^2}{2}\psi_{1yy}(x,y) + \cdots. \qquad (2.8.10)$$

Expanding the term on the right hand side about y=0,

$$\psi_1(x, y+\varepsilon h_0) = \psi_1(x,0) + y\psi_{1y}(x,0) + \frac{y^2}{2}\psi_{1yy}(x,0) + \cdots$$
$$+\varepsilon h_0\psi_{1y}(x,0) + \frac{(\varepsilon h_0)^2}{2}\psi_{1yy}(x,0) + \cdots. \qquad (2.8.11)$$

In this case, (2.8.9) leads to

$$E_1\psi = (1-G)\frac{y^2}{2} + G\frac{y^3}{3} + (1-G)y\varepsilon h_0 + Gy^2\varepsilon h_0 + \varepsilon\psi_1(x,0) + \varepsilon y\psi_{1y}(x,0) + \varepsilon^2 h_0\psi_{1y}(x,0) + \frac{(\varepsilon h_0)^2}{2}\psi_{1yy}(x,0). \quad (2.8.12)$$

The terms surviving to $O(\varepsilon^2)$ are identified by expressing $E_1\psi$ in terms of inner variable, $\eta = \frac{y}{\varepsilon}$ to yield,

$$H_2E_1\psi = (1-G)\frac{y^2}{2} + (1-G)y\varepsilon h_0 + \varepsilon\psi_1(x,0) + \varepsilon y\psi_{1y}(x,0) + \varepsilon^2 h_0\psi_{1y}(x,0). \quad (2.8.13)$$

On the other hand, applying E_1 in (2.8.6), leads to

$$E_1H_2\psi = (1-G)\frac{y^2}{2} + (1-G)\varepsilon y x^{1/3}c_1. \quad (2.8.14)$$

Matching (2.8.13) and (2.8.14) leads to $\psi_1(x,0) = 0$.This homogeneous boundary condition results in $\psi_1(x,y) = 0$. The remaining terms yields the result $h_0 = c_1x^{1/3}$. The vanishing of $\psi_1(x,z)$ means that, to the order ε, there is no interaction between the boundary layer and the core flow.

In this case, the free surface height is given by,

$$\zeta(x) = \varepsilon c_1(c)x^{1/3} + O(\varepsilon^2). \quad (2.8.15)$$

Applying m=2 and n=2 in (2.8.1), leads to

$$H_2E_2\psi = (1-G)\frac{y^2}{2} + (1-G)y\varepsilon h_0 + (1-G)\frac{\varepsilon^2 {h_0}^2}{2} + \varepsilon^2\psi_2(x,0), \quad (2.8.16)$$

$$E_2H_2\psi = (1-G)\frac{y^2}{2} + (1-G)\varepsilon y x^{1/3}c_1 + (1-G)\frac{\varepsilon^2 x^{2/3}c_1^2}{2}. \quad (2.8.17)$$

Again, matching (2.8.16) and (2.8.17) yields to $\psi_2(x,0)=0$, concluding that $\psi_2(x,z)=0$ everywhere which reflects the absence of interaction between the boundary layer and the core flow up to order ε^2.

Finally, to obtain h_1 and $\psi_3(x,0)$ equation (2.8.1) is applied for m=n=3. Noting that

$$\begin{aligned} H_3\psi = \varepsilon^2\Psi_2 + \varepsilon^3\Psi_3 = \varepsilon^2\xi^{2/3}&\left\{(1-G)\frac{\left(\eta\xi^{-1/3}+c_1\right)^2}{2}\right\} \\ &+\varepsilon^3\xi\left[\frac{G}{3}\left\{\left(\eta\xi^{-1/3}+c_1\right)^3-\frac{6}{1-G}\right\}+c_2\left(\eta\xi^{-1/3}+c_1\right)\right]. \end{aligned} \tag{2.8.18}$$

Thus,

$$\begin{aligned} E_3H_3\psi = (1-G)\frac{y^2}{2}+\frac{G}{3}y^3+\varepsilon x^{1/3}yc_1\left[(1-G)+Gy\right] \\ +\varepsilon^2x^{2/3}\left[\frac{(1-G)c_1^2}{2}+Gyc_1^2+c_2y\right]+\varepsilon^3x\left[c_2c_1+\frac{1}{3}\left(Gc_1^3-\frac{6G}{1-G}\right)\right]. \end{aligned} \tag{2.8.19}$$

By applying (2.8.1), it is not difficult to show that

$$\begin{aligned} E_3\psi = 2y^3-(3+c)y^2-\varepsilon\left(h_0+\varepsilon h_1+\varepsilon^2h_2\right)\left[2(3+c)-6y^2\right] \\ -\varepsilon^2\left[(3+c-6y)\left(h_0^2+2\varepsilon h_0h_1\right)\right]+\varepsilon^3\left[\psi_3(x,0)+2h_0^3\right]. \end{aligned} \tag{2.8.20}$$

Which leads to

$$\begin{aligned} H_3E_3\psi = (1-G)\frac{y^2}{2}+G\frac{y^3}{3}+\varepsilon y(1-G+Gy)h_0 \\ +\varepsilon^2\left[\left\{\frac{1-G}{2}+Gy\right\}h_0^2+(1-G)yh_1\right]+\varepsilon^3\left[(1-G)h_0h_1+\psi_3(x,0)+G\frac{h_0^3}{3}\right]. \end{aligned} \tag{2.8.21}$$

Matching (2.8.20) and (2.8.21), and recalling $h_0 = x^{1/3}c_1$, the correction of the free surface height to the next order is obtained, namely,

$$h_1 = \frac{c_2}{(1-G)} x^{2/3}. \tag{2.8.22}$$

In addition, one has,

$$\psi_3(x,0) = -\frac{2G}{1-G} x. \tag{2.8.23}$$

Condition (2.8.23) yields the third boundary condition in (2.5.5b). Consequently, for the first time, a non-trivial core problem is attained.

The height of the free surface to next order is given by,

$$\zeta(x) = \varepsilon c_1 x^{1/3} + \varepsilon^2 \frac{c_2}{(1-G)} x^{2/3}, \tag{2.8.24}$$

where c_1 and c_2 are the functions of G and are readily available from the figures 2.6 and 2.9, respectively.

Chapter 3

3 Summary and concluding remarks

The laminar two-dimensional jet flow of a Newtonian fluid exiting into the stagnant atmosphere is investigated in the current thesis. Especially, the flow near the channel exit is examined at moderate Reynolds number with the pressure gradient (adverse/favorable) applied far upstream of the channel exit. The problem is of direct relevance to two high-speed coating processes, namely, the slot coating and the blade coating. The method of matched asymptotic expansion is adopted to treat the problem. The interplay between the inertia and the pressure gradient on the free surface shape and the profiles of velocity and stress are emphasized. Sufficiently large inertia is assumed for allowing the asymptotic development of the flow in terms of the inverse Reynolds number. In this case, by expanding the flow field about the base Couette-Poiseuille flow, the equations of motion are simplified. At the channel exit, a stress singularity occurs where the boundary condition changes from no-slip at the lower wall to slip at the free surface. As a result, the entire flow domain comprises of four different regions: inner, core, lower wall, and upper wall layers. A classical boundary layer analysis is applied to determine the flow behavior in the free surface or inner layer as well as in the lower wall layer. Note that the upper wall layer is not treated in the present study. The boundary or inner layer forms near the free surface due to the presence of the stress singularity at the channel exit whereas the failure of satisfying the wall adherence of the core flow causes the two wall layers to form.

The boundary layer structure near the free surface and lower wall are investigated in details. Two similarity solutions are obtained in the two regions, which allow to avoid dealing with the singularity explicitly at the singular point, i.e. at x=0. In this case, matching between the inner layer and lower wall layer is not required due to the similarity nature of the solutions. This constitutes a major advantage of the current formulation over the numerical counterpart where the whole domain discretization is an essential requirement. The shape of the free surface is acquired by matching inner layer flow with the core flow outside the cannel exit. It is found that the free surface always contracts near the channel exit regardless of the level of inertia and direction of the applied pressure gradient. Depending on the direction of the pressure gradient, upon approaching the channel exit, the fluid exhibits an

increase (favorable case) or decrease (adverse case) in shearing at the lower wall with the inertia. In the case of pressure along the lower wall, it remains close to the Couette-Poiseuille level inside the channel and takes a negative or positive dip at the channel exit. These behaviors are reminiscent of the results found by Mitsoulis (2010), and Iilipoulos and Scriven (2005) for the blade coating flow numerically. While the film thickness gets thinner with the increasing level of adverse pressure gradient, it becomes thicker with the increase of the favorable pressure gradient. However, the film thickness increases with the inertia and reaches to an asymptotic value at higher inertia, i.e. larger Reynolds number. This trend also aggresses qualitatively with the previous studies conducted on the slot and the blade coating flows (refer to figure 10 of Ilipoulos and Scriven 2005, figure 11 of Lin et al. 2010, and figure 5 of Chin et al. 2010).

The present analysis provides an accurate estimate of the flow behaviors close to the channel exit, which are necessary to determine the flow far downstream of the channel exit. When the jet achieves a thin uniform profile further downstream, any thin layer approximation such as boundary layer or lubrication theory can be used to obtain the flow characteristics with currently predicted flow conditions. Note that similar to the thin film analysis, current formulation is not valid very close to the exit, i.e. at the point of inception. The analytical form of the steady-state flow obtained from the current analysis can be utilized to carry out a linear stability analysis.

3.1 Future work

Although the current thesis focuses only on the steady state flow of a free surface moving wall jet encountered in the slot and the blade coating processes, the followings can be done as an expansion work:

a) Calculation of the flow behavior in the boundary layer along the upper (moving) wall.
b) Incorporation of the non-Newtonian effects using polymeric solution instead of Newtonian fluid.
c) Consideration of the surface tension and gravity effects in the formulation, which have been neglected in the present study.

d) The heat transfer effect is not studied in the current thesis, which can be incorporated in the future.
e) Currently, only single layer of flow is considered. This can be extended by taking two layers of flow into consideration.

References

Aidun, C. K., & Triantafillopoulos, N. G. 1997. High-speed blade coating. *Liquid film coating*, 637-672. Springer, Dordrecht.

Amin, R. 2011 Moving wall jet flow near channel exit at moderate Reynolds number. Master's thesis, Department of Mechanical and Materials Engineering, The University of Western Ontario, London, Ontario, Canada.

Araujo, S. B., & Carvalho, M. S. 2014 Slot coating of particle suspension, *17th International Coating Science and Technology Symposium*, September 7-10, 2012, San Diego, California.

Ashmore, J., Shen, A. Q., Kavehpour, H. P., Stone, H. A., & McKinley, G. H. 2007 Coating flows of non-Newtonian fluids: weakly and strongly elastic limits. *Journal of Engineering Mathematics*, 60(1), 17-41.

Azad, Md. A. K. 2011. Pressure driven wall jet flow near channel exit at moderate Reynolds number. Master's thesis, Department of Mechanical and Materials Engineering, The University of Western Ontario, London, Ontario, Canada.

Bajaj, M., Prakash, J. R., & Pasquali, M. 2008 A computational study of the effect of viscoelasticity on slot coating flow of dilute polymer solutions. *Journal of Non-Newtonian Fluid Mechanics*, 149(1), 104-123.

Benilov, E. S., Benilov, M. S., & Kopteva, N. 2008 Steady rimming flows with surface tension. *Journal of Fluid Mechanics*, 597, 91-118.

Bowles, R. I., & Smith, F. T. 1992 The standing hydraulic jump: theory, computations and comparisons with experiments. *Journal of Fluid Mechanics*, 242, 145-168.

Bush, J. W., & Aristoff, J. M. 2003 The influence of surface tension on the circular hydraulic jump. *Journal of Fluid Mechanics*, 489, 229-238.

Cameron, A. 1966 *The principles of Lubrication*. Longmans Green & Co. London WI.

Carvalho, M. S., & Kheshgi, H. S. 2000 Low-flow limit in slot coating: Theory and experiments. *AIChE journal*, 46(10), 1907-1917.

Chang, Y. R., Chang, H. M., Lin, C. F., Liu, T. J., & Wu, P. Y. 2007 Three minimum wet thickness regions of slot die coating. *Journal of Colloid and Interface Science*, 308(1), 222-230.

Chang, Y. R., Lin, C. F., & Liu, T. J. 2009 Start-up of slot die coating. *Polymer Engineering & Science*, 49(6), 1158-1167.

Chin, C. P., Wu, H. S., & Wang, S. S. 2010 Improved coating window for slot coating. *Industrial & Engineering Chemistry Research*, 49(8), 3802-3809.

Chu, W. B., Yang, J. W., Wang, Y. C., Liu, T. J., Tiu, C., & Guo, J. 2006 The effect of inorganic particles on slot die coating of poly (vinyl alcohol) solutions. *Journal of Colloid and Interface Science*, 297(1), 215-225.

Eggers, J., & Villermaux, E. 2008 Physics of liquid jets. *Reports on Progress in Physics*, 71(3), 036601.

Elliotis, M., Georgiou, G., & Xenophontos, C. 2005 Solution of the planar Newtonian stick–slip problem with the singular function boundary integral method. *International Journal for Numerical Methods in Fluids*, 48(9), 1001-1021.

Glauert, M. B. 1956 The wall jet. *Journal of Fluid Mechanics*, 1(6), 625-643.

Goren, S. L., & Wronski, S. 1966 The shape of low-speed capillary jets of Newtonian liquids. *Journal of Fluid Mechanics*, 25(1), 185-198.

Higgins, B. G., & Scriven, L. E. 1980 Capillary pressure and viscous pressure drop set bounds on coating bead operability. *Chemical Engineering Science*, 35(3), 673-682.

Higgins, B. G. 1982 Downstream development of two-dimensional viscocapillary film flow. *Industrial & Engineering Chemistry Fundamentals*, 21(2), 168-173.

Hong, S., Lee, J., Kang, H., & Lee, K. 2013 Slot-die coating parameters of the low-viscosity bulk-heterojunction materials used for polymer solar cells. *Solar Energy Materials and Solar Cells*, 112, 27-35.

Hussain, Md. Y. 2010 Flow of a Jet depositing on a moving wall near channel exit at moderate Reynolds number. Master's thesis, Department of Mechanical and Materials Engineering, The University of Western Ontario, London, Ontario, Canada.

Jang, I., & Song, S. 2013 A model for prediction of minimum coating thickness in high speed slot coating. *International Journal of Heat and Fluid Flow*, 40, 180-185.

Khayat, R. E. 2014 Free-surface jet flow of a shear-thinning power-law fluid near the channel exit. *Journal of Fluid Mechanics*, 748, 580-617.

Khayat, R. E. 2016a Slipping free jet flow near channel exit at moderate Reynolds number for large slip length. *Journal of Fluid Mechanics*, 793, 667-708.

Khayat, R. E. 2016b Impinging planar jet flow on a horizontal surface with slip. *Journal of Fluid Mechanics*, 808, 258-289.

Khayat, R. E. 2017 Initial development of a free-surface wall jet at moderate Reynolds number. *Journal of Fluid Mechanics*, 826, 235-269.

Levin, O., Chernoray, V. G., Löfdahl, L., & Henningson, D. S. 2005 A study of the Blasius wall jet. *Journal of Fluid Mechanics*, 539, 313-347.

Lin, C. F., Hill Wong, D. S., Liu, T. J., & Wu, P. Y. 2010 Operating windows of slot die coating: comparison of theoretical predictions with experimental observations. *Advances in Polymer Technology*, 29(1), 31-44.

Lee, K. Y., Liu, L. D., & Ta-Jo, L. 1992 Minimum wet thickness in extrusion slot coating. *Chemical Engineering Science*, 47(7), 1703-1713.

Lee, A. G., Shaqfeh, E. S., & Khomami, B. 2002 A study of viscoelastic free surface flows by the finite element method: Hele–Shaw and slot coating flows. *Journal of Non-Newtonian Fluid Mechanics*, 108(1), 327-362.

Iliopoulos, L., & Scriven, L. E. 2005 A blade-coating study using a finite-element simulation. *Physics of Fluids*, 17(12), 127101.

Mahmood, T. 1988 A laminar wall jet on a moving wall. *Acta Mechanica*, 71(1), 51-60.

Maillard, M., Mézière, C., Moucheront, P., Courrier, C., & Coussot, P. 2016 Blade-coating of yield stress fluids. *Journal of Non-Newtonian Fluid Mechanics*, 237, 16-25.

Maki, H. 1983 Experimental studies on the combined flow field formed by a moving wall and a wall jet running parallel to it. *Bulletin of JSME*, 26(222), 2100-2105.

Middleman, S. 1995 *Modeling axisymmetric flows: dynamics of films, jets, and drops*. Academic Press, 63-65.

Mitsoulis, E. V. A. N. 2010 Numerical simulation of viscoelastic effects in blade-over-roll coating forming flows. *Computer Methods in Materials Science*, 10(3), 156-166.

Mitsoulis, E. V. A. N. & Athanasopoulos, G. 2010 Numerical simulation of Blade-over-roll coating forming flows. *Computer Methods in Materials Science*, 10(4), 214-224.

Miyake, Y., Mukai, E., & Iemoto, Y. 1979 On a two-dimensional laminar liquid jet. *Bulletin of JSME*, 22(172), 1382-1389.

Merkin, J. H., & Needham, D. J. 1986 A note on the wall-jet problem. *Journal of Engineering Mathematics*, 20(1), 21-26.

Pantokratoras, A. 2011 The nonsimilar laminar wall jet along a moving wall, in a free stream and in a free stream/moving wall. *Applied Mathematical Modelling*, 35(1), 471-481.

Philippe, C., & Dumargue, P. 1991 Étude de l'établissement d'un jet liquide laminaire émergeant d'une conduite cylindrique verticale semi-infinie et soumis à l'influence de la gravité. *Zeitschrift für angewandte Mathematik und Physik ZAMP*, 42(2), 227-242.

Pranckh, F. R., & Scriven, L. E. 1990 Elastohydrodynamics of blade coating. *AIChE Journal*, 36(4), 587-597.

Riley, N. 1958 Effects of compressibility on a laminar wall jet. *Journal of Fluid Mechanics*, 4(6), 615-628.

Ro, J. S., & Homsy, G. M. 1995 Viscoelastic free surface flows: thin film hydrodynamics of Hele-Shaw and dip coating flows. *Journal of Non-Newtonian Fluid Mechanics*, 57(2-3), 203-225.

Romero, O. J., Suszynski, W. J., Scriven, L. E., & Carvalho, M. S. 2004 Low-flow limit in slot coating of dilute solutions of high molecular weight polymer. *Journal of Non-Newtonian Fluid Mechanics*, 118(2), 137-156.

Romero, O. J., Scriven, L. E., & Carvalho, M. S. 2006 Slot coating of mildly viscoelastic liquids. *Journal of Non-Newtonian Fluid Mechanics*, 138(2), 63-75.

Ruschak, K. J. 1976 Limiting flow in a pre-metered coating device. *Chemical Engineering Science*, 31(11), 1057-1060.

Ruschak, K. J., & Scriven, L. E. 1977 Developing flow on a vertical wall. *Journal of Fluid Mechanics*, 81(2), 305-316.

Ruschak, K. J. 1985 Coating flows. *Annual Review of Fluid Mechanics*, 17(1), 65-89.

Saffari, A., & Khayat, R. E. 2009 Flow of viscoelastic jet with moderate inertia near channel exit. *Journal of Fluid Mechanics*, 639, 65-100.

Saito, H., & Scriven, L. E. 1981 Study of coating flow by the finite element method. *Journal of Computational Physics*, 42(1), 53-76.

Saito, F. A., and L. E. Scriven 1985 Coating Flow Analysis and the Physics of Flexible Blade Coating. *Coating Conf Proc*., TAPPI Press, Atlanta, USA.

Schlichting, H., Gersten, K., Krause, E., & Oertel, H. 2000 *Boundary-layer theory*. New York: McGraw-hill.

Shi, J. M., Breuer, M., & Durst, F. 2004 A combined analytical–numerical method for treating corner singularities in viscous flow predictions. *International Journal for Numerical Methods in Fluids*, 45(6), 659-688.

Smith, F. T. 1976 Flow through constricted or dilated pipes and channels: Part 1. *The Quarterly Journal of Mechanics and Applied Mathematics*, 29(3), 343-364.

Smith, F. T. 1976 Flow through constricted or dilated pipes and channels: Part 2. *The Quarterly Journal of Mechanics and Applied Mathematics*, 29(3), 365-376.

Smith, F. T. 1977 Upstream interactions in channel flows. *Journal of Fluid Mechanics*, 79(4), 631-655.

Smith, F. T. 1979 The separating flow through a severely constricted symmetric tube. *Journal of Fluid Mechanics*, 90(4), 725-754.

Sobey, I. J. 2005 *Introduction to Interactive Boundary Layer Theory*. Oxford University Press.

Sullivan, T. M., & Middleman, S. 1986 Film thickness in blade coating of viscous and viscoelastic liquids. *Journal of Non-Newtonian Fluid Mechanics*, 21(1), 13-38.

Sullivan, T., Middleman, S., & Keunings, R. 1987 Use of a finite-element method to interpret rheological effects in blade coating. *AIChE Journal*, 33(12), 2047-2056.

Tillett, J. P. K. 1968 On the laminar flow in a free jet of liquid at high Reynolds numbers. *Journal of Fluid Mechanics*, 32(2), 273-292.

Tsukiji, T., & Takahashi, K. 1987 Numerical analysis of an axisymmetric jet using a streamline coordinate system. *JSME International Journal*, 30(267), 1406-1413.

Van Dyke, M. D. 1964 *Perturbation Methods in Fluid Mechanics*. Academic Press, New York.

Watson, E. J. 1964 The radial spread of a liquid jet over a horizontal plane. *Journal of Fluid Mechanics*, 20(3), 481-499.

Weinstein, S. J., & Ruschak, K. J. 2004. Coating flows. *Annual Review of Fluid Mechanics*, 36, 29-53.

Wilson, D. E. 1986. A similarity solution for the axisymmetric viscous-gravity jet. *Physics of Fluids*, 29(3), 632-639.

Yu, W. J., Liu, T. J., & Yu, T. A. 1995 Reduction of the minimum wet thickness in extrusion slot coating. *Chemical Engineering Science*, 50(6), 917-920.

Yusuf, O. B. 2012 Improved non-linear solution of dip coating flow. Master's thesis, Department of Mechanical and Materials Engineering, The University of Western Ontario, London, Ontario, Canada.

Zhao, J., & Khayat, R. E. 2008 Spread of a non-Newtonian liquid jet over a horizontal plate. *Journal of Fluid Mechanics*, 613, 411-443.

Curriculum Vitae

Name:	Mohammad Tanvir Hossain
Post-secondary Education and Degrees:	The University of Western Ontario London, Ontario, Canada 2016-2017 (Ongoing) M.E.Sc. (MME) Khulna University of Engineering & Technology (KUET) Khulna, Bangladesh 2008-2012 B.Sc. (Mechanical Engineering)
Related Work Experience	Research and Teaching Assistant The University of Western Ontario, London, Ontario, Canada. 2016-2017